

Investigation of Non-coherent Discrete Target Range Estimation Techniques for High-precision Location

Qiushi Wu

A thesis submitted for the degree of

Doctor of Philosophy

of

University College London

Sensors, Systems and Circuits Group

Department of Electronic and Electrical Engineering

University College London

May 2020

I, Qiushi Wu, confirm that the work presented in this thesis is my own. Where information has been derived from other sources, I confirm that this has been indicated in the thesis.

Signature _____

Date _____

Abstract

Ranging is an essential and crucial task for radar systems. How to solve the range-detection problem effectively and precisely is massively important. Meanwhile, unambiguity and high resolution are the points of interest as well.

Coherent and non-coherent techniques can be applied to achieve range estimation, and both of them have advantages and disadvantages. Coherent estimates offer higher precision but are more vulnerable to noise and clutter and phase wrap errors, particularly in a complex or harsh environment, while the non-coherent approaches are simpler but provide lower precision. With the purpose of mitigating inaccuracy and perturbation in range estimation, miscellaneous techniques are employed to achieve optimally precise detection. Numerous elegant processing solutions stemming from non-coherent estimate are now introduced into the coherent realm, and vice versa.

This thesis describes two non-coherent ranging estimate techniques with novel algorithms to mitigate the instinct deficit of non-coherent ranging approaches. One technique is based on peak detection and realised by K^{th} -order Polynomial Interpolation, while another is based on Z-transform and realised by Most-likelihood Chirp Z-transform. A two-stage approach for the fine ranging estimate is applied to the Discrete Fourier transform domain of both algorithms. An N -point Discrete Fourier transform is implemented to attain a coarse estimation; an accurate process around the point of interest determined in the first stage is conducted. For KPI technique, it interpolates around the peak of Discrete Fourier transform profiles of the chirp signal to achieve accurate interpolation and optimum precision. For Most-likelihood Chirp Z-transform technique, the Chirp Z-transform accurately implements the periodogram where only a narrow band spectrum is processed. Furthermore, the concept of most-likelihood estimator is introduced to combine with Chirp Z-transform to acquire better ranging performance. Cramer-Rao lower bound is presented to evaluate the performance of these two techniques from the perspective of statistical signal processing.

Mathematical derivation, simulation modelling, theoretical analysis and experimental validation are conducted to assess technique performance. Further research will be pushed forward to algorithm optimisation and system development of a location system using non-coherent techniques and make a comparison to a coherent approach.

Impact Statement

The capability of estimating the range of targets effectively and precisely is of significant importance to a radar system, as well as its post-processing chain. Majority of applications call on high-performance range estimation with computational feasibility and efficiency. This thesis presents two non-coherent ranging estimate techniques with novel algorithms to enhance their precision of detection, while these two approaches are computationally practical and useful. Such techniques can be implemented to long-term surveillance and precise detection of ice shelves in Antarctica for the research of global climate change, automotive radar systems with features of small size and high performance for smart transportation, radar-communication integration with the development of the 5th Generation communication networks, collaborative situational awareness, wearable sensing equipment, and Internet of the things.

Acknowledgement

I would like to express my sincere gratitude to my supervisor, Professor Paul V. Brennan, for his wholehearted patience and encouragement. His concise but insightful words kept sparking genuine aspiration and academic inspiration on me, which led my research to move forward steadily. He created spacious space for me to explore my interests in research and gave me time to heal myself when progress was not satisfactory.

I am eternally grateful to radar group colleagues, who are all kindly and helpful, especially Lai Bun, Mandana, Alvaro, and Chen, for taking their time out busy schedules to figure out problems and give valuable advice to me and providing neat solutions to my practical struggles in researches, and Matt and Amin as well, for organising weekly seminars to present creative perspectives and collect remarkable feedbacks. Meanwhile, I wish to recognise the invaluable assistance from IT support and department staff all provided.

I am deeply indebted to my alma mater, the National University of Defense Technology in Changsha, China, granting me this opportunity to study abroad, as well as Wei Wang and Shunping Xiao, who led me into the research career as my mentors and supervisors.

Words cannot express how grateful I am to Ziyi Kang and Yueying Cao. It has been over 15 years since we first met. We shared brilliant ideas and engaging experiences in our work or life, watched NFL and NBA online, played Overwatch and Hearthstone together, and even explored the recipe for a durian pizza. Regardless of the time difference, our lifelong friendship of mutual understanding and heartfelt closeness has accompanied me to surviving from the darkest hour during my research journey so far.

A wholehearted appreciation goes to Hao Xu, who lived under the same roof with me for three years. Your perseverance and diligence inspired me a lot; you are a genuine role model for me, both as a researcher in the scholarly realm and as a man in daily life. Our friendship and brotherhood built through the time supported us to the happy ending of our PhD journey.

Besides, I wish to show my gratitude to Bote Luo, Yang Yi, Dandan Wang, Xianghao Xie, Ruofei Wen, Xinyi Zhou, Zhiyi Ren, and Wentao Chen. We have been knowing each other since senior high. I have been treasuring those iridescent experiences and memories we shared. The fascinating discovery real friends make is that we can grow separately, without growing apart.

I would also like to appreciate Yifang Yang, who was one of my close friends in London. Nor was I bored with our conversation with sparkling thoughts and joy every time. I hope her dream of being an executive producer comes true in the United States.

Furthermore, thanks should go to certain of my eldership. Liping Yu, Juan Liang, Jingzi Deng, and Yuanyuan Liu were my English teachers from junior high to postgraduate, respectively. Taigang He and Peiyuan Pan presented considerate help and valuable advice after I came to London. Yihua Hou, Yang Wang, Honglun Guo and Shijian Pi helped me a lot on various tricky paperwork. Ke Sheng and Hanhua Hu treated me as their child; I hope their daughter, Zhuang Sheng, grow up healthy and cheerful.

I also had the great pleasure of living with Qing, Xiangyuan, Fan, Akshay, and Juan at Liberty Living in Sebastian street, where you brought much happiness at the shared but narrow kitchen.

I cannot leave London without mentioning Sihao Lu, Hui Chen and Xiaoyuan Ren. "Uncle" Hao gave me infinite mental comfort and aspiration through his essays; Chen shared the same passion for writing with me, and she sent Lu's books with the autograph to London every year; Ren is one of my lifelong friends since undergraduate, and I wish his wedding as well as PhD viva will go smoothly.

I extend my gratitude to my friends wherever in China or Britain, excluding those mentioned above, namely Yang Zhang, Shu Tan, Cindy Feng, Fengyu Li, Jing Tao, Xinyuan Zhang, Weining Sun, Danping Wu, Xinru Chen, Teng Dong, Wei Liu, Shicheng Zhang, Xiao Li, Ti Wu, Xiaoxiao Zhao, and Zimo Liu. It was you all who gave me the solid strength to keep calm and carry on.

Special regards also to Zehan Zhang, Shiyu Tang, Zhen Hou, Qiyuan Sun, Meng Liu, Jin Zhao, Second, Shuiwang, Nainai, Bear, Jack, Yuanweiji, Dadajie, Kevin, Luna, and Biscuit. We held colourful memories and thrilling moments in the World of Warcraft. Hero shall light be with you and hover your wings.

Most significantly, most profound appreciation goes to my parents, grandparents, and uncles and aunts. You raised me, believed in and supported for me unconditionally; I could not have exploited this far without you. When I am chasing rainbows all the way, home always backs me up regardless of smiles or tears.

It is not an end, just a midway camp of another unknown and fascinating expedition. The comprehension regarding life and self-cognition that I have learnt during my PhD will be a lifetime treasure, which inspire and motivate myself never stopping exploration, never giving up, and never being afraid to hit the limits. As Winston Churchill once said, "Success is not final, failure is not fatal: it is the courage to continue that counts".

Contents

Abstract	3
Impact Statement	4
Acknowledgement	5
Contents	7
List of Figures	10
List of Tables	13
Abbreviations	14
1. Introduction	16
1.1 Overview	16
1.2 Aims and Target Applications	17
1.3 Novel Contributions and Publications	19
1.4 Thesis Organisation.....	19
2. Background Theory	22
2.1 Radar theory	22
2.1.1 Essential Radar Functions and Elements.....	22
2.1.2 Doppler Radar	25
2.2 Frequency-modulated Continuous Wave Radar	30
2.2.1 System Summary.....	31
2.2.2 Advantages.....	32
2.3 Fundamentals of Range Estimation	34
2.3.1 Radar Range Equations	34
2.3.2 Range Resolution and Maximum Unambiguous Range.....	37
2.4 Previews of Basic Radar Signal Processing	39
2.4.1 Radar Time Scales and Phenomenology	40
2.4.2 Signal Conditioning and Interference Suppression.....	41
2.4.3 Detecting, Imaging, and Postprocessing	43
2.5 Estimation Theory of Statistical Signal Processing	45
2.5.1 Probability Density Function	46
2.5.2 Minimum Variance Unbiased Estimation	48
2.5.3 Cramer-Rao Lower Bound.....	50
3. Current Ranging Techniques for High-precision Performance	54
3.1 Coherent Ranging Techniques.....	55
3.1.1 I/Q Detection	56

3.1.2	ApRES System and Phase-sensitive Processing.....	59
3.2	Non-coherent Ranging Techniques	62
3.2.1	Non-coherent MTI system	63
3.2.2	Detection Performance.....	64
3.3	Mathematical Descriptions of Several Useful Transform Tools	70
3.3.1	Fourier Transform	70
3.3.2	Z Transform	73
3.3.3	Laplace Transforms	75
4.	Non-coherent Range Estimation by Peak Detection and Chirp Z Transform Method.....	78
4.1	Method Description of Peak Detection	78
4.2	Algorithm Realisation by Polynomial Interpolation.....	79
4.2.1	Quadratic Interpolation	80
4.2.2	Cubic Interpolation.....	81
4.2.3	Quartic Interpolation	83
4.2.4	A general equation for <i>Kth</i> -order polynomial Interpolation	84
4.3	Method Description of Chirp-Z transform.....	85
4.4	Algorithm Realisation by Most-likelihood Chirp Z Transform	87
4.5	Mathematical Derivation of Most-likelihood Process in Chirp Z Transform	89
5.	Mathematical derivation of Cramer-Rao Lower Bound of Two Ranging Algorithms	95
5.1	Transformation of Parameters and CRLB of Vector Parameters.....	95
5.2	CRLB of <i>Kth</i> -order Polynomial Interpolation Algorithm.....	98
5.3	CRLB of Most-likelihood Chirp Z Transform Algorithm.....	105
6.	Simulation Results and Analysis.....	111
6.1	Results of Peak Detection by <i>Kth</i> -order Polynomial Interpolation	111
6.1.1	Pre-processing of Zero-padding	111
6.1.2	Results of Quadratic Interpolation.....	112
6.1.3	Results of Cubic Interpolation.....	115
6.1.4	Results of Quartic Interpolation.....	116
6.2	Results of Most-likelihood Chirp Z Transform	117
7.	Experimental Results and Discussion.....	120
7.1	FFT Process with Window Functions	121
7.2	Further Results of Polynomial Interpolation	124
7.3	Comparison between Coherent and Non-Coherent Ranging Approaches.....	129
8.	Conclusions and Future Work.....	136
8.1	Conclusions	136
8.2	Future Work.....	139

8.2.1	System Development	139
8.2.2	High-precision Ranging on radar communication integration.....	140
	Appendixes.....	142
	References	162

List of Figures

- 2.1 [Spherical coordinate system for radar measurement](#)
- 2.2 [An illustration of a pulsed monostatic radar](#)
- 2.3 [Types of Doppler radars](#)
- 2.4 [A simplified illustration of CW radar](#)
- 2.5 [A simplified illustration of a pulse-Doppler radar](#)
- 2.6 [A simplified illustration of FMCW radar](#)
- 2.7 [A typical flowchart of radar signal processing](#)
- 2.8 [Real part of an LFM signal](#)
- 2.9 [Imaginary part of an LFM signal](#)
- 2.10 [Spectrum of an LFM signal](#)
- 2.11 [Spectrum of an LFM signal \(close look\)](#)
- 2.12 [Probability density function \(PDF\) of Gaussian and Rayleigh models](#)
- 3.1 [A brief diagram of a coherent pulse radar](#)
- 3.2 [A brief diagram of a conventional model of \$I/Q\$ detection network](#)
- 3.3 [Rectangular and polar coordinate system representations of \$I/Q\$ vector](#)
- 3.4 [Locus plot of ideal target vector and the effects of \$I/Q\$ errors](#)
- 3.5 [Block diagram of basic ApRES system instruction](#)
- 3.6 [Outline of an FMCW ranging technique with phase-sensitive processing](#)
- 3.7 [Brief illustration of a pulsed non-coherent radar system](#)
- 3.8 [Nonfluctuating Coherent ROC Curves for different SNR values](#)
- 3.9 [Nonfluctuating Coherent ROC Curves \(averaging over two pulses\)](#)
- 3.10 [Nonfluctuating Noncoherent ROC Curves for different SNR values](#)
- 3.11 [Nonfluctuating Noncoherent ROC Curves](#)
- 3.12 [Nonfluctuating Noncoherent ROC Curves \(with 20 integrated pulses\)](#)

- 3.13 [ROC Curve of Swerling 1 Target Model](#)
- 4.1 [Quadratic interpolation around the DFT peak](#)
- 4.2 [Pascal's triangle and binomial coefficients](#)
- 6.1 [Deramped signal and zero-padding](#)
- 6.2 [Quadratic interpolation with padding factor \$p=2\$](#)
- 6.3 [Quadratic interpolation with padding factor \$p=1\$](#)
- 6.4 [Quadratic interpolation with padding factor \$p=4\$](#)
- 6.5 [Cubic interpolation with padding factor \$p=2\$](#)
- 6.6 [Cubic interpolation with padding factor \$p=4\$](#)
- 6.7 [Quartic interpolation with padding factor \$p=1\$](#)
- 6.8 [Quartic interpolation with padding factor \$p=4\$](#)
- 6.9 [A spiral contour of MLCZT](#)
- 6.10 [CTZ and FFT](#)
- 6.11 [MLCZT error in range bins](#)
- 7.1 [Features of three kinds of window functions](#)
- 7.2 [Normalised amplitude spectrum of Rectangular window](#)
- 7.3 [Normalised Amplitude Spectrum of Hamming Window](#)
- 7.4 [Normalised Amplitude Spectrum of Hanning Window](#)
- 7.5 [Normalised Amplitude Spectrum of Kaiser Window](#)
- 7.6 [Deramped Signal with zero-padding and window](#)
- 7.7 [Estimation Performance of Quadratic Interpolation with/without window function](#)
- 7.8 [Estimation Performance of Quartic Interpolation with/without window function](#)
- 7.9 [Experimental System and Layout of an FMCW radar prototype](#)
- 7.10 [Deramped Signals of Loop Test](#)
- 7.11 [Frequency Spectrum and Range Profile of Loop Test](#)
- 7.12 [Frequency Spectrum and Range Profile with LO power 10.5 dBm](#)

7.13 [Frequency Spectrum and Range Profile with LO power 15.5 dBm](#)

7.14 [Frequency Spectrum and Range Profile with LO power 17.5 dBm](#)

List of Tables

- 2.1 [Distinctive modes of pulsed Doppler radars](#)
- 3.1 [Principal Radar Parameters of ApRES System](#)
- 6.1 [Simulation Parameters of Polynomial Interpolation](#)
- 7.1 [Properties of a variety of common data windows](#)
- 7.2 [Polynomial interpolation Error under several conditions](#)
- 7.3 [Principal Radar Parameters](#)
- 7.4 [Processing Results of Loop Test](#)
- 7.5 [Processing Results with LO power 10.5 dBm](#)
- 7.6 [Processing Results with LO power 15.5 dBm](#)
- 7.7 [Processing Results with LO power 17.5 dBm](#)

Abbreviations

AC	Alternating Current
ACF	Autocorrelation Function
ADC	Analogue to Digital Converter
AM	Amplitude Modulated
BPF	Bandpass Filter
CPI	Coherent Processing Interval
CRLB	Cramer-Rao Lower Bound
CW	Continuous Wave
CZT	Chirp-Z Transform
DAC	Digital to Analogue Converter
DC	Digital Current
DDS	Direct Digital Synthesiser
DFT	Discrete Fourier Transform
DOA	Direction of Arrival
DTFT	Discrete Time Fourier Transform
EM	Electromagnetic Wave
ESM	Electronic Support Measure
FFT	Fast Fourier Transform
FM	Frequency Modulated
FMCW	Frequency Modulated Continuous Wave
IF	Intermediate Frequency
IOT	Internet of Things
KPI	Kth-order Polynomial Interpolation
LFM	Linear Frequency Modulated
LO	Local Oscillator
LPI	Low Probability of Intercept
MLCZT	Most-likelihood Chirp-Z Transform
MTI	Moving Target Indication

MVU	Minimum Variance unbiased
PD	Pulsed Doppler
PDF	Probability Density Function
PL	Processing Loss
PLL	Pulse Locked LoopF
PRF	Pulse Repetition Frequency
PRI	Pulse Repetition Interval
RCS	Radar Cross Section
RF	Radio Frequency
RMS	Root Mean Square
ROC	Receiver Operating Characteristic
SAR	Synthetic Aperture Radar
SCR	Signal to Clutter Ratio
SIR	Signal to Interference Ratio
SNR	Signal to Noise Ratio
VNA	Vector Network Analyser
VCO	Voltage Controlled Oscillator

1. Introduction

1.1 Overview

Range estimation is one of the fundamental and significant attributes of a radar system. After more than half a century's development of radar technology and theory, there are numerous techniques and algorithms nowadays to resort to achieve range estimation according to the distinctive system structures and signal processing approaches.

Coherent and non-coherent techniques are the two types of ubiquitous approaches among them to achieve the goal of range detection, and both have their advantages and disadvantages. The coherent estimate has benefits of improved precision, which may be several orders of magnitude better than the classic radar range resolution. Still, it can suffer from phase wrap errors, particularly in complex environments. In contrast to coherent technique, the non-coherent technique offers lower precision, perhaps an order of magnitude smaller than coherent, but does not suffer from phase wrap errors, so is more resilient to environmental effects such as multipath and clutter.

As a representative of a widely used radar structure, FMCW radar offers a satisfactory solution to range detection. FMCW radar systems are considerably robust, and their power consumption is substantially small to operate on considerable harsh environments. Meanwhile, miscellaneous elegant processing techniques can be applied to attain stable and precise performance, especially in terms of range estimation. Furthermore, radar measurement reduces the influence of environmental factors such as smoke, dust and debris which might surround the target, compared with laser or other sensors. Because of various merits, FMCW radars have relatively broad employment and bright prospect in enormous applications nowadays, including but not limited to environment surveillance (i.e., ice shelf monitoring [1, 2, 3, 4] and snow avalanches measurements [5, 6]), displacement measurements [7, 8], vehicles detection in urban areas [9, 10], industrial control (for example, non-contact measuring [11, 12]), indoor localisation and life detection [13] et al. Among these applications, an ice-penetrating FMCW radar system (ApRES) with phase-sensitive processing to ice shelf surveillance in the Antarctic [3] will be introduced in section 3.1.

Given the considerable potential of non-coherent detection, two purpose-built estimate techniques (the object of this thesis) are under development to improve estimate precision. K^{th} -order Polynomial Interpolation (KPI) is inspired by the processing procedures of excellent Doppler estimation mentioned in [14] and [15]. A two-stage method for the excellent ranging estimate is applied to the DFT domain. An N -point DFT is implemented to attain a rough estimate. A delicate

process is undertaken around the location of interest given by the previous procedure, through refining the estimated parameters of the objects by polynomial interpolation. The technique of Most-likelihood Chirp Z-transform (MLCZT) is inspired by the chirp Z transform [16, 17, 18], and the concept of most-likelihood estimator is presented to combine with CZT to acquire better ranging performance. Cramer-Rao lower bound (CRLB), which is the most effective unbiased variance of estimation algorithm as a benchmark for performance evaluation [19, 20, 21], is presented to assess the performance of these two techniques statistically.

1.2 Aims and Target Applications

The primary objective of the thesis is to develop two non-coherent ranging estimate techniques with novel algorithms for high-precision performance with computationally efficiency. At the same time, the initial inspiration stemmed from the research of accurate ice shelf monitoring with phase-sensitive FMCW radar.

Ice shelves in Antarctica are the unstable fringe and increment of the ice sheet. Long-term surveillance and precise detection are crucial to the prediction of sea-level rising and contribute to further research on global climate change. FMCW radar offers simple structure, decent detection performance, low power consumption and maintenance cost, and sufficient system reliability. Owing to these advantages, FMCW radar systems are particularly suitable to undertake such long-term surveillance task under the Antarctic environment. It is desired to develop a novel high-precision ranging technique with polynomial interpolation for ice shelf detection and monitoring, which provides millimetre-level performance on range estimation.

Coherent and non-coherent approaches can be applied to range estimation. Coherent estimate offers higher precision but is more vulnerable to noise and clutter and phase wrap errors, particularly in a complex or harsh environment, while the non-coherent structure is more straightforward, more robust to environmental effects such as multipath and clutter but provides lower precision. Therefore, it is reasonable to investigate a few non-coherent ranging techniques with elegant solutions to mitigate the intrinsic drawbacks of non-coherent techniques, and eventually generate high precision range estimation.

Furthermore, with the tide of technology innovation and information era, the capability of estimating the range of targets of interest effectively and precisely is of significance to a radar system, as well as its post-processing chain. Majority of applications call on high-performance range estimation with computational feasibility and efficiency. Meanwhile, it is not necessary to acquire the

range information as well the velocity or direction of the angle at the same time in specific applications; on the other hand, interdisciplinary techniques and solutions provide profound technological feasibility to current problems.

For instance, automotive radar is going to be the fastest-growing research point of interest, and it will become to one of the most promising civilian applications of radar technology, beyond classical military usage. Radar systems with features of small size and high performance on vehicles provide the potential revolution of autonomous driving [22, 23, 24]. They are the crucial part in the autonomous sensing equipment due to the current renovation of radio frequency (RF) CMOS technology that gets access to advanced radar-on-chip integration and solution; its reduced cost provides the possibility to mass production on consumer-level [25, 26].

Besides, with the development of the 5th Generation communication networks, the time delay of real-time cloud computing has been significantly reduced, less than one microsecond [27, 28]. However, it would not be sufficient with the absence of high spatial detection performance. The high-performance ranging techniques will be widely used on massive MIMO systems and autonomous vehicles, for detection and obstacle avoidance [29, 30, 31].

High-performance ranging techniques and algorithms can also be implemented to distinctive realms of applications, such as wearable sensing equipment [32, 33], Internet of Things [34, 35], collaborative situational awareness [36, 37], and radar-communication integration [38, 39, 40].

Desired target applications can be divided into two distinctive perspectives, civil usages and military applications. There are broad applications for precise range detection in the civil field, especially in civil construction, i.e., underground and skyscraper constructions. Owing to the considerations of the safety, precise range detection can be applied to monitor the incline from buildings' virtual middle axis via the wind or other turbulence/destabilisation. Other featured civil usages lie on the smart transportation and the Internet of Things. The high-precision ranging techniques can be also applied to military scenarios as well for sure. For examples, guided missile, automatic target recognition, collaborative situational awareness, active/passive radar early warning & surveillance networks, and battlefield information link.

1.3 Novel Contributions and Publications

The primary contributions of this research are concluded to four perspectives:

- Investigation of non-coherent and coherent discrete target range estimation techniques and making a comparison to each other for pros and cons under scenarios of distinctive environmental factors and various applications;
- Development of a non-coherent ranging technique of peak detection by K^{th} -order Polynomial Interpolation (KPI). A two-stage approach for the excellent ranging estimate is applied to the DFT domain of both KPI and following MLCZT algorithms to achieve accurate interpolation and optimum precision. Mathematical derivation, simulation modelling, theoretical and experimental analysis are implemented to evaluate its performance;
- Development of a non-coherent ranging technique of Most-likelihood Chirp Z-transform (MLCZT). The concept of most-likelihood estimator is introduced to combine with CZT to acquire better ranging performance. Mathematical derivation, simulation modelling and theoretical analysis are conducted to assess its representation;
- Derivation and analysis of the mathematical expressions of the Cramer-Rao lower bound (CRLB) of K^{th} -order Polynomial Interpolation (KPI) and Most-Likelihood Chirp Z-transform (MLCZT) techniques.

The plan of publication will also be described as follow. Two papers are intended to compose based on the research works.

One paper concentrates on the polynomial interpolation technique and the paper is targeting at top tire journals, i.e., IET Radar, Sonar & Navigation, IEEE Transactions on Aerospace and Electronic Systems, and IEEE Transactions on Signal Processing.

Another one focus on the most-likelihood chirp-Z transform technique and the paper is aiming to a conference paper, e.g., IET International Conference on Radar Systems and IEEE Radar Conference.

1.4 Thesis Organisation

This thesis is composed of eight chapters, firstly the introduction, including overview, inspiration and aims, novel contribution, and thesis structure. The second chapter discusses the relevant theory required for current research, consisting of radar theory (mainly focusing on Doppler radar and FMCW radar) and the range estimation theory, which initially a summary regarding range equations and then

range resolution, finishing off with descriptions about the maximum unambiguous range and range performance. A preview of basic radar signal processing is presented and then estimation theory of statistical signal processing. Several important concepts are introduced for the following discussion, i.e., PDF, MVU estimator and CRLB.

Chapter 3 introduces several prevailing ranging techniques for high-precision performance. It begins with the process of I/Q detection of coherent ranging technique and introduces an ice-penetrating FMCW radar (ApRES) with the phase-sensitive process. FMCW radar literature is analysed with how current systems are designed, and both advantages and disadvantages are discussed against non-coherent detection. Then non-coherent technique and an MTI system are presented, and the ROC curve is introduced to evaluate the performance of radar detectors. The rest of the chapter describes three mathematical transformation tools that will be used in the following chapters, namely, Fourier transform, Z transform, and Laplace transform.

Chapter 4 presents two novel non-coherent ranging technique by Peak detection. A two-stage approach for the fine ranging estimate is applied to the DFT domain to achieve accurate interpolation and optimum precision. Method description is introduced, following with the algorithm realisation by KPI, which is one of the main works on the thesis. Polynomial interpolation is expounded, including the procedures of processing and the configuration of the parabolic, cubic and quartic functions. Then a general equation for K th-order polynomial fit is derived and given eventually. Another non-coherent ranging technique uses chirp Z transform. The basic concept of Z transform is introduced firstly, following with the algorithm realisation by MLCZT. The CZT accurately implements the periodogram, and only a narrow band spectrum is processed. The concept of most-likelihood estimator is introduced to combine with CZT to acquire better ranging performance.

Mathematical expressions of CRLB of KPI and MLCZT algorithms are derived in chapter 5. It contains the majority of mathematical proofing and derivation of all parts of the thesis. The vector form of CRLB is firstly introduced, then the derivation of asymptotical CRLB under the distinctive circumstance and SNR regarding two techniques, respectively. A mathematical derivation is also presented to validate the most-likelihood method in the CZT at the end of this chapter.

Chapter 6 analyses the results and data obtained by simulations, beginning with pre-processing the acquired raw time-domain data, then the processing results of polynomial interpolation and most-likelihood chirp-Z transform technique as well. Relative drawbacks and improvements are discussed from several aspects under different conditions.

Experimental results and discussion are presented in chapter 7. Window functions are introduced to evaluate and analyse the performance of these techniques. Further results of polynomial interpolation are presented as well. At the rest part of the chapter, coherent and non-coherent ranging approaches are compared based on experimental data to summarise several advantages and disadvantages as conclusions for further research.

The final chapter, chapter 8, concludes the thesis and proposes the plan of future work. It summarises the whole thesis and goes on to convey the next steps needed to be taken to improve the range accuracy of non-coherent estimation. Further research will be kept pushing forward to develop and trial a location system using non-coherent techniques, and a few thrilling points of interest with the tide of technological renovation, such as the application of deep learning in radars and digital radar structures. There are also several appendices after the conclusion, including parts of the Matlab codes from related works of the thesis.

2. Background Theory

This chapter introduces the theoretical knowledge needed for the rest of the thesis. It describes the relevant radar theory tailored to the fundamentals of radar systems, such as substantial principles and elements of a basic radar system. Then Doppler radar is introduced as two sections, continuous wave (CW) and pulsed-Doppler radars. After that, FMCW radar systems are introduced, because they allow the measurement of range whereas Continuous Wave (CW) systems do not. FMCW systems also lead to the low initial and maintenance cost, and high reliability, compared with the pulsed-Doppler radars. Furthermore, system structure and other advantages of FMCW radars are discussed. The last part of this chapter describes the essential knowledge regarding range estimation, including the derivation of radar range equations, range resolution and unambiguity, which is related to the following contents in chapter 3. The majority of the theory introduced in this chapter refers to [41], [42], [43], [44], [45], [46], and [47].

2.1 Radar theory

The majority applications of radar systems can be categorised to detection, tracking, and imaging. The essential but crucial task among them is the detection of a target and measuring its range towards the radar itself and the velocity as well. This requires distinguishing that the receiver signal at a given interval demonstrates the transmitted signals from the targets of interest with environmental and artificial noise.

2.1.1 Essential Radar Functions and Elements

Target detection is typically implemented via measuring the amplitude $A(t)$ from the receiver chain (t refers to time) to a preset threshold $H(t)$, which is one of the priorities in terms of a radar. Taking a most basic case as an example, for a discrete point target, the time needed to radiate a space R and go back (travelling the distance $2R$ totally), can be presented to $2R/c$; therefore, if $A(t) > H(t)$ at a particular time delay τ after the transmission of a pulse, the target is present at a range

$$R = \frac{c\tau}{2} \quad (2.1)$$

After the indication of the presence of an object, it is therefore natural to detect its coordinates and velocity. Taking a monostatic radar as an example, it measures position in a spherical coordinate system. For analysing conveniently, we can presume that it locates at the phase center of its radar antenna, illustrated in Figure 2.1. In the frame of axes illustrated below, the look direction (boresight direction) of the antenna, is towards to $+x$ axis. ϕ is the elevation angle, while θ is the azimuth angle. The range R follows directly from a specific time interval between transceivers as mentioned. The angles of Azimuth θ and elevation ϕ depend on the antenna orientation because the object should be generally located within the main beam of the antenna to be detected. In general, velocity is estimated by detecting the Doppler shift of the received signal from the object. Although Doppler shift merely distinguishes the radial velocity component, various techniques of positioning and determination of radial velocity are applied to attain the object's coordinates in all three dimensions.

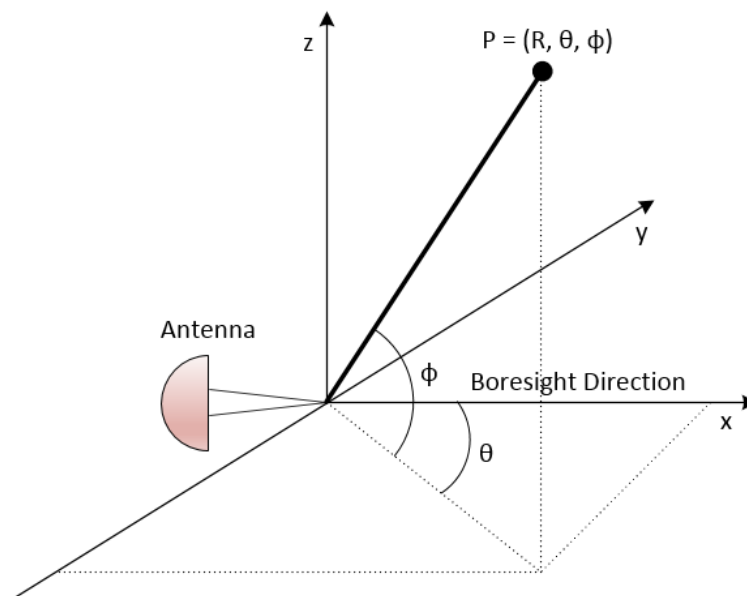


Figure 2.1 Spherical coordinate system for radar measurement

Meanwhile, radar systems have prevailing applications of imaging with two-dimensional form. Civil information and even military intelligence can be extracted from those images, such as geographical mapping, mining detection, avalanche warning, surveillance assignment, and so forth. Radar imaging is not the subject of this thesis, it is, therefore, unnecessary to go into details.

The performance of radar can be evaluated by considerable figures of merit, according to the functions and applications. In terms of the estimation of performance, the primary indices are the

probability of detection P_D and the probability of false alarm P_F . When the rest of the system parameters are fixed, the higher P_D is, the higher P_F follows. The practical trade-off is therefore established through the signal and interference characteristics, for instance, the signal-to-interference ratio (SIR). If several objects of interest occur in the detection range of the radar system, extra considerations of resolution and side lobes originate from evaluating the related performance of such detection. The issues as side lobes and resolution in range depend on the transmitting waveform, while others in angle depend on the antenna pattern.

Figure 2.2 is the illustration of a primary pulse-monostatic radar. The desired waveform of the pulse signal is produced through the waveform generator, and this waveform is modulated via a transmitter to the required radio frequency (RF), and then augments the signal to a specific extent. The outcome of the transmitter is sent to the antenna via a transmit/receive switch. The signal received by the antenna flows again through the T/R switch and gets to the receiver chain. A receiver is typically super-heterodyne form, with a low-noise RF amplifier as its first stage. Several modules may be required to modulate the received signal to intermediate frequencies (IF) and baseband. Modulation is conducted with a local oscillator (LO) and a mixer. Signal processors are the following destination for these baseband signals. Numerous functions like pulse compression, matched filtering, and error compensation, are implemented in here. According to different applications, the output of the signal processor may have varied forms. For instance, an imaging radar may generate multi-dimensional images while a tracking radar will produce a series of estimations indicating to the range and angle coordinates. Eventually, the processor result is routed to the module of display or even further processors for signal data.

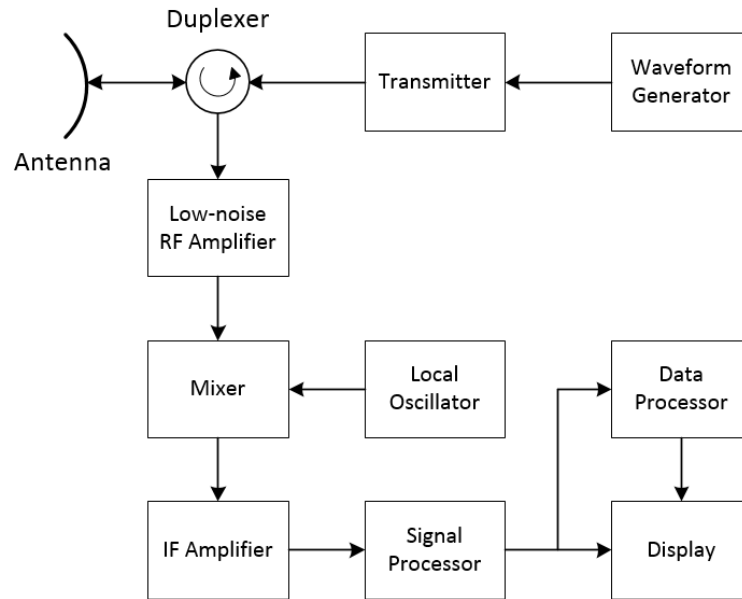


Figure 2.2 An illustration of a pulsed monostatic radar [41]

The configuration of Figure 2.2 is not ubiquitous. For instance, numerous systems process signals at intermediate frequencies, not baseband (i.e., Doppler filtering). Another distinction may lay on the node where the signal is digitised in radar. For instance, previous radars were all typically analogue, and many current radar systems do not convert the signal into digital form until baseband. What is to say that any processing undertaken at intermediate frequencies must be done with analogue techniques. Nowadays, radar systems digitise the signal at an intermediate frequencies zone (e.g., several hundred kilohertz), and then send to the A/D converter and implement the digital process at intermediate frequencies.

2.1.2 Doppler Radar

The term Doppler radar refers to a radar that can detect the Doppler frequency in comparison to the transmitted and received signal [49]. The shift in frequency relates to the radial component of the target motion is referred to as the Doppler frequency. Doppler radars are used most often to discriminate between the return from the desired target, usually moving, and that from undesired objects generally ground clutter, usually not moving [50, 51].

Figure 2.3 depicts the different types of Doppler radar. The optimum choice is dependent on the operational requirements of the specific radar system. Considerable radars are required to perform over a sufficiently broad range of circumstances; therefore, no single type is universally acceptable.

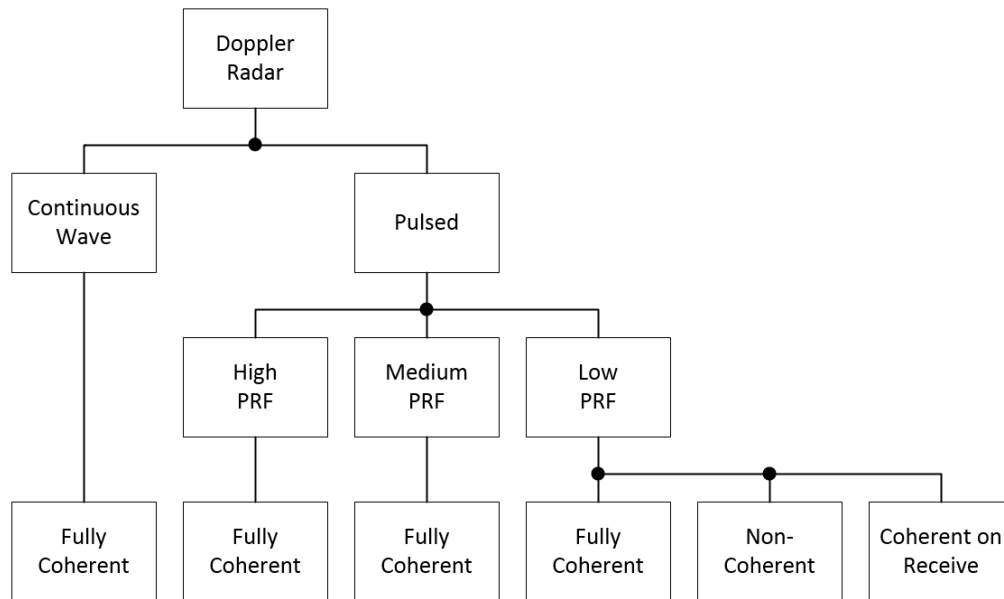


Figure 2.3 Types of Doppler radar

Continuous wave (CW) radars, as the name itself implies, transmit and receive a continuous waveform. Figure 2.4 demonstrates a simplified block diagram, where f_D is the Doppler shift for moving objects (the logo of UCL is used here presenting as a still target). In high-power CW radar system, separate transmit and receive antennas, which have adequate isolation between them, are required to prevent receiver desensitisation.

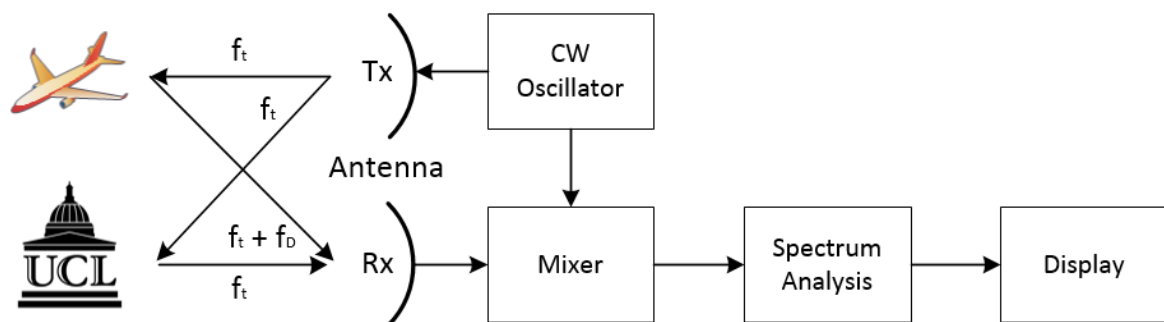


Figure 2.4 A simplified illustration of CW radar

CW radar can be analysed as a pulse radar, illustrated in Fig. 2.5, by adding a pulse modulator, as well as a power amplifier. A few numbers of the CW oscillator transmit pulses to the receiver directly, and it operates just like a coherent beacon to estimate the shift of Doppler frequency. 'Coherent' indicates that the phase of the transmitted signal is implemented to a reference or benchmark, which is the distinctive characteristic of coherent pulse-Doppler radar and applied to the following processing.

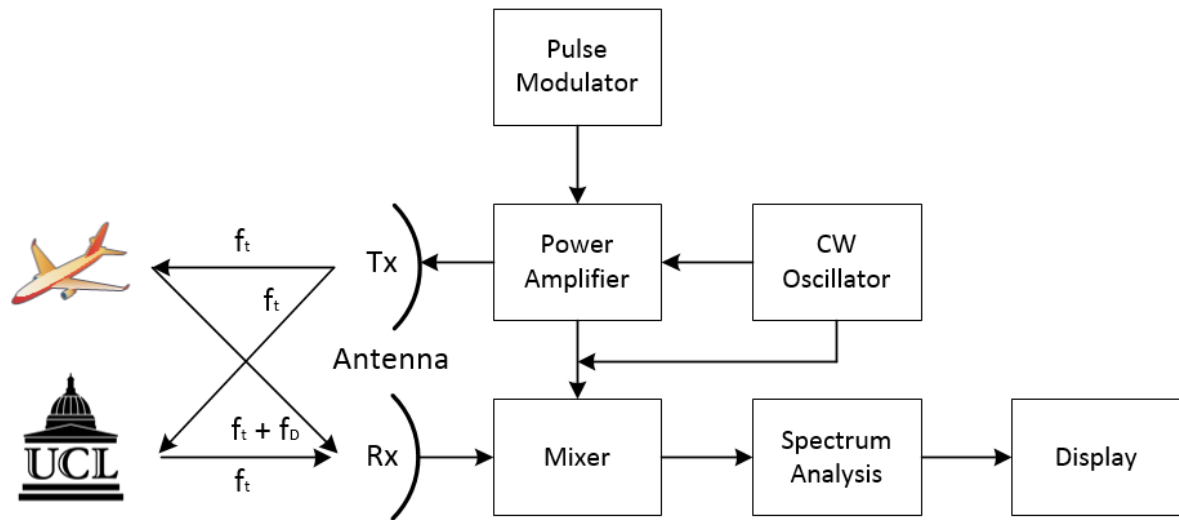


Figure 2.5 A simplified illustration of a pulse-Doppler radar

Table 2.1 describes the three waveforms used in pulsed Doppler radar. Each of the waveforms possesses significant differences in performance. Numerous modern radars are 'multimode'; that is, they can operate using two or more of the waveforms shown below.

Table 2.1 Distinctive modes of pulsed Doppler radars

Mode	Range	Velocity
Low-PRF	Unambiguous	Usually ambiguous
Medium-PRF	Ambiguous	Ambiguous
High-PRF	Highly ambiguous	Unambiguous

Low-PRF Radars

Low-PRF radars are generally designed to detect the range unambiguously, operating on a substantially low pulse repetition frequency (PRF). The transmitted pulse propagates towards and from the maximum range during the inter-pulse interval, before transmitting the next pulse. The unambiguous range R_u can be presented to

$$R_u = \frac{c}{2PRF} \quad (2.2)$$

where c is the speed of the light.

High-PRF Radars

High-PRF radars are typically applied to unambiguously estimate velocities of the object, with a PRF sufficiently high. The maximum Doppler shift that can be unambiguously distinguished can be expressed as

$$f_{dmax} = \frac{PRF}{2} = \frac{2fV_u}{c} \quad (2.3)$$

in which f is the transmitter frequency, and V_u is the total closing velocity.

Medium-PRF Radars

Medium-PRF radars are defined as radars with a PRF that produces ambiguous in range, as well as in Doppler. Medium-PRF seems to gather the worst features of both high and low-PRF radars. However, medium-PRF is usually the best option of the waveform for airborne radar. The equation for unambiguous range R_u and unambiguous velocity V_u are both functions of the PRF. Either of them is, therefore, cannot be independently chosen.

Doppler and Range Ambiguities

Doppler shift lies on the frequency between the transmitted radio frequency (RF) carrier and the echoes reflected from moving objects [51]. Consider a target at a range R . The round-trip distance is $2R$, and the total phase distinction among the transmitted and received wave is presented as

$$\phi = -2\pi \left(\frac{2r}{\lambda} \right) \quad (2.4)$$

where the negative sign indicates a phase delay. Using the definition of frequency,

$$f = \frac{1}{2\pi} \left(\frac{d\phi}{dt} \right) \quad (2.5)$$

The change in frequency (i.e., the Doppler shift), seen at the radar, resulting from a target with changing range, is given by

$$f_d = -\frac{2}{\lambda} \left(\frac{dR}{dt} \right) = \frac{2v}{\lambda} \quad (2.6)$$

Equation (2.6) shows that any magnitude of object speed is capable of estimating. However, based on the Nyquist criterion, the minimum sampling frequency required to reconstruct precisely the frequency component of a signal is equivalent to twice the signal bandwidth. In terms of pulsed radar, the sampling frequency is the pulse repetition frequency (PRF). In contrast, a CW radar is subject to the same sampling consideration with sampling and using digital spectrum analysis. The radar that extracts two samples each pulse repetition interval (PRI) samples twice rate as the PRF and presents an unambiguous frequency interval of PRF (I.E., I and Q channel, which will be introduced in details at section 3.1.1).

Equation (2.4) suggests the total phase delay among the transmitted and received waveforms. The phase change between pulses (samples) is

$$\Delta\phi = 2\pi \left(\frac{2\Delta R}{\lambda} \right) \quad (2.7)$$

where ΔR is the range change between pulses.

If the phase variation between pulses is no more than 2π , the Doppler frequency can be unambiguously detected. If the phase variation is equivalent to 2π , the Doppler frequency is worth to the PRF. A shift of 2π obviously will not be discerned among a shift of any integral multiple of 2π (including zero). The speed that generates the Doppler shift to be an integral multiple of 2π has been historically called blind speeds [52]. And if the phase variation is larger than 2π , the targets will generally be recognised, but the estimated Doppler shift will not appropriately correspond to the target speed. The received Doppler frequency will be faulty by an integral multiple of the PRF. Multiple PRFs are used to block the effect of blind speeds and to distinguish ambiguous target speed detections [53, 54].

The Doppler shift observed by a pulsed radar is more accurately given by modifying the equation (2.6) to read

$$f_d \equiv \frac{2v}{\lambda} (\text{mod } PRF) \quad (2.8)$$

where 'mod' is an abbreviation of modulo, presenting the remainder after dividing one number by another.

Besides, for a pulsed-Doppler radar, when the same antenna is applied to high-power transmitting and receiving, the radar receiver must be turned off during transmission. The receiver off time must be long enough for the transmitter energy to decay to levels that do not harm the receiver and is, therefore, longer than the 3-dB transmitter pulse width. The result is a blind range which can be substantial in radars that use pulse compression.

Targets at ranges more significant than the unambiguous range R_u and not at a blind range may be detected. The observed apparent range R_a will be faulty by an integral multiple of R_u and is shown by

$$R_a \equiv \frac{c\tau}{2} (\text{mod } R_u) \quad (2.9)$$

where τ is the propagation time to the target.

2.2 Frequency-modulated Continuous Wave Radar

To achieve a relatively desired performance on "Low Probability of Intercept" (LPI), CW transmitters are implemented to replace the pulsed transmitters. CW radar systems utilise low continuous power (though working at 100% duty cycle) in terms of the high peak power of pulsed radars to achieve a similar performance of estimation and detection. However, because of the application of the unmodulated waveforms, CW radars cannot attain the range information from the echoes of objects. There is no reference "beacon" among the transmitted and echo signals to indicate the time delay as in a pulsed-Doppler radar. Specific sort of timing mark is required to a continuous wave carrier to fulfil the function of range estimation. This indicator distinguishes the time of return from the time of transmission—the more distinctive the indicator, the more precise the estimation of the transition interval. However, based on the Fourier transform, the sharper the benchmark, the broader will be the transmission spectrum. Therefore, a finite spectrum is required to transmit relative waveform to attain the range estimation.

The spectrum of a continuous wave transmission can be extended through the modulation of amplitude, frequency, and phase. Pulsed radars are examples of the amplitude modulation: the narrower the pulse, the more precise the estimation of range and the wider the transmitting spectrum. Frequency modulation is widely implemented to extend the spectrum of a CW system. The timing indicator is, therefore, the variational frequency. The conveying time of the electromagnetic wave is proportional to the variation in frequency among the received and transmitted signal. The more considerable the transmitted frequency variation in a given period, the more precise is the estimation of the time interval, and the larger will be the transmission spectrum. Consequently, radars applying this technique are named as FMCW radars and the waveform used here for signal processing is described as the “chirp” signal.

2.2.1 System Summary

Frequency modulation can be implemented in various forms and applications in radar systems, while linear modulation is the most versatile among them. Meanwhile, it also pretty matches with the FFT process to attain range estimation. Since the frequency of the transmitting signals is linearly varied over time, there is a certain distance among the radar and objects, and the reflected signal varies in frequency compared to the currently transmitted frequency. To extract the distance parameter of an objective, the difference in frequency, called beat frequency between the transmitting and the receiving signal is evaluated [57]. A simplified diagram of a typical FMCW system is demonstrated below.

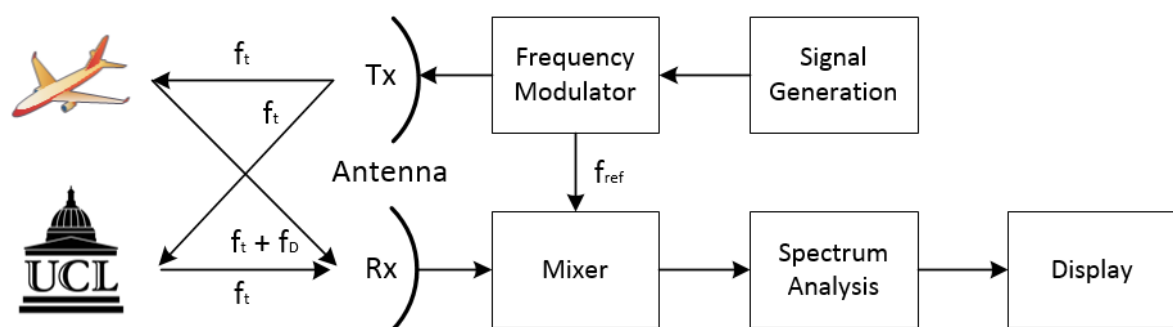


Figure 2.6 A simplified illustration of FMCW radar

An FMCW radar concludes a “chirp” signal generator, transceivers, mixers, spectrum analysis and signal processing sections, and display devices. The transmitted “chirp” signal of high frequency is generated by a voltage-controlled oscillator (VCO) or a direct digital synthesiser (DDS), which transmits to generated signal directly to the transmitting antenna (can be amplified for specific scenario of power). There are perhaps several low noise amplifiers (LNA) after the receiver antennas, before the signal flowing to the mixer. The spectrum analysis and signal processing sections contain a set of filters and amplifiers to accomplish compact post-process procedures, then leading to the results display of the target’s velocity, as well as range.

An FMCW radar is generally applied to estimate the velocity and range of objectives simultaneously, which subjects to the FMCW ambiguity function for sure. Meanwhile, FMCW systems acquire considerably high accuracy on ranging, and they can detect slight ranges to the target (minimal measurable range compared to the transmission wavelength). Besides, signal processing of FMCW radars after mixing is implemented at an intermediate frequency limit, vastly simplifying the realisation of the post-process hardware.

The range resolution of an FMCW radar individually relies on its frequency-sweeping bandwidth [58]. If the bandwidth increase, the practical range resolution drops and the maximum unambiguous range reduces as well. Meanwhile, the antennas bandwidth determines the angular resolution in detection within the allocated bandwidth. Furthermore, the product of frequency and phase evaluation can be integrated to attain the pre-set performance in the sub-millimetre range [59, 60]. After rough estimation via the frequency, a correction is achieved through the evaluated phase information unambiguously of half the wavelength [61]. The performance of an FMCW radar system can be assessed with sensitivity and range resolution, with consideration of critical contaminating effects. Sensitivity and range resolution are critical components of the SNR and signal-to-clutter ratio, which determine the overall radar system performance.

2.2.2 Advantages

As mentioned above, FMCW radar systems allow the measurement of range whereas continuous wave (CW) systems do not. For an FMCW radar, the transmitting frequency varies through the time, and the frequency of the echo signal from the object is attained. The beat frequency and the phase are individually proportional to the range of the object [62]. Objects information on both range and Doppler domains can be implemented through mixing the return signal with the transmitting signal.

The frequency modulation over a modulation bandwidth ΔF presents decent range resolution, which is crucial to target recognition among clutters.

In a homodyne FMCW radar configuration, the LO signal is coupled from the transmit signal, which avoids the need for a separate oscillator. The resulting cost and volume savings make the homodyne FMCW radar structure attractive for the low-cost systems. FMCW radars operate at a much lower peak output power when compared to PD radar systems, due to the substantial processing gain.

FMCW technique has the advantage of simple solid-state transmitters so that such systems operate on low initial cost, low maintenance costs, and high reliability as well. It permits a broad transmitting spectrum for multiply applications which grants decent range resolution without the auxiliary of processing very short pulses. The requirement of frequency modulation can be implemented conveniently than the modulation of short pulses. FMCW modulation is therefore desirable to applications demanding the minimal system consumption, because of giving a radar an extremely high time-bandwidth product and allowing a right combination of operating range and range resolution with just a simple way [63, 64]. In terms of low-power consideration, FMCW structure presents the most straightforward transceiver designs of any radar which can provide range estimation, despite the relative trade-off to fulfil functions as frequency analysis on the IF spectrum [65]. Meanwhile, considering the complexity of signal processing, FMCW systems implement the range estimation via the digitised intermediate frequency (IF) signals. It can be quickly processed with the fast Fourier transform (FFT).

Moreover, from perspectives of LPI, the power spectrum of the FMCW signal is similarly rectangular within the bandwidth of modulation, which is difficult to be intercepted by non-cooperative form. FMCW radars are therefore much harder to be detected by the electronic support measures (ESM) systems. On the other hand, the waveform of transmission in an FMCW radar is deterministic, the pattern of the received signals can be predicted due to the foreknowledge. It provides the resistance to jamming in that any signal which is not matched to the specific form that can be suppressed in the course of the process. Furthermore, FMCW radar measurement reduces the influence of environmental factors such as smoke, dust and debris which might surround the target, compared with optical sensors such as a camera or laser, and therefore have profound usage from industrial applications, civilian employment to even climate surveillance, for example, Antarctic ice shelf profile monitoring (see section 3.1.2).

2.3 Fundamentals of Range Estimation

Ranging is an essential and crucial issue for the majority of radar systems. How to solve the range-detection problem effectively and precisely is massively important, especially taking every factor into considerations, such as the power level of a received echo signal to the pertinent characteristics of radar systems, the antenna patterns, the wave-propagation medium, and the characteristics of the target. Moreover, high resolution and unambiguity of range estimation are the points of interest as well.

2.3.1 Radar Range Equations

As known, the radar equation for a point-target in free space is

$$P_r = \frac{P_t G_t G_r \sigma \lambda^2}{(4\pi)^3 R^4} \quad (2.10)$$

where P_t and P_r are receiving and transmitting power respectively, G_t and G_r are the gain of transmitting and receiving antenna respectively, σ is the radar cross-section (RCS) of the object, λ is the wavelength, and R is the target range towards the radar itself in metres.

The quantities on the equation's right side either are standard parameters of a radar system or can be detected or otherwise evaluated. However, caution is necessary if the equation is used for obtaining engineering information because not all the parameters on the right side are mutually independent. It might be particularly thought that the equation states that P_r is proportional to λ^2 . Meanwhile, some of the other factors in the equation are implicitly wavelength-dependent. Wavelength dependence also means frequency dependence since wavelength and frequency are related in free space by the equation

$$\lambda = \frac{c}{f} \quad (2.11)$$

where c is the wave velocity.

When it does not meet the circumstances specified for free-space propagation, equation (2.3) can be re-written as

$$P_r = \frac{P_t G_t G_r \sigma \lambda^2 F_t^2 F_r^2}{(4\pi)^3 R^4} \quad (2.12)$$

where F_t is the pattern propagation factor of transmitting, and F_r is the pattern propagation factor of receiving.

This is the radar equation without the free-space restriction. When the identical antenna is applied to transmit and receive, thus $G_t = G_r$ and $F_t = F_r$, and the equation can be written

$$P_r = \frac{P_t G^2 \sigma \lambda^2 F^4}{(4\pi)^3 R^4} \quad (2.13)$$

This is the form in which it was initially written by [41]. It includes the free-space situation as a particular case. For that case, the pattern propagation factor becomes simply the magnitude of the pattern factor $|f(\theta, \phi)|$. And additionally, when the target is in the beam maxima, the pattern factors become unity.

In principle, equation (2.12) is an entirely general transmission equation for monostatic radar and point targets. However, in engineering usage, the loss factor L of a two-port (i.e., a transmission line) and various losses may need to be considered, such as atmospheric loss. It is the reciprocal of the definition of the gain of a two-port. For a lossy two-port, $L \geq 1$. Therefore, if the loss factor L_t is placed in the denominator of the transmission equation, the quantity P_t can be defined as the power output of the transmitter. Considering a variety of loss factors together into a system loss factor L , the radar transmission equation now is

$$P_r = \frac{P_t G_t G_r \sigma \lambda^2 F_t^2 F_r^2}{(4\pi)^3 R^4 L} \quad (2.14)$$

Monostatic Radar Range Equation

According to the transmission equation provided above, a rudimentary radar range equation is presented through merely re-arranging the transmission expression as shown

$$R = \left[\frac{P_t G_t G_r \sigma \lambda^2 F_t^2 F_r^2}{(4\pi)^3 P_r L} \right]^{1/4} \quad (2.15)$$

This is not an equation of maximum range; it merely demonstrates that if the quantities on the right side have specified values, the target range will be given by the equation above theoretically, while this is not how the range is measured in practical applications.

The radar has a maximum useable range. As the range increases, a point is ultimately reached at which P_r decreases to the value of $P_{r(min)}$, and does not, therefore, rise above this value. Therefore, the equation can be adjusted as below

$$R_{\max} = \left[\frac{P_t G_t G_r \sigma \lambda^2 F_t^2 F_r^2}{(4\pi)^3 P_{r(\min)} L} \right]^{1/4} \quad (2.16)$$

with the understanding that in some situation P_r may have the values $P_{r(\min)}$ at more than one range, in which case R_{\max} is the largest range under such circumstances.

Expanded Radar Range Equation

The significant factor in analysing the signal detection is not the power of signal itself, but the signal-to-noise power ratio, designated S/N (sometimes called 'SNR' as well). The minimum-detectable signal power $P_{r(\min)}$ is expressed by the minimum-detectable signal-to-noise power ratio $(S/N)_{\min}$

$$P_{r(\min)} = (S/N)_{\min} P_n \quad (2.17)$$

where P_n denotes the power level of the noise in the receiver circuits. P_n can be written as

$$P_n = N_0 B_n = k T_s B_n \quad (2.18)$$

where N_0 is the noise power per unit bandwidth, B_n is the 'noise bandwidth' of the receiver, k is the Boltzmann's constant ($1.38 \times 10^{-23} \text{ W} \cdot \text{s/degree}$), and T_s is the system noise temperature in Kelvins (K). Therefore, based on the equation (2.19)

$$P_{r(\min)} = (S/N)_{\min} k T_s B_n \quad (2.19)$$

This expression can be substituted in equation (2.8) to obtain a new equation as

$$R_{\max} = \left[\frac{P_t G_t G_r \sigma \lambda^2 F_t^2 F_r^2}{(4\pi)^3 (S/N)_{\min} k T_s B_n L} \right]^{1/4} \quad (2.20)$$

Subject to the qualification that $(S/N)_{\min}$ here means the value applicable at the antenna terminals.

General Radar Equation

Although the equation (2.20) can be considered to a general equation in the sense that it is not limited to pulse waveforms, it is not recommended for general use because $(S/N)_{\min}$ does not refer to the SNR at the detector terminals. Therefore, the results of detection theory cannot be directly applied to it unless the receiver filter is matched to the transmitted waveform. Admittedly, the mismatch is seldom severe in well-designed radars. Nevertheless, a potentially significant error can

occur when equation (2.20) is used if $(S/N)_{min}$ is interpreted to be required the value at the detector input and if the filter is mismatched.

However, an appropriate general equation can be obtained if the product $P_t\tau$ in equation (2.20) is replaced by the transmitted waveform energy E_t . Then, with suitable definitions of E_t and D_0 , the result is a genuinely general radar equation

$$R_{max} = \left[\frac{E_t G_t G_r \sigma \lambda^2 F_t^2 F_r^2}{(4\pi)^3 k T_s D_0 C_b L} \right]^{1/4} \quad (2.21)$$

If a repetitive or quasi-repetitive waveform is transmitted, whether it is periodic pulses, pulse bursts, or any other waveform, then the appropriate matched filter is defined concerning some finite time interval of this transmitted waveform. For simple pulse radars, this time interval is usually the duration of a single pulse, and “matching” then consists simply of designing the pre-detection filter to have the appropriate bandwidth and pass-band shape. For pulse-compression radars, a feedback integrator may be implemented to decrease the SNR, at the cost of requiring a longer time of measurement for the detection process [66].

In these terms, therefore, it is seen that equation (2.21) can be regarded as a general radar equation, with E_t defined as the transmitted energy for which the receiver filter is matched (at least approximately). If the matching is not perfect, then C_b must be assigned a value greater than unity to account for this equation.

2.3.2 Range Resolution and Maximum Unambiguous Range

Fourier processing provides a means for radars to evaluate the frequency components of the received signal, including stationary and moving targets. In a pulsed-Doppler application, the radial component of velocity of the moving targets is determined by measuring the Doppler frequency, which an ideal response from a target has a specific Doppler frequency shift. High-resolution range estimation of radar targets can be achieved through elegant processing of the received signal. Numerous techniques are applied to attain a high-resolution performance of the target in the range dimension, which all requires adequate bandwidth for resolution consideration [67].

In the simplest case of a pulse transmitted without phase or frequency coding, the range resolution can be determined by

$$R_r = \frac{c\tau}{2} \quad (2.22)$$

where R_r is the range resolution in metres, and τ is the pulse length in seconds.

In the more general case, the processed pulse width will be asymptotically the reciprocal of the signal bandwidth, and the related range resolution will be

$$R_r = \frac{c}{2B} \quad (2.23)$$

where B is the bandwidth in Hertz [68].

As mentioned in section 2.2.1, the range measurement of an FMCW radar is achieved by differentiating the frequency of the received signal to a reference one (transmitted signal itself). Meanwhile, the transmission waveform T is considerably more significant than the demanding receiving time for the pre-set interval of ranging. The range R from the object to radar is therefore written as

$$R = \frac{c|\Delta f|}{2 \frac{\delta(f)}{\delta(t)}} \quad (2.24)$$

where c is the light speed, Δf is the frequency difference (Hz), and $\delta(f)/\delta(t)$ is the frequency shift per unit of the time.

If the frequency variation is linear throughout the time, the range estimation can be calculated by a simple frequency distinction, which means the frequency variation Δf is precisely proportional to the range R . In a static scenario, which doesn't have the Doppler effects, the consequences are at a linearly expanding frequency equivalent to the frequency reduction, because only the absolute amount of the frequency variation can be detected.

If the target has a radial speed to the radar, the received signal acquires a Doppler frequency f_D . Then the radar echo contains not only the difference frequency Δf to the previous frequency (caused by the runtime), but an additionally Doppler frequency f_D . The estimation depends on the motion direction of the objective and the direction of the linear modulation as well. It is only the variation among the varied frequencies as the carrier of the range information, and that of the Doppler frequency as a carrier of the velocity information. For instance, if the detection is implemented within a falling edge of the transmission waveform, the Doppler frequency f_D is deducted by the variation of runtime frequency; while the received signal frequency is deducted by the Doppler frequency f_D if the object is going away from the radar.

In terms of an FMCW radar, the maximum non-ambiguous range is determined by the duration of the frequency increase. The maximum frequency shift and steepness of the edge can be designed through the capabilities of different circuits. It is known that the bandwidth of the transmitted signal is decisive to the range resolution of FMCW radar. Nevertheless, the computational feasibility of the Fast Fourier Transformation (FFT) is restricted in time.

2.4 Previews of Basic Radar Signal Processing

After the introduction of the essential elements of typical pulsed and CW radar systems, a summary of signal processing implemented in the radar receiver chain is going to be presented.

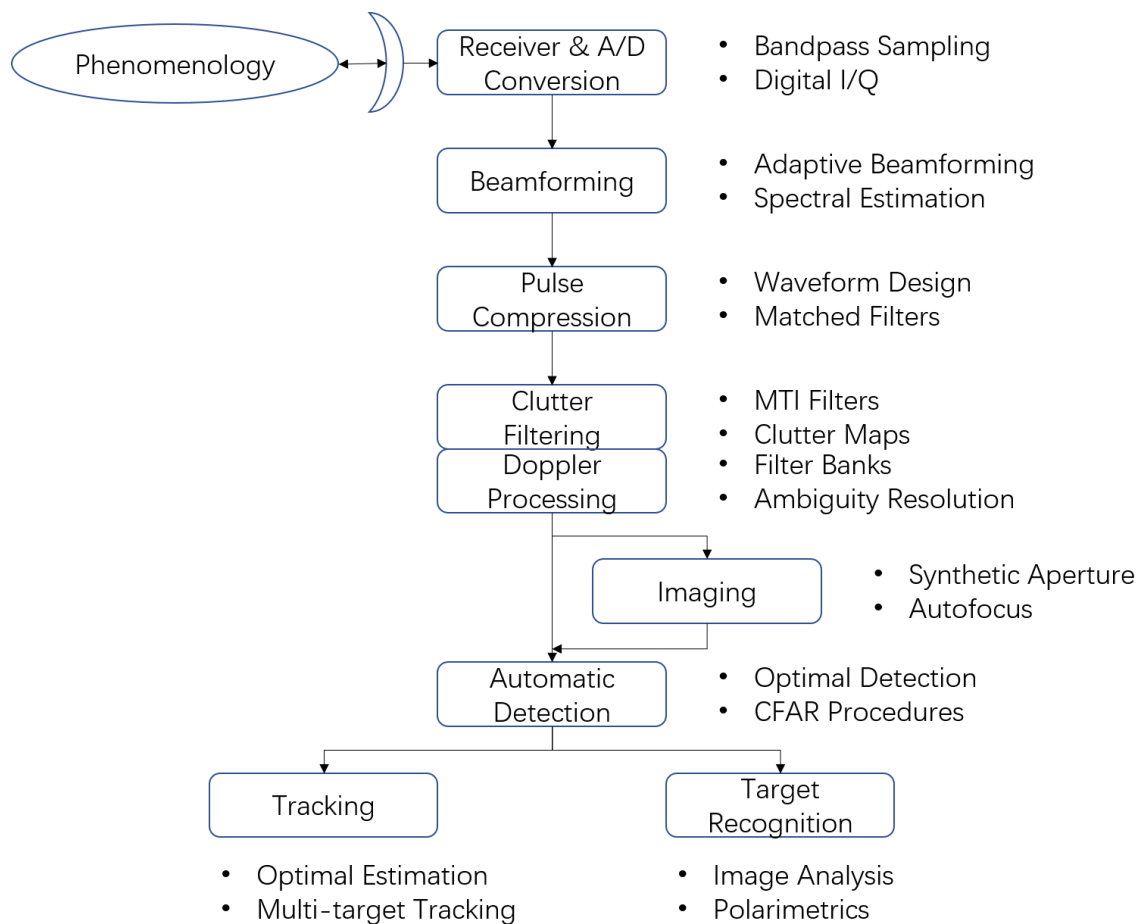


Figure 2.7 A typical flowchart of radar signal processing

Figure 2.7 demonstrates a procedure flowchart in a typical radar signal processor. Such processing techniques are not ubiquitous, nor is the series of techniques thoroughly. Additionally, where the signal is digitised in the processing chain differs from systems; it might take place as the latter approach before the outcome of clutter filtering.

2.4.1 Radar Time Scales and Phenomenology

Signal processing of radar systems occurs on time scales, and distinctive categories of techniques perform on considerably varied time scales. Process techniques can be referred to as fast time because the sample rate, determined by the instantaneous pulse bandwidth when applying to data from a signal pulse on the shortest time scale [71]. Typically, fast time techniques include digital I/Q signal formation [72], beamforming [73, 74], pulse compression [75, 76], matched filtering [77], sensitivity time control, and so forth.

The sampling interval among pulses that is PRI is generally on the order of a few microseconds to tens of milliseconds, because of the much slower sampling rate in terms of single-pulse processing (in slow time). Representative techniques contain coherent and non-coherent integration, Doppler processing, synthetic aperture imaging, and so forth.

A set of coherent pulses can generate a coherent processing interval (CPI) in applications as Doppler processing or synthetic aperture radar (SAR) imaging [78, 79, 80]. Many radar systems process data from multiple CPIs and therefore acts on even larger time scales. Techniques on this category comprise multiple-CPI ambiguity resolution [81], multi-look SAR imaging [82], and track filtering [83].

As we know, the characteristics of the processing signals must be intercepted to depict an efficient signal processor. Corresponding characteristics contain frequency, signal power, ways of polarisation, the direction of arrival (DOA), variation over time, and randomness. The phenomenology of received signal relies on intrinsic traits of the physical objects affecting the radar echo, like physical size, coordination and velocity to the radar; besides, radar parameters need to take into consideration as well, such as its transmitted waveform or polarisation or antenna gain.

The radar equation of range estimation introduced previously provides ways to estimate nominal signal power, while the received frequency can be estimated via the Doppler phenomenon. In the course of the signal processing, the complex variation in radar signal generates due to the complexity of the real world, leading to the implementation of random processing to model the signals, and to specific probability density functions.

2.4.2 Signal Conditioning and Interference Suppression

The function of signal conditioning operations is to enhance the signal-to-interference ratio (SIR) of the data before detection, parameters estimation, and imaging, which means to filter the radar data as much as possible. Processing techniques can be implemented to such procedure include beamforming, pulse compression, Doppler processing, and so forth.

Beamforming can be therefore applied if the antenna of radar systems is an array. Fixed beamforming utilises the outcomes of available phase centres to construct a pattern of directive gain. The high-gain main lobe and low side lobes selectively improve the echo strength from scatters in the antenna boresight direction while suppressing the clutter from scatters in other directions. After the integration of all relative channels through appropriate weighting, the main lobe of the beam can be pointed to distinctive boresight directions, and the trade-off among the sidelobe level and the main lobe width modifies by specific applications.

In terms of the concept of adaptive beamforming, it is feasible to recognise the jamming and clutter presented to the antenna pattern side lobes and to design a set of weights to integrate the channels. Meanwhile, more efficient jammer suppression can be therefore achieved, and the performance of clutter suppression can also be enhanced via the technique.

Pulse compression can be analysed as a distinctive scenario of the matched filtering. Numerous designs of radar systems endeavour to achieve both high sensitivity and high range resolution, which means the capability to distinguish close targets spatially. In general, the ability of target detection enhances as the transmitted waveform's instantaneous bandwidth increases. The transmitting pulse is required to extend its length if the radar transmits a constant-frequency rectangular envelop pulse. Nevertheless, prolonging the pulse reduces its instantaneous bandwidth, and jeopardise the range resolution. Therefore, trade-off and compromise will need to make between the sensitivity and range resolution, based on distinctive applications.

Pulse compression gives a practical method to solve this dilemma. With the procedure of decoupling the waveform bandwidth from its duration, it specifies both factors independently. The linear frequency modulated (LFM, or so-called chirp) waveform is one of the most practical alternatives.

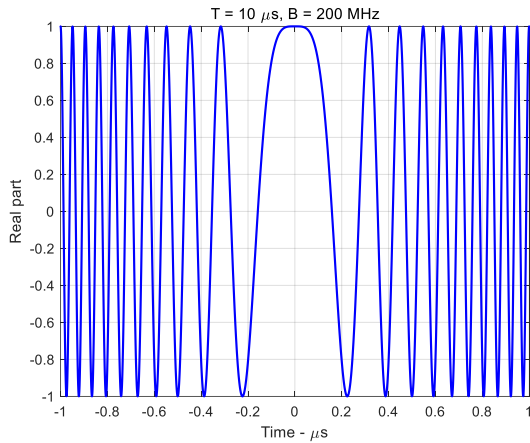


Figure 2.8 Real part of an LFM signal

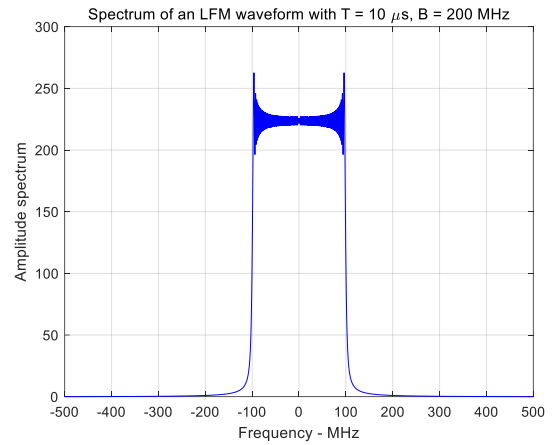


Figure 2.10 Spectrum of an LFM signal

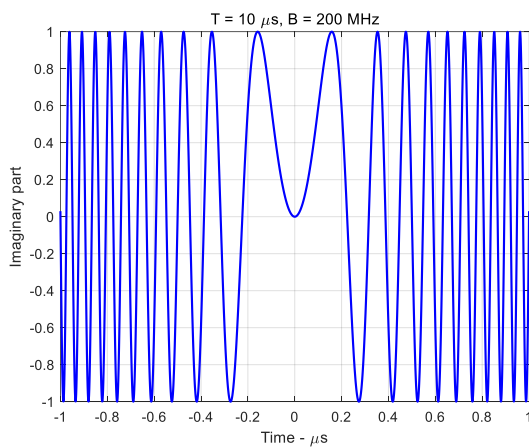


Figure 2.9 Imaginary part of an LFM signal

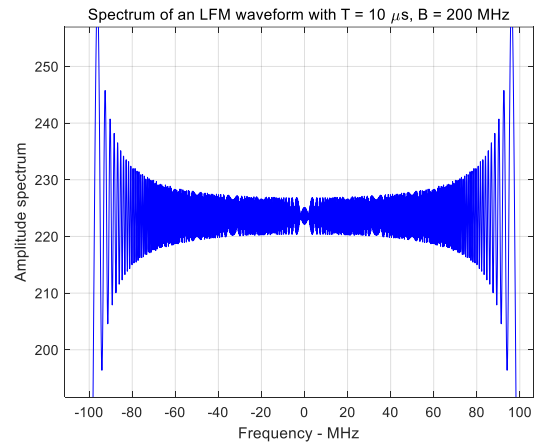


Figure 2.11 Spectrum of an LFM signal (close look)

Figure 2.8 and 2.9 illustrate a sample of an LFM signal; The LFM waveform has a duration of $10\mu s$, a bandwidth of $200MHz$. The real part of the signal is shown in the Figure 2.8 and the imaginary part is shown in the Figure 2.9. Furthermore, the spectrum of the LFM signal is illustrated in the Figure 2.10 and 2.11, which there is a close look in the Figure 2.11 within the fluctuating section of the previous figure.

The matched filter is to maximise the SNR at its result. The impulse response of the filter is a replica of the modulation function of the transmitted waveform. It has been reversed in time and conjugated and therefore, the impulse response is matched to the specific modulation of the transmitted waveform. Pulse compression designs desirable waveforms and corresponding matched filters as well

so that the result of the matched filter responds to the high transmitted energy of a long pulse. Such width provides the ability of the waveform to distinguish objects in range since it is therefore called the range resolution.

The concepts of Doppler processing and clutter filtering are highly associated. They both concentrate on upgrading the detectability of moving targets under suppressing interference clutters, based on distinctions in Doppler shift of the received signals from the clutters and the objects. Two techniques distinguish each other from the domain of implementation (time or frequency domain). Clutter filtering is generally applied to moving target indication (MTI), which simply pulse-to-pulse high-pass filters the received signal at the given range to suppress constant components (referring to the non-moving clutters). Simple and low-order digital filters are implemented to the sampling signals.

In terms of the Doppler processing, it refers to the implementations of the fast Fourier transform (FFT) or a few spectral estimation techniques. Doppler processing is designed to explicitly compute the spectrum of the received signals across multiple pulses. Because of different Doppler shifts of discrete objects, energy from moving objects locates to distinctive zone of the spectrum from the clutter energy, and it permits the feasibility of detection and recognition of the targets out of the clutter. Doppler processing attains various information from the radar signals. While the cost requires more radar pulses, leading to the increased consumption of power and timeline, and higher processing complexity as well.

2.4.3 Detecting, Imaging, and Postprocessing

Radars are also implemented to generate high-resolution images. Comparing of optical and SAR images, explicit comparison discloses numerous similarities and crucial distinctions as well between the scene generated by radars and visible wavelengths equipment. The photograph took by visible light are a more natural way to interpret and analyse, since the phenomenology is similar to the human visual system. Though parts of radars cannot achieve the resolution of photographic systems, there are still a few distinct advantages. Radar systems can implement imaging through clouds and inclement weather. On the other hand, radar can operate all day, while photography and other optical sensors would fail on environmental conditions. However, radar imaging at typical ranges and wavelengths would not be affected in any noticeable way.

To obtain high-resolution imagery, radar systems apply an integration of high-bandwidth waveforms to receive a desirable resolution in the range domain and apply the synthetic aperture radar (SAR) technique to get decent resolution in the cross-range domain. The high performance of range

resolution is attained through pulse compression, which maintains adequate signal energy, i.e., linear frequency modulation. A long pulse swept over a large enough bandwidth B can present decent range resolution via a matched filter. According to varied applications, modern imaging radars typically have good range resolution.

For a traditional non-imaging radar (real aperture in terms of SAR), cross-range resolution depends on the width of the antenna beam at the range of interest. Realistic antenna beam-widths for narrow-beam antennas are worse than typical range resolutions and too coarse to generate realistic images. Such intrinsic drawback of cross-range resolution can be figured out by SAR techniques.

In terms of synthetic aperture technique, it indicates that synthesising the effect of a huge antenna by mobilising the actual physical radar antenna in the corresponding imaging zone. Signals are transmitted at each pre-set location, and results are collected to process altogether in a specific order. A SAR system generates the effect of a large antenna extending over the distance flown while collecting data. The substantially large size of antenna aperture presents a narrow-focused antenna beam with high efficiency, leading to the feasibility of high performance of cross-range resolution.

Furthermore, the capability of recognition of multi targets is another fundamental function to a radar signal processor. Estimation information regarding the presence of targets includes in the echoes of the radar pulses, which are made up of a superposition of receiver noise, undesired clutter, and possible jamming. The signal processor is required to analyse the received signal and distinguish the useful information from others.

The complexity of radar signals calls to construct corresponding statistical models, and the estimation of targets among interference signals is a typical case in statistical signal processing theory. Optimal estimation can be attained by the threshold detection in numerous scenarios. The magnitude of the transmitted signal makes comparisons to a pre-set threshold after necessary processing in this approach. If the signal magnitude is below the threshold, judgment lies on the interference signals only; while it is above the threshold, a detection is declared since it contains the target echo with interference. Essentially, the detector makes judgment if the energy in specific signal samples is too large to likely being only interference.

As the outcome of a process of statistical estimation, the judgments of threshold detection have a finite probability of being wrong. Such errors (false alarm) are minimised if noise spikes present distinctively among the background interference if the SIR is as large as possible. Under such circumstances, the threshold can be set correspondingly high, so that few false alarms will be triggered while the majority of objects can still be detected. The matched filter maximises the SIR and presents

the optimal performance of threshold estimation. Moreover, the achievable SIR is proportionally expanding to the transmitted pulse energy, which stimulates to apply longer pulses for higher energy on the objects.

The methodology of threshold estimation can be implemented to distinctive signal processing sections. For instance, in an application of a fast-time signal trace, it can be presented to a signal with detections at different Doppler frequencies. Numerous detectors designed for threshold estimation operate on the distinctive principles of the complex signal samples. The threshold is determined by the foreknowledge of the interference statistics, to restrict the possibility of false alarms to an acceptable percentage. Nevertheless, in practical applications, the statistical parameters of interference are rarely precisely known, leading to precomputing a reasonable threshold. The threshold is generally estimated by applying interference statistics from the data itself, which is the so-called constant-false-alarm-rate (CFAR) detection.

Last but not least, radar systems implement numerous post-processing techniques after the procedure of detection. Often these are referred to as data processing rather than signal processing operations. Tracking is an essential component of many systems. Once detected, the signal processor may also estimate the range of the object, which relies on the time delay after pulse transmission where the threshold crossing comes, the angle of the object corresponding to the antenna boresight direction, and its radial velocity using Doppler detections. The angle measurements are obtained using angle tracking techniques, especially mono-pulse tracking. These signal processor measurements provide a trackable position of the target location at one instant in time. Track filtering presents a comprehensive process of integrating various measurements to calculate an exhaustive motion trajectory of the object over time. The individual position detections will occur errors because of interference, and there may also be multiple objects with crossing or closely spaced trajectories. Consequently, track filtering is required to tackle the situation of decision-making regarding detections corresponding to which objects being traced and correctly calculate nearby and crossing trajectories. Different techniques and algorithms for optimal estimation have been researched to implement track filtering effectively.

2.5 Estimation Theory of Statistical Signal Processing

Several estimation theories and theorem based on statistical signal processing is going to be introduced in this section.

2.5.1 Probability Density Function

The signal model with random noise can be expressed as

$$y(x) = a_k x^k + a_{k-1} x^{k-1} + \dots + a_2 x^2 + a_1 x + a_0 + n[x] \quad (2.25)$$

where $x = 0, 1, \dots, K - 1$.

A reasonable model for the noise is that $n[x]$ is white Gaussian noise (WGN) or each of $n[x]$ has the PDF $X(0, \sigma^2)$ (Gaussian distribution with a mean of zero and a variance of σ^2) and every single sample is independent to others. The parameters to be estimated are a_2 , a_1 , and a_0 . They can be integrated into a vector form as $\varepsilon = [a_2 \ a_1 \ a_0]^T$. Letting $y = [y(0) \ y(1) \ \dots \ y(K - 1)]^T$, the PDF is

$$p(y; \varepsilon) = \frac{1}{(2\pi\sigma^2)^{\frac{K}{2}}} \exp \left[-\frac{1}{2\sigma^2} \sum_{x=0}^{K-1} (y(x) - a_k x^k - a_{k-1} x^{k-1} - \dots - a_2 x^2 - a_1 x - a_0) \right] \quad (2.26)$$

The assumption of WGN is justified by the need to formulate a mathematically tractable; therefore, closed-form estimators can be found. Meanwhile, it is reasonable unless there is strong evidence to the contrary, such as highly correlated noise. Theoretically, the performance of any estimator attained will be critically dependent on the PDFs.

Estimation based on PDFs can be described as classical estimation because the parameters to be determined are presumed to be deterministic but unknown. In contrast, Bayesian estimation incorporates the prior knowledge of the parameters of interest. It is considered as a realization of the random variable ε . The signal can be therefore presented through the joint PDF

$$p(y; \varepsilon) = p(y|\varepsilon)p(\varepsilon) \quad (2.27)$$

where $p(\varepsilon)$ is the prior PDF, briefing the knowledge related to ε before any signal is acquired, and $p(y|\varepsilon)$ is a conditional PDF, concluding the knowledge provided with the signal y conditioned on knowing ε .

Once the PDF is specified, the question becomes one of determining an optimal function or estimator of the signal. Note that an estimator may depend on other parameters, but only if they are known. An estimator may be considered as a mapping that distributes value to ε for each realisation of y . The estimation of ε is the value of ε attained by a given realisation of y . This distinction is analogous to a random variable, which is a function defined on the sample space.

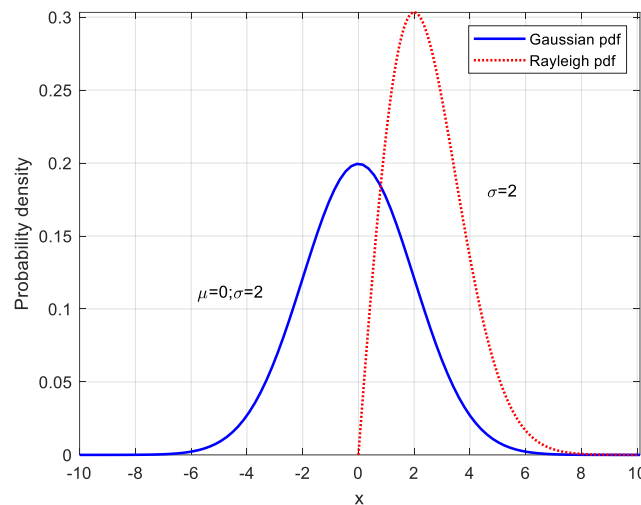


Figure 2.12 Probability Density Function (PDF) of Gaussian and Rayleigh models

A specific estimator is closer to the true value only means that for the given realisation of the signal. To assess performance, we must do so statistically. One possibility would be to repeat the experiment that generated the signal and apply each estimate to every signals set. Then we could get the information which estimator produces a better estimate in a majority of the cases.

The application of computer simulations for assessing estimation performance is never conclusive. Under promising circumstance may the practical performance be attained to the desired extent of precision. In contrast, under limited circumstance may erroneous results be obtained as errors in the simulation techniques or an insufficient number of experiments.

Furthermore, there is always the trade-off among computational complexity and performance. In a general scenario, an estimator performing better also requires more computation. It is known that optimal estimators can sometimes be challenging to implement, which requires a multi-dimensional optimisation and integration. Under such circumstances, alternative estimators with suboptimal characteristic but computational feasibility may be preferred. For any specific application, we need to weigh up between the loss in performance of a suboptimal estimator and computational complexity. Generally, estimations aim to obtain an optimal estimator, and we resort to an approximately optimal estimator; if the former cannot be found or is not implementable, suboptimal one is, therefore, the new destination.

2.5.2 Minimum Variance Unbiased Estimation

It is natural to investigate the one with the minimum variance among various estimators. The unbiased constraint is shown by example to be desirable from a practical viewpoint since the more fundamental error criterion; the minimum mean square error generally leads to unrealisable estimators, Minimum variance unbiased estimators do not exist in general, exist. When they do, varied approaches can be applied to ascertain them; these approaches are determined by the Cramer-Rao lower bound. If a minimum variance unbiased estimator does not exist or if both previous two methods do not work, a further restriction on the estimator, to being linear in the signal, leads to an easily implemented, but suboptimal, estimator.

In terms of an unbiased estimator, it means that averagely the estimator will yield the true value of the unknown parameter. While the parameter value may, in general, be anywhere in the interval $a < \varepsilon < b$, unbiasedness demonstrates that whatever the true value of ε , the estimator will yield it on the average. An unbiased estimator can be presented in mathematically as

$$E(\hat{\varepsilon}) = \varepsilon \quad a < \varepsilon < b \quad (2.28)$$

Generally, an unbiased estimator has a symmetric PDF centred about the true value of ε , although this is not necessary. The restriction that $E(\hat{\varepsilon}) = \varepsilon$ for all ε is an important one. Assuming $\hat{\varepsilon} = h(x)$, where $x = [x(0) x(1) \dots x(K-1)]^T$,

$$E(\hat{\varepsilon}) = \int h(x) p(x; \varepsilon) dx = \varepsilon \quad \text{for all } \varepsilon \quad (2.29)$$

That an estimator is unbiased does not necessarily refer that it is a good estimator. It merely assures that on the average, it will attain the true value. On the other hand, biased estimators are ones that are characterised by a systematic error. A persistent bias will always lead to an unsatisfied estimator. For example, the unbiased property has a significant implication when several estimators are combined. It sometimes occurs that several estimates of the same parameter are available, i.e., $\{\hat{\varepsilon}_1, \hat{\varepsilon}_2, \dots, \hat{\varepsilon}_n\}$. A feasible solution is to combine these estimates into a better one by averaging them to form

$$\hat{\varepsilon} = \frac{1}{m} \sum_{n=1}^m \hat{\varepsilon}_n \quad (2.30)$$

Letting these estimators are unbiased, with the same variance, and uncorrelated with others

$$E(\hat{\varepsilon}) = \varepsilon \quad (2.31)$$

and

$$\text{var}(\hat{\varepsilon}) = \frac{1}{m^2} \sum_{n=1}^m \text{var}(\hat{\varepsilon}_n) = \frac{\text{var}(\hat{\varepsilon}_1)}{m} \quad (2.32)$$

so that as more estimates are averaged, the variance will decrease. Ultimately, as $m \rightarrow \infty$, $\hat{\varepsilon} \rightarrow \varepsilon$.

However, if the estimators are biased or $E(\hat{\varepsilon}_n) = \varepsilon + b(\varepsilon)$, then

$$E(\hat{\varepsilon}) = \frac{1}{m} \sum_{n=1}^m E(\hat{\varepsilon}_n) = \varepsilon + b(\varepsilon) \quad (2.33)$$

and no matter how many estimators are averaged, $\hat{\varepsilon}$ will not converge to the true value.

$$b(\varepsilon) = E(\hat{\varepsilon}_n) - \varepsilon \quad (2.34)$$

is defined as the bias if the estimator.

Minimum variance criterion

It is needed to adopt several optimality criteria in the course of ascertaining optimal estimators. A typical formula is the mean square error (MSE), and it can be presented as

$$\text{mse}(\hat{\varepsilon}) = E[(\hat{\varepsilon} - \varepsilon)^2] \quad (2.35)$$

The deviation of the estimator from the true value is determined by the average mean square. However, the application of this formula leads to unrealisable estimators, which cannot be individually presented as a function of the signal date. The MSE can be rewritten as

$$\begin{aligned} \text{mse}(\hat{\varepsilon}) &= E\left\{[(\hat{\varepsilon} - E(\hat{\varepsilon})) + (E(\hat{\varepsilon}) - \varepsilon)]^2\right\} \\ &= \text{var}(\hat{\varepsilon}) + [E(\hat{\varepsilon}) - \varepsilon]^2 = \text{var}(\hat{\varepsilon}) + b^2(\varepsilon) \end{aligned} \quad (2.36)$$

which indicates that the MSE consists of error due to the variance of the estimator and the bias. The estimator is, therefore, not realisable in that the optimal value relies on the unknown parameter. In retrospect, the estimator depends on the unknown parameter since the bias term is a function of it, which means any criterion based on the bias indicates an unrealisable estimator.

An alternative approach is to restrict the bias down to zero and search for the estimator with minimal variance. Such an estimator is named as the minimum variance unbiased (MVU) estimator, while the MSE of an unbiased estimator is the variance. In general, the MVU estimator does not always exist. Even if an MVU estimator exists, it may not be able to find it. There are several possible approaches to get asymptotic solutions.

(1). Ascertaining the Cramer-Rao lower bound (CRLB) and examine whether several estimators satisfy its formula;

- (2). Implementing the Rao-Blackwell-Lehmann-Scheffe (RBLs) theorem;
- (3). Further restrict the class of estimator within the specific restricted area.

Approaches one and two may produce the MVU estimator, while three will yield it only if the MVU estimator is linear in the signal data.

The CRLB permits us to ascertain that for any unbiased estimator the variance must be greater than or equal to a given value. If an estimator exists whose variance is equivalent to the CRLB for each value of it, then it must be the MVU estimator. In this case, the theory of the CRLB immediately yields the estimator. Realistically, no estimator exists whose variance is equivalent to the bound, while an MVU estimator may still exist. Therefore, it must resort to the Rao-Blackwell-Lehmann-Scheffe (RBLs) theorem. This procedure first finds sufficient statistic, one which uses all the signal data efficiently, and then finds a mapping of an unbiased estimator to the sufficient statistic. With a slight restriction of the PDF of the data, this procedure will then be assured to produce the MVU estimator. The third approach requires the estimator to be a linear, sometimes severe restriction, and chooses the best linear estimator; only for particular signal data sets can this approach produce the MVU estimator.

2.5.3 Cramer-Rao Lower Bound

As described above, it is beneficial in practical applications to set a lower bound on the variance of any unbiased estimator [84]. Generally, it permits us to evaluate whether an estimator is an MVU estimator or not. Meanwhile, it presents a reference to compare the performance of any unbiased estimator. It also indicates that it is physically impossible to search for an unbiased estimator with the variance less than the bound. Despite the existence of various similar variance bounds, the CRLB is by far the easiest to determine [85]. Besides, the theory permits us to evaluate whether an estimator can hit the bound conveniently. If no such estimator exists, then we understand to search for estimators which are asymptotically close to the bound.

Before starting the CRLB theorem, it is worthwhile to expose the hidden factors that determine how well we can estimate a parameter. As an example, we should not expect to adequately estimate a parameter precisely if the PDF depends only weakly on that parameter, or in the extreme case if the PDF does not depend on it at all. Generally, the more the PDF is influenced by the unknown parameter, the better we should be able to estimate it.

Consider a simple signal sample

$$y[0] = B + \varphi(0) \quad (2.37)$$

where $\varphi(0) \sim \mathcal{N}(0, \sigma^2)$, and it is desired to estimate B , and then we expect a better estimate if σ^2 is small. Indeed, from previous sections, it is known that $\tilde{B} = y[0]$ is a good unbiased estimator. The variance is, of course, just σ^2 , so that the estimator accuracy improves as σ^2 decreases. Meanwhile, the PDFs for two different variances can be expressed as follow

$$p_u(y[0]; B) = \frac{1}{\sqrt{2\pi\sigma_u^2}} \exp\left[-\frac{1}{2\sigma_u^2}(y[0] - B)^2\right] \quad (2.38)$$

Likelihood function refers to the PDF as a function of the unknown fixed parameter. The sharpness of the likelihood function affects the precision of parameters estimation, which can be calculated by the negative of the second derivative of the logarithm of the likelihood function at its peak. Now consider the natural logarithm of the PDF of Equation (2.38)

$$\ln(y[0]; B) = -\ln\sqrt{2\pi\sigma_u^2} - \frac{1}{2\sigma_u^2}(y[0] - B)^2 \quad (2.39)$$

And the first derivation is

$$\frac{\partial \ln(y[0]; B)}{\partial B} = \frac{1}{\sigma_u^2}(y[0] - B) \quad (2.40)$$

Then the negative of the second derivative is

$$-\frac{\partial^2 \ln(y[0]; B)}{\partial B^2} = \frac{1}{\sigma_u^2} \quad (2.41)$$

The curvature increases as σ^2 decreases. Since we already know that the estimator $\tilde{B} = y[0]$ has variance σ^2 , then for this example

$$\text{var}(\tilde{B}) = \frac{1}{-\frac{\partial^2 \ln(y[0]; B)}{\partial B^2}} \quad (2.42)$$

and the variance decreases as the curvature increases. Although in this example, the second derivative does not depend on $y[0]$, while in general it will. Therefore, an appropriate benchmark of curvature is

$$-E\left[\frac{\partial^2 \ln(y[0]; B)}{\partial B^2}\right] \quad (2.43)$$

The expectation is taken concerning $p(y[0]; B)$, resulting in a function of B only. The expectation acknowledges the fact that the likelihood function, which depends on $y[0]$, is itself a random variable. As the theorem of CRLB for the scalar parameter, the PDF $p(y; \varepsilon)$ satisfies

$$E \left[\frac{\partial \ln p(y; \varepsilon)}{\partial \varepsilon} \right] = 0 \quad \text{for all } \varepsilon \quad (2.44)$$

The variance of any unbiased estimator $\hat{\varepsilon}$ must satisfy

$$\text{Var}(\hat{\varepsilon}) \geq \frac{1}{-E \left[\frac{\partial^2 \ln p(y; \varepsilon)}{\partial \varepsilon^2} \right]} \quad (2.45)$$

Moreover, an unbiased estimator may be found that attains the bound for all ε if and only if

$$\frac{\partial \ln p(y; \varepsilon)}{\partial \varepsilon} = L(\varepsilon)(h(y) - \varepsilon) \quad (2.46)$$

That estimator, $\hat{\varepsilon} = h(y)$, is the MVU estimator, and its minimum variance is $1/L(\varepsilon)$.

The expectation in (2.45) is explicitly given by

$$E \left[\frac{\partial^2 \ln p(y; \varepsilon)}{\partial \varepsilon^2} \right] = \int \frac{\partial^2 \ln p(y; \varepsilon)}{\partial \varepsilon^2} p(y; \varepsilon) dy \quad (2.47)$$

If an estimator is unbiased and attains the CRLB, it is efficient. For example, an estimator is efficient as it attains the CRLB; therefore, it is also the MVU estimator. On the other hand, one does not attain the CRLB, which means it is not efficient. However, since its variance is uniformly less than that of all other unbiased estimators, it is still the MVU estimator.

The CRLB given by (2.47) can also be presented in a slightly different form. Although (3.6) is usually more convenient for evaluation, the alternative form is sometimes useful for theoretical work. It follows from the identity

$$E \left[\left(\frac{\partial \ln p(y; \varepsilon)}{\partial \varepsilon} \right)^2 \right] = -E \left[\frac{\partial^2 \ln p(y; \varepsilon)}{\partial \varepsilon^2} \right] \quad (2.48)$$

so that

$$\text{Var}(\hat{\varepsilon}) \geq \frac{1}{E \left[\left(\frac{\partial \ln p(y; \varepsilon)}{\partial \varepsilon} \right)^2 \right]} \quad (2.49)$$

The denominator in (2.45) is referred to as the Fisher information $I(\varepsilon)$ for the data \mathbf{y}

$$I(\varepsilon) = -E \left[\frac{\partial^2 \ln p(\mathbf{y}; \varepsilon)}{\partial \varepsilon^2} \right] \quad (2.50)$$

As shown previously, when the CRLB is regressive, the variance is the reciprocal of the Fisher information. Intuitively, the more information, the lower the bound. It has the essential properties of an information measure because it is non-negative due to (2.49) and additive for independent observations.

The latter property leads to the result that the CRLB for M IID (independent identity distribution) observations is $1/M$ times that for one observation. To verify this, note that for independent observations

$$\ln p(\mathbf{y}; \varepsilon) = \sum_{m=0}^{M-1} \ln p(y[m]; \varepsilon) \quad (2.51)$$

This result in

$$-E \left[\frac{\partial^2 \ln p(\mathbf{y}; \varepsilon)}{\partial \varepsilon^2} \right] = -\sum_{m=0}^{M-1} E \left[\frac{\partial^2 \ln p(y[m]; \varepsilon)}{\partial \varepsilon^2} \right] \quad (2.52)$$

and for identically distributed observations

$$I(\varepsilon) = Mi(\varepsilon) \quad (2.53)$$

where

$$i(\varepsilon) = E \left[\frac{\partial^2 \ln p(y[m]; \varepsilon)}{\partial \varepsilon^2} \right] I(\varepsilon) = Mi(\varepsilon) \quad (2.54)$$

is the Fisher information for one sample. For non-independent samples, we might expect that the information will be less than $Mi(\varepsilon)$. For entirely dependent samples as $y[0] = y[1] = \dots = y[m-1]$, we will have $I(\varepsilon) = i(\varepsilon)$. Therefore, additional observations carry no information, and the CRLB will not decrease with increasing data record length.

This chapter discusses the relevant theory required for current research, consisting of radar theory (mainly focusing on Doppler radar and FMCW radar) and the range estimation theory, which initially a summary regarding range equations and then range resolution, finishing off with descriptions about the maximum unambiguous range and range performance. A preview of basic radar signal processing is presented and then estimation theory of statistical signal processing. Several important concepts are introduced for the following discussion, i.e., PDF, MVU estimator and CRLB.

3. Current Ranging Techniques for High-precision Performance

Miscellaneous elegant techniques and algorithms have been implemented to attain high-performance range estimation, based on distinctive structures of radar systems., and both coherent and non-coherent approaches are presented to this goal. Because of the intrinsic pros of system structure, FMCW radar draws considerable preferences to accomplish the objective of precise ranging.

[86] introduced a new up-sampling theory based on interpolators trained for a set of functions to improve the performance of nonlinearity correction in FMCW radar (2.4 GHz) and to enhance range estimation. However, it did not address the nonlinearity correction problem at the chip or circuit level, only at signal processing level. Fourier coefficients are applied to estimate frequency by interpolation in [87, 88]; [87] is based on the periodogram technique for the computational simplicity, but it is only applicable to Hanning window. One three-point interpolation DFT method for frequency estimation is implemented in [89, 90, 91], in which [89] uses a H-term maximum sidelobe decay window. Weighted multipoint interpolated DFT method for fine estimation is investigated in [92, 93], but they are still only applicable to Hanning window. [94] presented an interpolated DFT algorithm with zero-padding for classic windows. [14] proposed a fine resolution frequency estimation from three DFT samples. A precise ranging technique of FMCW radar based on the phase of the zero-padded FFT is presented in [95]. Another fine ranging algorithm via DFT with millimetre-wave FMCW radar (60 GHz and 122 GHz) is introduced in [96]. A chirp Z transform method for improving ranging performance is introduced in [63, 97]. Other distinctive algorithms of accurate ranging for FMCW radars are presents in [98-102].

[63] introduced a chirp Z transform algorithm for an optimized FMCW application, and it proposed to calculate the phase via the CZT, as the CZT already calculated the complex frequency spectrum. However, its precision is limited due to the real-time requirement by means of FPGA fulfillment. Apart from the intrinsic advantage of chirp Z transform and absorbing the positive thoughts mentioned above, the CZT-based algorithm stated in the thesis utilised the most-likelihood process (estimator) creatively for improving range performance, by introducing and applying the concept and thought of statistical signal processing.

[97] presented a multi-target precise-ranging algorithm based on the CZT as well, for FMCW systems. It described that the performance was better than the FFT and MUSIC in white noise background; but its multi-target algorithm still needs to be optimized in the implementation of the periodogram.

Extending to multi-target ranging methods in the FMCW systems, such techniques can be categorised into two aspects, high-resolution techniques and filter bank techniques. In terms of high resolution techniques, under the general assumption of white noise, these techniques determine the targets frequencies by distinguishing the signal and noise subspaces. The eigen-decomposition of the observation covariance matrix is applied to fulfil such separation. MUSIC, ESPRIT, Min-Norm and Pisarenko are the prevailing algorithms within the category [103-106]. The statistical performance of these algorithms is quite similar. Due to the required eigen-decomposition, they are computationally sophisticated.

On the other hand, filter bank techniques are typically applied if the noise is coloured or lack of sufficient knowledge about relative noise. APES, Slepian filters, Periodogram, and Capon, are the most regular algorithms among them [107-110]. They conduct adaptive or non-adaptive narrowband filters to estimate sinusoids under the background of the noise environment. Despite the computational complexity, the demanded inversion of the covariance matrix in these techniques requires high computational capacity.

3.1 Coherent Ranging Techniques

Radars are implemented to detect objects with the formula of the energy returned to the radar antenna stemming from a transmitted signal that radiates and come back from the target. In the past, most radars were non-coherent in that they transmitted non-coherent bursts of RF energy and the presence and position of a target were determined from an analysis of the amplitude of the signal returning to the radar from the object of interest. In terms of advanced coherent radars, the detection relies not only on the amplitude of the signal but on its phase characteristics as well, allowing for greater precision than that given by the classic range resolution expression. The received vector is detected by relating the phase of the received signal to that of a stable reference oscillator in the radar system. The phase relationship is measured and processed over an extended time relative to the range delay time, often in the tens or sometimes hundreds of milliseconds. Coherent and non-coherent ranging techniques will be both expounded in this chapter.

Figure 3.1 illustrates a typical coherent radar system. The transmitted signal is derived from a set (two or more) of stable oscillators, which serve as the reference for measuring the phase of the received signal. Typically, the received signal is characterised as a vector with an amplitude and a phase. The typical coherent radar measures the received vector in terms of the two orthogonal

components in the rectangular coordinate system, the in-phase (I channel) and the quadrature (Q channel) components of the received vector, rather than the amplitude and phase explicitly.

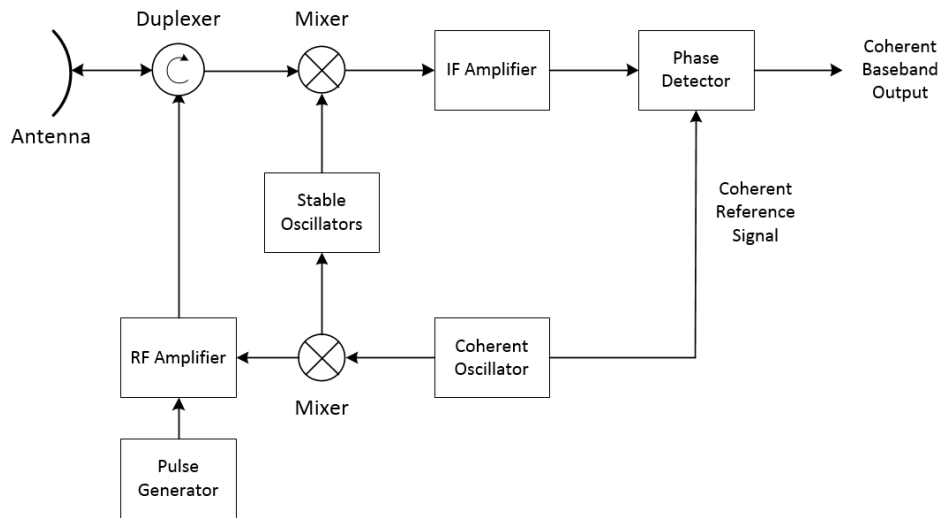


Figure 3.1 A brief diagram of a coherent pulse radar

3.1.1 I/Q Detection

A block diagram of a conventional model of I/Q detection network is presented in Figure 3.2. The received signal is applied to a power splitter, the two outputs of which are applied to the RF ports of double-balanced mixers. The local oscillator (LO) ports are driven by two samples of the coherent oscillator signal, the two components being in quadrature. The resulting outputs from the mixers are the in-phase (I channel) and quadrature-phase (Q channel) baseband signals representative of the received vector.

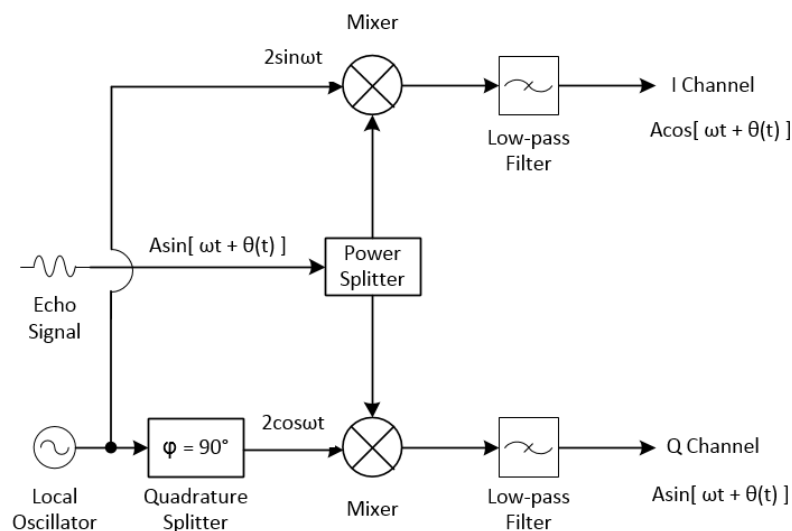


Figure 3.2 A brief diagram of a conventional model of I/Q detection network

Assume the received signal $r(t)$ can be expressed as

$$r(t) = A(t)\sin[\omega t + \theta(t)] \quad (3.1)$$

where $A(t)$ modulates the amplitude of the pulse envelopes.

The received signal flows to distinctive channels. The I channel of the receiver mixes the received signal with the local oscillator (LO). It produces both sum and difference frequency ingredients

$$2\sin(\omega t)A(t)\sin[\omega t + \theta(t)] = A(t)\cos[\theta(t)] - A(t)\cos[2\omega t + \theta(t)] \quad (3.2)$$

The sum component is filtered by the low-pass filter, only the modulation component $A(t)\cos[\theta(t)]$ left.

Another channel (Q channel) mixes the signal with the exact frequency but a 90° phase shift from the I channel oscillator. The mixed consequence of Q channel can be presented as

$$2\cos(\omega t)A(t)\sin[\omega t + \theta(t)] = A(t)\sin[\theta(t)] - A(t)\sin[2\omega t + \theta(t)] \quad (3.3)$$

which, after filtering, leaves the modulation term $A(t)\sin[\theta(t)]$. Both the I and Q channels are required as either one alone cannot provide adequate knowledge to distinguish the phase modulation $\theta(t)$ unambiguously.

As introduced above, the received vector is often detected using a network that measures the component of the received vector that is in phase with the coherent reference oscillator, the I component, and the component that is in quadrature with the coherent reference, the Q component. These two components describe the received vector. The relationships between the I and Q components and the amplitude and phase are given by

$$I = A\cos[\theta(t)] \quad (3.4)$$

$$Q = A\sin[\theta(t)] \quad (3.5)$$

Figure 3.3 is a vector representation of the received signal, showing the relationships between the polar coordinate representations. The amplitude A and phase θ can be determined, if desired, from I and Q

$$A = \sqrt{I^2 + Q^2} \quad (3.6)$$

$$\theta = \arctan\left(\frac{Q}{I}\right) \quad (3.7)$$

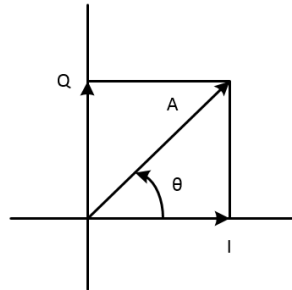


Figure 3.3 Rectangular and polar coordinate system representations of I/Q vector

Some errors can develop from non-ideal circuit components in the I/Q detector that affect the radar system performance. Three common types of errors can be summarised by the following: DC voltage offset of either the I or Q channel or both, imbalance of gain between the I and Q components, and non-orthogonality between the two channels. One method of representing the time history of the received vector is by tracing the locus of the vector tip as it rotates.

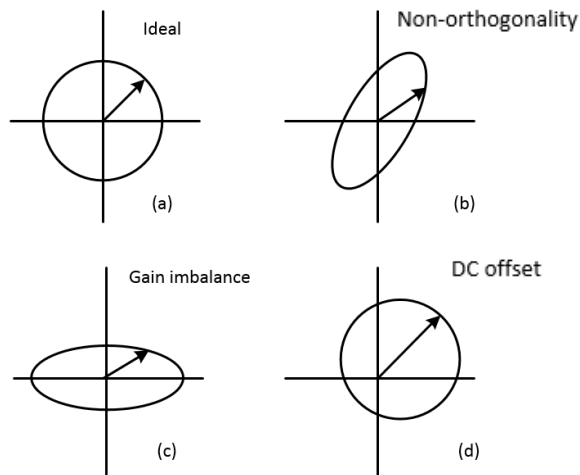


Figure 3.4 Locus plot of ideal target vector and the effects of I/Q errors

For an ideally rotating vector, as depicted in Figure 3.4(a), the result is a circle centred at zero. Contaminants cause a departure from this ideal situation. A displacement of the vector from the origin

results from DC offset, as shown in Figure 3.4(b). The effect of DC offset in either the I or Q channel or both, is to produce a signal in the zero-Doppler bin of the processed signal. If the gains of the two channels are not identical, resulting in an elliptical vector plot, illustrated in Figure 3.4(c), as opposed to the circular plot. The ellipse is either horizontally or vertically oriented, depending on the relative gains of I and Q . And the resulting from non-orthogonality is much the same as for gain imbalance, which the only difference is that the elliptical pattern leading to the non-orthogonality is oriented at 45° from a major axis, as shown in Figure 3.4(d).

Numerous techniques have been developed that minimise or virtually eliminate the effects of these errors. The basic technique is to inject a known ideal signal into the receiver, ahead of the I/Q detector. This signal needs to have a synthesised Doppler signature of known characteristics (i.e., the Doppler amplitude and frequency are known). The signal can be injected at any convenient time when the processor is not on operate, for example, at antenna turnaround or between coherent dwells. Depending on the drift expected of the circuits, the correction may not need to be performed very often.

The synthetic signal is processed through the FFT processor, and the result is analysed. A response in the zero frequency bin of either the I or Q component in the output results from a DC offset in the respective I/Q circuit. A response at the image frequency of the injected signal represents a gain imbalance or non-orthogonality, or both. The relative phase of the image signal provides sufficient information to solve the non-orthogonal ambiguity of the gain.

Correction of errors identified in the detectors may be performed in many approaches. For instrumentation systems in which the received data are generally recorded for offline calibration and processing, the errors may be merely stored in a calibration file. Calibration can be implemented to the signal during the correction process. For operational systems, the data may be corrected to re-establish gain balance (by using a gain correction factor to one or the other channel) and orthogonality (by converting the vector to the spherical coordinate system, applying the phase correction, and reconverting the vector back to the rectangular coordinate system, if needed).

3.1.2 ApRES System and Phase-sensitive Processing

As mentioned above, FMCW radar systems are substantially robust, and their power consumption can be considered low to operate on quite a few harsh environments, and therefore have significant usage from industrial applications to civil employment. There is a purpose-built radar system named pRES system, which detected the depths of the ice shelf on several locations over Antarctica. However,

this system suffers from several flaws, i.e., the high noise parameter of the receiver, the high power consumption of the network analyser, being unable to operate under low temperature, and so forth. Given this enormous potential of the pRES system, an advanced system called ApRES is developed and optimised explicitly for this application [1, 2, 4]. This phase-sensitive FMCW radar system consists of a linear-FM chirp generator via direct digital synthesiser (DDS) and a low-noise receiver/down-converter chain. Accurate phase estimation can be implemented to deramped signal in subsequent processing for high range precision after the baseband synchronisation. The principal parameters of ApRES system are shown in Table 3.1.

Table 3.1 Principal Radar Parameters of ApRES System

Operating (Central) frequency f_c	300 MHz
FM sweep bandwidth B	200 MHz
RF power P_t	20 dBm
Antenna gain G_t, G_r	10 dBi
Noise figure N	6 dB (F=4)
Associated standard range resolution ΔR	43 cm with $\epsilon_r = 3.1$
Depth precision in phase-sensitive mode	3 mm RMS, provided SNR > 21 dB
Pulse duration	1 S
Total acquisition time	60 s for c; ten pulses each with 4 RF gain values
ADC Sampling rate	> 12 k samples/s
Ice attenuation	0.015 dB/m
Maximum operation range, R	2 km

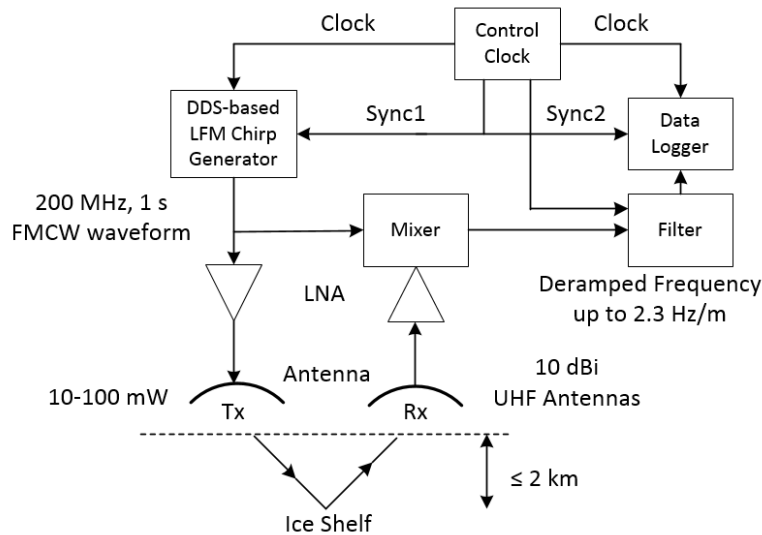


Figure 3.5 Block diagram of basic ApRES system instruction

The ApRES system operates on a 200-400 MHz chirp signal with a 1 GHz clock. Several careful designs regarding filters and amplifiers are incorporated to fulfil the reduced noise figure and low-power consumption requirement. Besides those hardware considerations, some delicate processing techniques can be applied to attain a dependable and precise performance of range estimation. FMCW signal processing is used to detect the targets and measure their coarse ranges. Then phase-sensitive signal processing is applied to determine their exact ranges from the central unit. The crucial steps of phase-sensitive FMCW range processing are illustrated below in Figure 3.6.

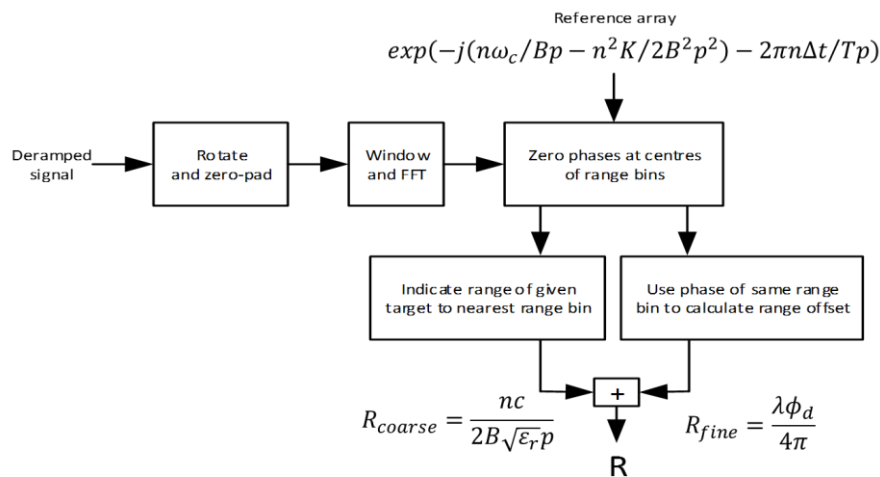


Figure 3.6 Outline of an FMCW ranging technique with phase-sensitive processing (taken from [4])

As the figure is shown, a Vernier-like process is applied to attain high precision of range estimation. The accurate range is achieved through determining the signal phase in the specific range bin where the coarse measurement is located. Signal processing techniques are implemented to integrate standard FFT-based algorithm, providing a rough range estimate to the closest range bin, $n\Delta R$, with a delicate estimation determined by the phase information. Precise phase estimation is needed to determine the exact range bin close where a distinct target is located, and then calculate the fractional range within that specific range bin. The fine range is obtained from the phase of the range bin with maximum magnitude [30].

Detection Performance

Whereas the performance of a non-coherent radar system associated with the detection of a target is bounded to the presence of the thermal noise, the performance of a coherent system is limited by additional factors. The integrity with which the received vector can be described depends on the amplitude and the phase contamination in the system.

As mentioned above, deramped signal processed by the FFT, and after the coarse range of the object, the object's phase of that exactly range bin is estimated as well. Therefore, the millimetre range precision is attained by integrating both rough and the fine estimate. It is to say that peak amplitude is located around the range bin of the desirable objective, then the fine range within the range bin is determined by the phase of that range bin. It indicates that the critical point to achieve an accurate range is to estimate the phase precisely, which means that the frequency-modulated waveform and ADC are required to be exactly synchronised. The synchronisation is attained by producing the frequency-modulated signal with a frequency division of the ADC signal. One significant procedure is the mis-synchronisation calibration of the frequency-modulated signal and ADC signal. A time delay will occur and lead to the corresponding phase delay.

Meanwhile, the Direct Digital Synthesiser may not initiate at the identical time during the operation shift of radar because of temperature variation. A timing error will occur since it cannot be compromised by the calibration of the time delay. One feasible solution is to implement two reference range values as calibration.

3.2 Non-coherent Ranging Techniques

In addition to the factors outlined above, a particularly challenging issue on coherent systems is phase wrapping. Measured or calculated phase values from two or more mutually-coherent

multidimensional signals are related in a nonlinear manner to a desired physical quantity of interest. The nonlinearity is in the form of ‘wraps’ or cycle discontinuities where an underlying two-dimensional phase is wrapped from $-\pi$ to π . The wrapped phase must somehow be unwrapped to provide an estimation of the underlying physical quantity.

Both temporal, spatial signal magnitudes and phase are needed to transmit and receive the coherent signals. By contrast, the non-coherent process applies only signal magnitudes (amplitudes) or intensities (squared magnitudes). Meanwhile, incorrect magnitude spectral components easily add an overall noise-like perturbation to the signal reconstruction. It is simply assumed that slight perturbation of the correct phase values could entirely deteriorate the result of the processed signal. Any coherent processing requires extreme care to maintain correct phase information, which could be very tricky under considerable circumstances [31].

3.2.1 Non-coherent MTI system

Taking a scenario of moving target identification (MTI) as an example, the received signals consist of both object’s information and clutter (including phase and amplitude components). The moving target identification of coherent radar and the pulse-Doppler radar both utilise the phase variation from the received signal to reconstruct the Doppler components.

The fact that the Doppler component, produced by a moving target, can also be recognised by using the amplitude fluctuation. As illustrated in Fig. 3.7, the non-coherent MTI radar uses amplitude replacing phase fluctuations. Nor the coherent internal reference or a phase detector is required as it to coherent systems.

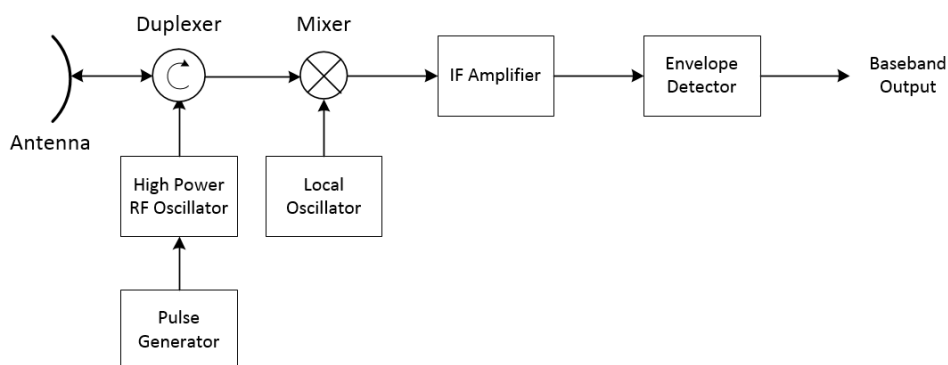


Figure 3.7 Brief illustration of a pulsed non-coherent radar system

As mentioned above, coherent structures offer higher precision but more vulnerable to noise/clutter and phase wrapping; non-coherent structures are more straightforward, more robust, but offering lower precision. For example, if there are limitations about weight and space of radar systems, the simplicity of non-coherent MTI may be attractive to such applications. However, the primary drawback lies on the issue that the object must be present to substantial clutter. Clutter may not typically exist to the desired detection [32]. The identical function is served for clutter and the reference signal in the coherent MTI system. The desired targets might not be detectable if clutter were not present. It is reasonable to design a switch between the non-coherent MTI mode and normal mode, which depends on the clutter. If the radar system is static, the clutter can be saved in a digital memory as a form of look-up tables and applied to make judgments the timer of the mode switch.

In general, the improvement factors of a non-coherent MTI system will not be desirable compared to a coherent structure using the reference oscillator. Clutter is the reference signal in the non-coherent condition. And it is not as reliable as a reference oscillator due to the finite width of the spectrum.

3.2.2 Detection Performance

As discussed in Chapter 2, the essential parameters using discussing the detection performance of a radar system are the probability of detection (P_d) and the probability of false alarm (P_f). These terms best describe the measure of performance for which most (but not all) radar systems are developed; that is, to detect objectives within interference (i.e., noise). There is no closed-form analysis to determine the P_d and P_f directly from knowledge of the radar parameters, but it is relatively straightforward to calculate the signal-to-interference ratio (SIR).

Determining the signal-to-interference ratio will lead to the ability to determine the P_d and P_f performance. This typically involves two steps: determining the received power from the object and determining the interference power. The power that enters a receiver because of the energy reflected from a target can be predicted from

$$P_r = \frac{P_t G^2 \lambda^2 \sigma}{(4\pi)^3 L_s R^4} \quad (3.8)$$

where P_r and P_t are the received power and peak transmitted power respectively, G is the antenna gain, λ is the radar wavelength in metres, σ is the radar cross-section (RCS) of the target, L_s is the system losses.

If the interfering signal is thermal noise, the noise power can be found from

$$P_n = kTBF \quad (3.9)$$

where P_n is the noise power in watts, k is the Boltzmann's constant ($1.38 \times 10^{-23} \text{W/sK}$), T is the system temperature (usually 290K), B is the noise bandwidth in Hertz, and F is the system noise factor.

A detector's performance can be measured by its ability to achieve a certain probability of detection (P_d) and probability of false alarm (P_{fa}) for a given SNR. Examining a detector's ROC curves provides insight into its performance. ROC curves originated from WWII (specifically refer to the Battle of Britain) to help radar operators decide whether the signal they were getting indicated the presence of a meaningful signal (e.g., a Luftwaffe's Messerschmitt aircraft) embedded in noise, or just noise alone (e.g., birds). ROC curves are plots of the probability of detection (P_d) versus the probability of false alarm (P_{fa}) for a given SNR. It is usually used to evaluate the performance of a radar detector.

Given an SNR value, we are able to calculate the probability of detection (P_d) and false alarm (P_{fa}) values that a linear or square-law detector can realise utilising a single pulse. Assuming the determined SNR value is 8 dB, and the required P_{fa} is at most 1%, we can calculate the P_d and P_{fa} and then achieve values of P_d corresponding to $P_{fa} = 0.01$. (It assumes the detector operates in an additive complex whit Gaussian noise environment.)

It is convenient to specify a vector of SNR values and conduct specific function to calculate the ROC curve for each of these SNR values. Instead of individually calculating P_d and P_{fa} values for a given SNR, we can analyse the results in a plot of ROC curves, shown in Figure 3.8. There are distinctive ROC curves for different SNR values. Taking the curve of $SNR = 8$ for an example, P_{fa} is approximately 0.01 at the point where $P_d = 0.9$.

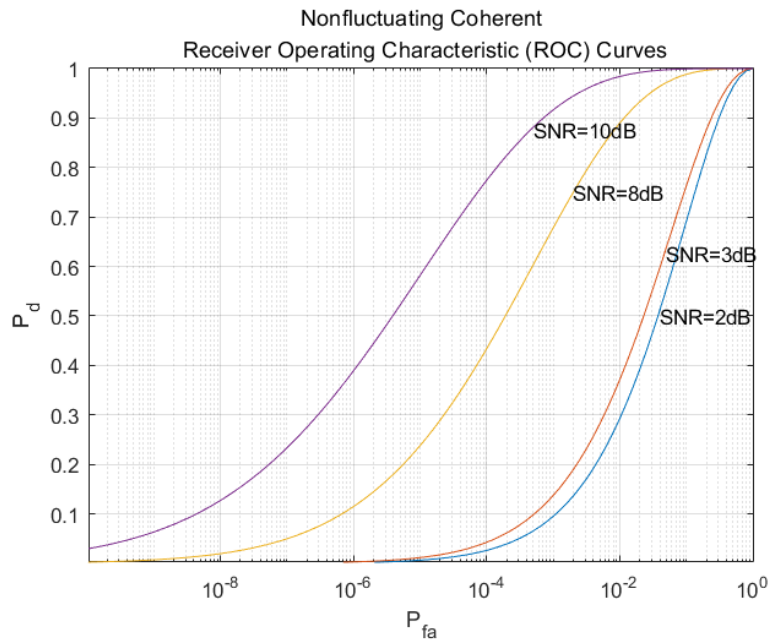


Figure 3.8 Nonfluctuating Coherent ROC Curves for different SNR values

One solution to enhance a detector's performance is to average over several pulses, which is especially useful in scenarios where the signal of interest is known and transmits in additive complex white noise. Although this still applies to both linear and square-law detectors, the consequence of square-law detectors could be off by approximately 0.2 dB. Now continue the previous example of $SNR = 8dB$ and averaging over two pulses, shown in Figure 3.9.

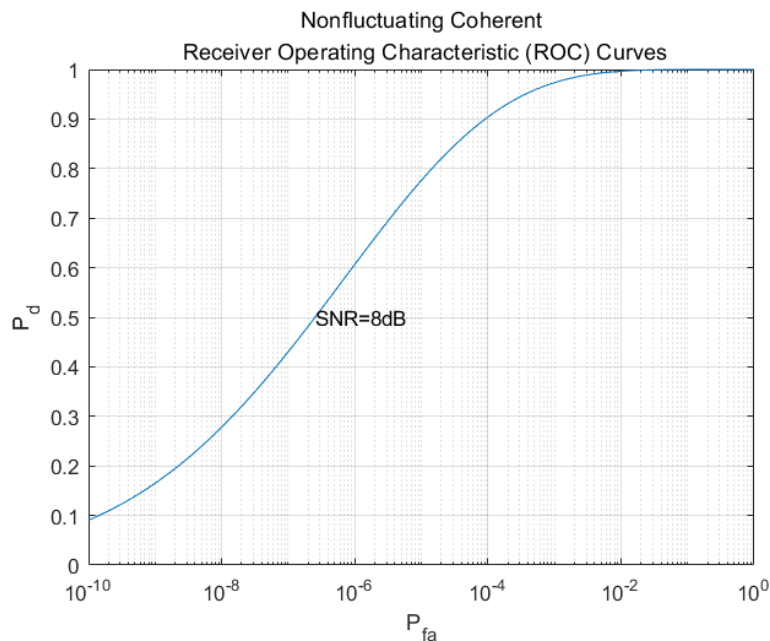


Figure 3.9 Nonfluctuating Coherent ROC Curves (averaging over two pulses)

By observing the illustration, it can be concluded that averaging over two pulses contributed to a higher probability of detection for a given false alarm value. With an SNR of 8 dB and averaging over two pulses, the probability of false alarm can be constrained at most 0.0001 and reached a probability of detection of 0.9. Comparing with the scenario of single pulse, the permitted probability of false alarm is as much as 0.01 to achieve the same probability of detection.

The previous assumption lies on the scenarios of a known signal in complex white Gaussian noise and a default coherent detector. In order to analyse the performance of a non-coherent detector on the scenario where the signal is known apart from the phase, the same SNR values are used to make comparisons, shown in Figure 3.10.

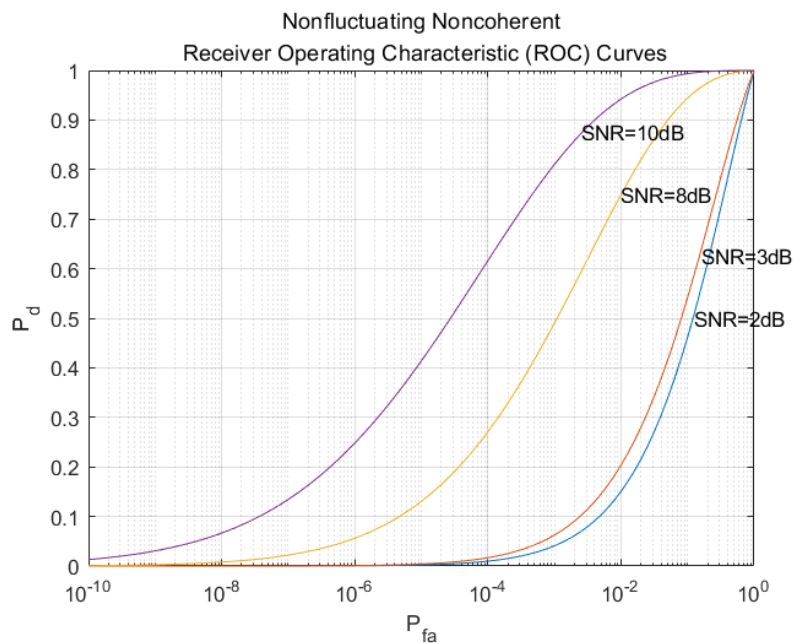


Figure 3.10 Nonfluctuating Noncoherent ROC Curves for different SNR values

By observing the graph of ROC curve corresponding to an SNR of 8dB, we have to tolerate a probability of false alarm up to 0.05, to reach a probability of detection of 0.9. a higher SNR is needed to achieve the same probability of detection for a given probability of false alarm, without using phase information. The Albersheim's equation [128] is applied the related parameters for non-coherent linear detectors.

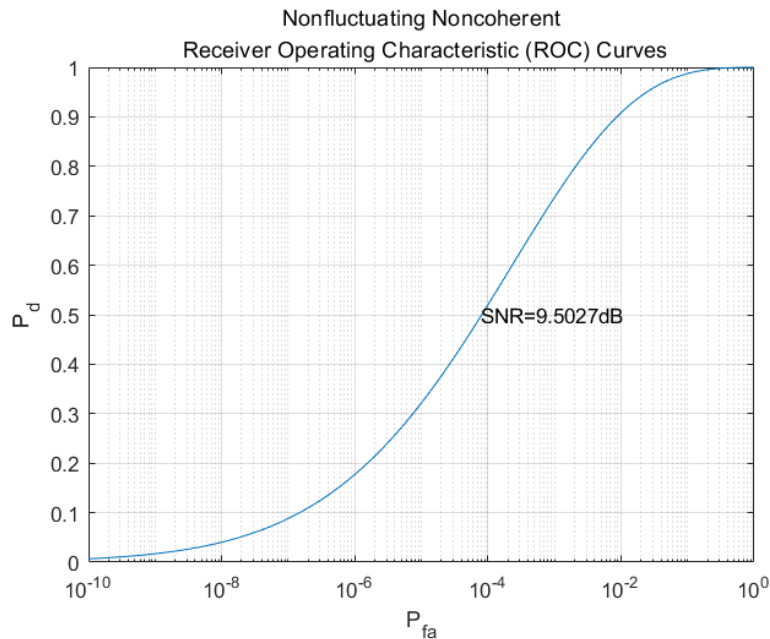


Figure 3.11 Nonfluctuating Noncoherent ROC Curves

It is shown in Figure 3.11 that the detector will reach $P_d = 0.9$ and $P_{fa} = 0.1$, when illustrating the ROC curve of the SNR value approximated by Albersheim's equation. (Note that the Albersheim's equation applies only to non-coherent detectors.)

All previous discussions lie on the assumption that the target is non-fluctuating, which refers to the stable (not change over time) statistical characteristics of the target. While targets' acceleration will change in realistic cases, leading to the variation over time of the target's RCS. A set of statistical models termed Swerling models [129-131].

There are four Swerling models, namely Swerling 1-4, meanwhile, many radar analysts refer to a fifth Swerling model which is termed Swerling 0 or Swerling 5. Each model describes how a target's RCS varies over time and the probability distribution of the variation. The fifth Swerling model is defined as a target that has a constant RCS. The non-fluctuating target often belongs to this category.

The ROC curves for fluctuating targets are distinctive to the non-fluctuating ones, because of the variation of the target RCS. Besides, it is difficult to utilise a coherent detector for Swerling targets in that they add random phase into the received signal; that is to say, non-coherent detection techniques are usually utilised for Swerling targets.

Now consider the ROC curves for a non-fluctuating target and a Swerling 1 target. It is desired to explore the SNR requirements for both situations for getting the same P_d and P_{fa} . Under such

circumstances, the ROC curve as P_d against SNR with varying P_{fa} will be illustrated. The ROC curve for a non-fluctuating target is shown in Figure 3.12, with 20 integrated pulses of non-coherent detection and the desired P_{fa} being at most $1e-6$; meanwhile, the ROC curve for a Swerling 1 target for comparison is illustrated in Figure 3.13.

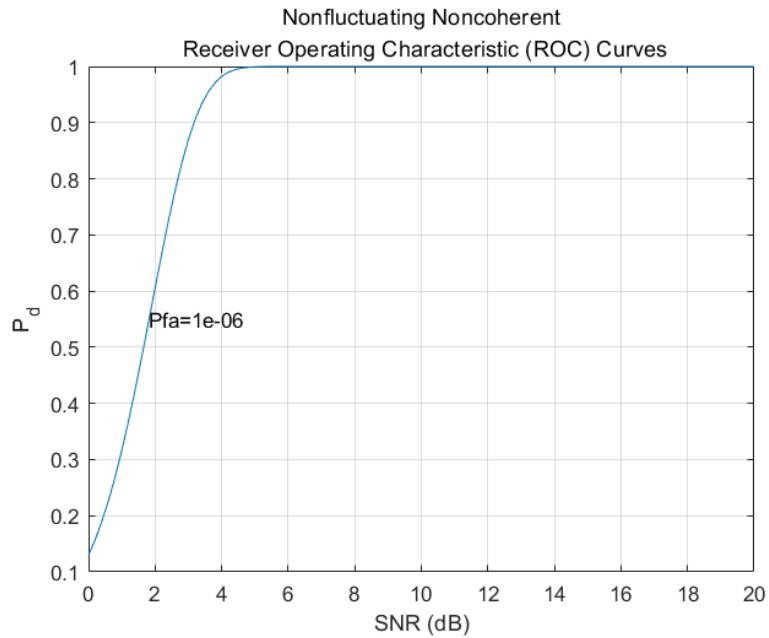


Figure 3.12 Nonfluctuating Noncoherent ROC Curves (with 20 integrated pulses)

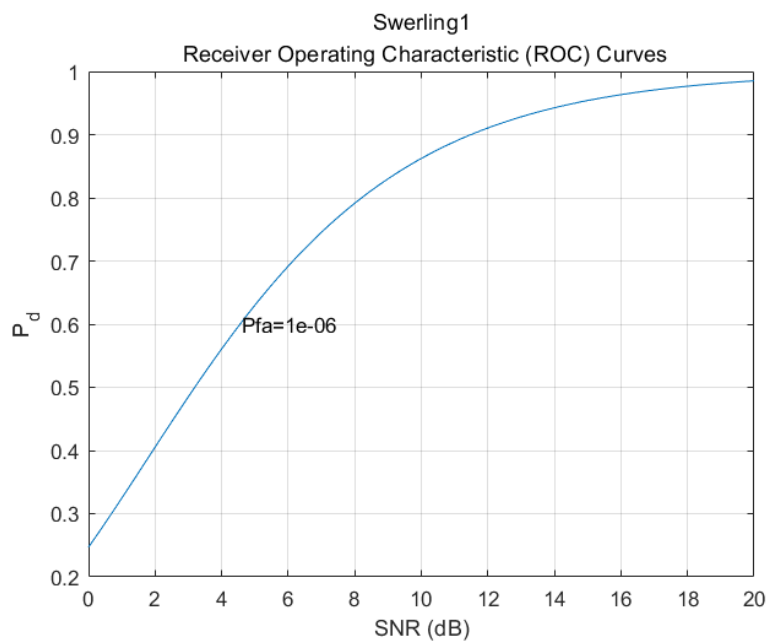


Figure 3.13 ROC Curve of Swerling 1 Target Model

By observing these two figures, it can be known that for a P_d of 0.9, an SNR of about 3.2 dB is required if the target is non-fluctuating. However, the required SNR reaches to about 11.4 dB if the target is a Swerling case 1 model. An 8.2 dB difference will significantly affect the design of the radar system.

3.3 Mathematical Descriptions of Several Useful Transform Tools

There are various mathematical transformations applied to the realm of signal processing and system control, for the convenience and efficiency of post-processing of data chain. Three of the mainly used mathematical tools is going to be introduced as follow, which will be applied to the rest of the thesis, namely, Fourier transform, Z transform, and Laplace transform.

3.3.1 Fourier Transform

The Fourier transform is widely used in many disciplines and is extremely useful to signal processing in the perspective of time and frequency domain. For a signal $f(t)$ continuous on the time interval $[0, T]$ and repeats with period T , its Fourier series is presented as

$$f(t) = A_0 + \sum_{n=1}^{\infty} A_n \cos(n\omega_0 t) + B_n \sin(n\omega_0 t) \quad (3.10)$$

where

$$\omega_0 = 2\pi/T \quad (3.11)$$

$$A_0 = \frac{1}{T} \int_0^T f(t) dt \quad (3.12)$$

$$A_n = \frac{2}{T} \int_0^T f(t) \cos(n\omega_0 t) dt \quad (3.13)$$

$$B_n = \frac{2}{T} \int_0^T f(t) \sin(n\omega_0 t) dt \quad (3.14)$$

This implies that a signal $f(t)$ in time-domain can be identically presented to a constant plus a series of sinusoids and cosines in frequency-domain, and it leads to an effective technique to decompose and analyse signals of interest. An exponential form of the Fourier series can be expressed as

$$f(t) = \sum_{n=-\infty}^{\infty} C_n e^{jn\omega_0 t} \quad (3.15)$$

where

$$C_n = \frac{1}{T} \int_0^T f(t) e^{-jn\omega_0 t} dt \quad (3.16)$$

where C_n can be a complex number.

$$\int_0^{2\pi} \sin(ut) \sin(vt) dt = 0, \quad \text{for } u \geq 1, v \geq 1, u \neq v \quad (3.17)$$

$$\int_0^{2\pi} \cos(ut) \cos(vt) dt = 0, \quad \text{for } u \geq 1, v \geq 1, u \neq v \quad (3.18)$$

$$\int_0^{2\pi} \sin(ut) \cos(vt) dt = 0, \quad \text{for } u \geq 1, v \geq 1 \quad (3.19)$$

Consider a non-periodic, but the finite integral of absolute value signal, a more general expression of the Fourier transform is shown as

$$F(\omega) = \int_{-\infty}^{\infty} f(t) e^{-j\omega t} dt \quad (3.20)$$

$$f(t) = \frac{1}{2\pi} \int_{-\infty}^{\infty} F(\omega) e^{j\omega t} d\omega \quad (3.21)$$

It indicates that a signal in time-domain can be described as a distinctive form in frequency-domain, and the process of transformation is invertible. The Fourier transform of derivatives and the integrals are presented as follow

$$f(t) \leftrightarrow F(\omega) \quad (3.22)$$

$$\frac{d^n f(t)}{dt^n} \leftrightarrow (j\omega)^n F(\omega) \quad (3.23)$$

$$\int_{-\infty}^{\tau} f(t) dt \leftrightarrow \frac{1}{j\omega} F(\omega) \quad (3.24)$$

Parseval's Relation, a significant characteristic in the Fourier transform, is shown below

$$\int_{-\infty}^{\infty} f^2(t) dt = \frac{1}{2\pi} \int_{-\infty}^{\infty} F(\omega) F^*(\omega) d\omega = \int_{-\infty}^{\infty} |F(\omega)|^2 d\omega \quad (3.25)$$

where the $F^*(\omega)$ indicates the complex conjugate of $F(\omega)$.

The Fourier transform can also be implemented to resolve linear differential equations with constant coefficients in linear time-invariant systems, and so forth.

$$f(t) = sy'' + uy' + vy \leftrightarrow F(\omega) = (-s\omega^2 + ju\omega + c)Y(\omega) \quad (3.26)$$

Therefore,

$$Y(\omega) = \frac{1}{-s\omega^2 + ju\omega + c} F(\omega) \quad (3.27)$$

$$H(\omega) = \frac{1}{-s\omega^2 + ju\omega + c} \quad (3.28)$$

Combining with them together, $Y(\omega) = H(\omega)F(\omega)$.

$$\begin{aligned} Y(\omega) &= \mathcal{F} \left[\int_{-\infty}^{\infty} f(\tau)g(t-\tau)d\tau \right] = \int_{-\infty}^{\infty} \int_{-\infty}^{\infty} f(\tau)g(t-\tau)e^{-j\omega t} dt d\tau \\ &= \int_{-\infty}^{\infty} \int_{-\infty}^{\infty} f(\tau)g(\theta)e^{-j\omega(\theta+\tau)} d\theta d\tau \end{aligned} \quad (3.29)$$

since $e^{-j\omega t} = e^{-j\omega(t-\tau+\tau)}$

$$= \int_{-\infty}^{\infty} e^{-j\omega\theta} g(\theta) d\theta \int_{-\infty}^{\infty} e^{-j\omega\tau} f(\tau) d\tau = H(\omega)F(\omega) \quad (3.30)$$

The system transfer function is defined as the Fourier transform of the impulse response. Another elegant characteristic of the Fourier transform is that the magnitude of the transfer function scales a sinusoidal input, and the angle of the transfer function adds to the angle of the sinusoidal input, which means

$$\begin{aligned} r(t) &= r_0 \cos(\omega_0 t + \varphi) \rightarrow \\ s(t) &= r_0 |H(\omega_0)| \cos(\omega_0 t + \varphi + \arg(H(\omega_0))) \end{aligned} \quad (3.31)$$

To prove the above relations, it is going to use the complex exponential

$$r(t) = \text{Re}(r_0 e^{-j(\omega_0 t + \varphi)}) = \text{Re}(\tilde{r}_0 e^{j\omega_0 t}) \quad (3.32)$$

Making complex $r_0 e^{j\varphi} \tilde{r}_0$, thus

$$\begin{aligned} s(t) &= h(t) * r(t) \\ &= \int_{-\infty}^{\infty} h(\tau) r(t-\tau) d\tau = \int_{-\infty}^{\infty} h(\tau) \text{Re}(\tilde{r}_0 e^{j\omega_0(t-\tau)}) d\tau \end{aligned}$$

$$\begin{aligned}
&= \operatorname{Re} \left(\int_{-\infty}^{\infty} h(\tau) e^{-j\omega_0\tau} d\tau \tilde{r}_0 e^{j\omega_0 t} \right) = \operatorname{Re} (H(\omega_0) r_0 e^{j(\omega_0 t + \varphi)}) \\
&= r_0 |H(\omega_0)| \cos(\omega_0 t + \varphi + \arg(H(\omega_0)))
\end{aligned} \tag{3.33}$$

3.3.2 Z Transform

Z transform is another useful technique of transformation to process and analyse the signal in its z-plane. For instance, a typical difference equation may be represented as

$$\begin{aligned}
f(n) &= (r_0 x(n) + r_1 x(n-1) + \dots + r_N x(n-N)) \\
&\quad - (s_0 f(n-1) + s_1 x(n-2) + \dots + s_M x(n-K))
\end{aligned} \tag{3.34}$$

The coefficients r_i and s_i are constant coefficients and affect the system response. N and K determine the number of past inputs and outputs, respectively. Now consider a time function $g(t)$, the Z transform of $g(t)$ is determined by $G(z)$, and can be calculated with

$$G(z) = g(0)z^0 + g(1)z^{-1} + g(2)z^{-2} + \dots = \sum_{n=0}^{\infty} g(n) z^{-n} \tag{3.35}$$

The time samples $g(n)$ are the mean of $g(nT)$. Meanwhile, equation (5.8) can be interpreted in the time domain. Let $g(n)$ delayed by one sample be $\tilde{g}(n)$, therefore, according to the definition of the differential equation, $\tilde{g}(n) = g(n-1)$.

$$G(z) = g(0)z^0 + g(1)z^{-1} + g(2)z^{-2} + \dots \tag{3.36}$$

thus,

$$\begin{aligned}
\tilde{G}(z) &= \tilde{g}(0)z^0 + \tilde{g}(1)z^{-1} + \tilde{g}(2)z^{-2} + \dots \\
&= \tilde{g}(0)z^0 + z^{-1}(\tilde{g}(1)z^0 + \tilde{g}(2)z^{-1} + \dots) \\
&= g(-1)z^0 + z^{-1}(g(0)z^0 + g(1)z^{-1} + \dots) \\
&= g(-1)z^0 + z^{-1}G(z)
\end{aligned} \tag{3.37}$$

assuming zero initial circumstance, $g(t) = 0$ for $t < 0$ and $g(-1) = 0$, so that

$$\tilde{G}(z) = z^{-1}G(z) \tag{3.38}$$

To recapitulate, it indicates that multiplying by z^{-1} means to a delay of one sample. On the other hand, multiplying by z^{-n} means to a delay of n samples. The Z transform also easily allows us to

construct a system transfer function, which can be emphasized in a computer algorithm using the corresponding difference equation.

$$G(z) = H(z)F(z) \quad (3.39)$$

which means that the outcome of a linear, time-invariant system is equivalent to the input $F(z)$ multiplied by the transfer function $H(z)$. However, the time-domain functions cannot be presented to the multiplication as the z transfer functions

$$g(n) = h(n)f(n) \quad (3.40)$$

Furthermore, consider a decaying exponential time function $g(t) = e^{-\omega t}$, and therefore the sampled version is $g(nT) = e^{-\omega nT}$,

$$\begin{aligned} G(z) &= g(0)z^0 + g(1)z^{-1} + g(2)z^{-2} + \dots \\ Z(e^{-\omega t}) &= e^0 z^0 + e^{-\omega t} z^{-1} + e^{-2\omega t} z^{-2} + \dots \\ &= 1 + e^{-\omega t} z^{-1} (1 + e^{-\omega t} z^{-1} + e^{-2\omega t} z^{-2} + \dots) \\ &= 1 + e^{-\omega t} z^{-1} G(z) \end{aligned} \quad (3.41)$$

Therefore,

$$G(z) = \frac{1}{1 - e^{-\omega t} z^{-1}} \quad (3.42)$$

Z transform is expected as negative powers of z in that only the present or past samples can be accessed. Multiplying by z/z , the final Z transform of $e^{-\omega t}$ is presented to

$$Z(e^{-\omega t}) = \frac{z}{z - e^{-\omega t}} \quad (3.43)$$

A sine waveform can be implemented to examine the system response.

$$r(n) = A \sin(\omega t) \quad (3.44)$$

Using the exponential of a complex number, $\sin(\omega t)$ can be expressed as

$$\sin(\omega t) = \frac{1}{2j} (e^{j\omega t} - e^{-j\omega t}) \quad (3.45)$$

Applying the result of equation (5.xx2) for the Z transform of $e^{-\omega t}$

$$Z(\sin(\omega t)) = \frac{1}{2j} \left(\frac{z}{z - e^{j\omega t}} - \frac{z}{z - e^{-j\omega t}} \right)$$

$$\begin{aligned}
&= \frac{z}{2j} \left(\frac{(z - e^{-j\omega t}) - (z - e^{j\omega t})}{(z - e^{j\omega t})(z - e^{-j\omega t})} \right) \\
&= \frac{z}{2j} \left(\frac{e^{j\omega t} - e^{-j\omega t}}{z^2 + z(e^{j\omega t} + e^{-j\omega t}) + 1} \right) \\
&= \frac{z}{2j} \left(\frac{2j \sin(\omega t)}{z^2 + 2z \cos(\omega t) + 1} \right) \tag{3.46}
\end{aligned}$$

Further properties and characteristics of Z transform will be presented in chapter 5.

3.3.3 Laplace Transforms

Laplace transform can also be implemented to signal processing realm, apart from calculating system responses and transfer functions. Consider a function $f: R^+ \rightarrow R$, the Laplace transform projects f to a function $F = \mathcal{L}f: C^+ \rightarrow C$ of a complex variable. It can be defined as

$$F(\omega) = \int_0^{\infty} e^{-\omega x} f(x) dx, \quad \text{Res} > \omega_0 \tag{3.47}$$

The linearity of the transform can be presented as

$$\begin{aligned}
\mathcal{L}(mf + nh) &= \int_0^{\infty} e^{-\omega x} (mf(x) + nh(x)) dx \\
&= m \int_0^{\infty} e^{-\omega x} f(x) dx + n \int_0^{\infty} e^{-\omega x} h(x) dx = m\mathcal{L}f + n\mathcal{L}h \tag{3.48}
\end{aligned}$$

The derivation of the Laplace transform can be calculated.

$$\begin{aligned}
\mathcal{L} \frac{df}{dx} &= \int_0^{\infty} e^{-\omega x} f'(x) dx = e^{-\omega x} f(x) \Big|_0^{\infty} + \omega \int_0^{\infty} e^{-\omega x} f(x) dx \\
&= -f(0) + \omega \mathcal{L}f \tag{3.49}
\end{aligned}$$

thus

$$\mathcal{L} \frac{df}{dx} = \omega \mathcal{L}f - f(0) = \omega F(x) - f(0) = -f(0) + \omega \mathcal{L}f \tag{3.50}$$

Since differentiation corresponds to multiplication with ω , it can be expressed as the integration corresponds to division by ω , which has

$$\mathcal{L} \int_0^x f(\mu) d\mu = \int_0^x \left(e^{-\omega x} \int_0^x f(\mu) d\mu \right) dx$$

$$\begin{aligned}
&= -\frac{e^{-\omega x}}{\omega} \int_0^x e^{-\omega \mu} f(\mu) d\mu \Big|_0^\infty + \int_0^x \frac{e^{-\omega x}}{\omega} f(\mu) d\mu \\
&= \frac{1}{\omega} \int_0^\infty e^{-\omega \mu} f(\mu) d\mu
\end{aligned} \tag{3.51}$$

therefore,

$$\mathcal{L} \int_0^x f(\mu) d\mu = \frac{1}{\omega} \mathcal{L} f = \frac{1}{\omega} F(x) \tag{3.52}$$

It indicates that Integration of a time function is equivalent to dividing the Laplace transform by ω . Now consider an LTI system with zero initial states,

$$h(x) = \int_0^\infty t(x - \mu) s(\mu) d\mu \tag{3.53}$$

And its Laplace transform can be presented as

$$\begin{aligned}
H(\omega) &= \int_0^\infty e^{-\omega x} h(x) dx = \int_0^\infty e^{-\omega x} \int_0^\infty t(x - \mu) s(\mu) d\mu dx \\
&= \int_0^\infty \int_0^x e^{-\omega(x-\mu)} e^{-\omega x} t(x - \mu) s(\mu) d\mu dx \\
&= \int_0^\infty e^{-\omega \mu} s(\mu) d\mu \int_0^\infty e^{-\omega x} h(x) dx = T(\omega) S(\omega)
\end{aligned} \tag{3.54}$$

It can also be described as $H(\omega) = T(\omega)S(\omega)$ where T, S, and H are the Laplace transform of t, s, and h. A mathematical interpretation is that the Laplace transform of a convolution is one reason why Laplace transform has been prevailing in control systems and other applications.

$$\omega F(\omega) = MF(\omega) + NS(\omega) \tag{3.55}$$

$$T(\omega) = UF(\omega) + VS(\omega) \tag{3.56}$$

Eliminating of $F(\omega)$ gives

$$T(\omega) = (U[\omega I - M]^{-1}N + V)S(\omega) \tag{3.57}$$

The transfer function is thus $H(\omega) = U[\omega I - M]^{-1}N + V$. It indicates that the Laplace transform of the output is the product of the transfer function of the system and the transform of the input.

This chapter introduces several prevailing ranging techniques for high-precision performance. It begins with the process of I/Q detection of coherent ranging technique and introduces an ice-penetrating FMCW radar (ApRES) with the phase-sensitive process. FMCW radar literature is analysed

with how current systems are designed, and both advantages and disadvantages are discussed against non-coherent detection. Then non-coherent technique and an MTI system are presented, and the ROC curve is introduced to evaluate the performance of radar detectors. The rest of the chapter describes three mathematical transformation tools that will be used in the following chapters, namely, Fourier transform, Z transform, and Laplace transform.

4. Non-coherent Range Estimation by Peak Detection and Chirp Z Transform Method

The previous chapter summarises current range estimation techniques that are applied to get good performance, as well as three useful mathematical tools for signal transformation. Now, this chapter is going to present one estimation technique of K th-order polynomial interpolation (KPI) in the DFT domain, which is one of the main works of the thesis, to acquire desirable ranging precision. Method description, algorithm realisation and mathematical derivation will be introduced as follow.

4.1 Method Description of Peak Detection

As introduced in chapter 3, various techniques and algorithms [86-102] have been presented to achieve high-performance range estimation, and several papers suggested a two-step approach for accurate frequency estimation in the DFT domain. An N -point DFT is implemented to find the rough estimate; then a fine estimation is applied to the location around the peak determined in the previous procedure; a similar approach applied to fine Doppler estimation is described in [14, 15] which focus on the peak of the specific DFT samples as well.

As samples of the peak of an asinc component in the DFT output, they are substantially above the noise level to trigger a target judgment threshold as responses [15]. However, a DFT sample will not present identically on the peak of asinc function. Therefore, the magnitude of the DFT sample accounts for detection, but its frequency is approximate to the actual location of the asinc peak. Notably, the error can be as much as one-half Doppler bin, which is equivalent to $PRF/2K$ Hertz (K is the number of sampling), in terms of the estimation of Doppler frequency.

If the size K of the Discrete Fourier transform is considerably more significant than the length of data sequence M , a few of DFT samples will fall on the main lobe of the asinc function, and the largest one among them can be seen as a reasonable estimate of the asinc peak to some extent. Nevertheless, when $K = M$ and sometimes, with the use of data turning, it is even true that $K < M$. In these cases, the Doppler samples are far away with each other, and an error of half-bin is unacceptable. Under such circumstance, interpolation in the vicinity of the DFT peak is one feasible solution to enhance the estimate performance of the true Doppler frequency F_D .

Zero-padding (and process a larger DFT) is one of the simplified approaches to implement such interpolation. Still, it lacks computational efficiency, since it indicates to interpolate all of the spectra.

Zero-padding is less feasible if precise sampling is required to process only a short segment of the spectrum

From a digital signal processing theoretical point of view, correct interpolation involves using all of the DFT data samples and an asinc interpolation kernel (effectively, computing a larger DFT). To understand this technique, consider computing the DTFT at an arbitrary value of ω , using only the available DFT samples. This can be done by computing the inverse DFT to recover the original time-domain data, and then computing the DTFT from those samples

$$\begin{aligned}
 Y(\omega) &= \sum_{n=0}^{N-1} y[n]e^{-j\omega n} = \\
 &= \sum_{n=0}^{N-1} \left(\frac{1}{K} \sum_{k=0}^{K-1} y[k]e^{+j2\pi\omega n/K} \right) e^{-j\omega n} \\
 &= \frac{1}{K} \sum_{k=0}^{K-1} y[k] \left\{ \sum_{n=0}^{N-1} \exp \left[-jn \left(\omega - \frac{2\pi k}{K} \right) \right] \right\}
 \end{aligned} \tag{4.1}$$

The term in parentheses is the interpolating kernel. It can be expressed in closed form as

$$\begin{aligned}
 &\sum_{n=0}^{N-1} \exp \left[-jn \left(\omega - \frac{2\pi k}{K} \right) \right] \\
 &= \exp \left[-j \left(\omega - \frac{2\pi k}{K} \right) (N-1)/2 \frac{\sin \left[\left(\omega - \frac{2\pi k}{K} \right) N/2 \right]}{\sin \left[\left(\omega - \frac{2\pi k}{K} \right) /2 \right]} \right] \\
 &\equiv Q_{N,K}(\omega, k)
 \end{aligned} \tag{4.2}$$

Combining these gives

$$Y(\omega) = \frac{1}{K} \sum_{k=0}^{K-1} Y[k] Q_{N,K}(\omega, k) \tag{4.3}$$

Equations (4.1) and (4.2) can be used to compute the DTFT at any single value of ω from the DFT samples. Thus, it can be applied to interpolate the values of the DFT over localised regions with any desired sample spacing. However, it remains relatively computationally expensive.

4.2 Algorithm Realisation by Polynomial Interpolation

4.2.1 Quadratic Interpolation

An uncomplicated and efficient technique for interpolating local peaks is illustrated in Figure 4.1. For each detected peak in the magnitude of the DFT output, a second-order polynomial is fit through that peak and the two adjacent magnitude data samples. Once the parabola coefficients are known, the amplitude and frequency of its peak are easily found by differentiating the formula for the parabola and setting the result to zero.

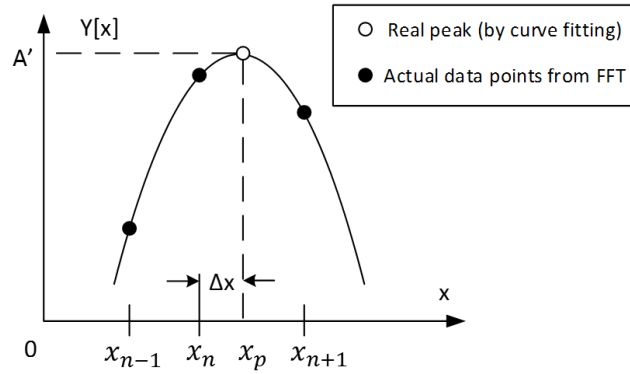


Figure 4.1 Quadratic interpolation around the DFT peak

To develop this technique, assume that the DFT $Y[x]$ is a function of a continuous frequency index x , since the goal is to estimate a peak location assumed to be between actual sample locations. In the vicinity of the DFT peak at x_n , assume that $Y[x]$ is of the form

$$Y[x] = ax^2 + bx + c \quad (4.4)$$

Now consider the three measurements $Y[x_n - 1]$, $Y[x_n]$, and $Y[x_n + 1]$ (written as y_{n-1} , y_n , and y_{n+1} respectively for the convenience of expression). If Eq. (4.4) is to be applied, these measurements must satisfy the system of equations

$$\begin{bmatrix} y_{n-1} \\ y_n \\ y_{n+1} \end{bmatrix} = \begin{bmatrix} (x_n - 1)^2 & x_n - 1 & 1 \\ x_n^2 & x_n & 1 \\ (x_n + 1)^2 & x_n + 1 & 1 \end{bmatrix} \begin{bmatrix} a \\ b \\ c \end{bmatrix} \quad (4.5)$$

The matrix of coefficients in Eq. (4.5) has the structure of a Vandermonde matrix; its determinant is

$$\begin{vmatrix} (x_n - 1)^2 & x_n - 1 & 1 \\ x_n^2 & x_n & 1 \\ (x_n + 1)^2 & x_n + 1 & 1 \end{vmatrix} = [x_n - (x_n - 1)][(x_n + 1) - x_n][(x_n + 1) - (x_n - 1)] = 2 \quad (4.6)$$

Since the determinant is nonzero, a unique solution to this system of equations exists. The coefficients of the interpolating polynomial can be obtained by solving the matrix Eq. (4.5) or by a variety of other interpolation analysis methods, all of which will lead to the same answer because it is unique.

Assume the peak location x_p in the form $x_p = x_n + \Delta x$ (see Fig. 4.1); thus, Δx is the location of the interpolated peak relative to the index of the central sample of the three DFT samples being used for the estimate. Then the second-order polynomial passing through the three samples can be written as

$$Y[x_n + \Delta x] = \frac{1}{2} \{ (\Delta x - 1)(\Delta x)y_{n-1} - 2(\Delta x - 1)(\Delta x + 1)y_n + (\Delta x + 1)(\Delta x)y_{n+1} \} \quad (4.7)$$

Differentiating this equation concerning Δx , setting the results to zero, and solving for Δx gives the estimated location of the parabola peak relative to x_n as

$$\Delta x = \frac{y_{n-1} - y_{n+1}}{2(y_{n-1} - 2y_n + y_{n+1})} (x_{n+1} - x_n) \quad (4.8)$$

The amplitude of the estimated peak $A' = Y[x_n + \Delta x]$ is determined by computing Δx and then using that result in Equation (4.7). Note that the formula for Δx (i.e., for a displacement of the estimated peak from the central sample) behaves in intuitively satisfying ways. If the first and the third DFT magnitude samples are equal, $\Delta x = 0$; the middle sample is the estimated peak. If the second and third samples are equal, $\Delta x = \frac{1}{2}$, showing the estimated peak is halfway between the two samples; a similar result exists if the first and second DFT magnitude samples are equal.

4.2.2 Cubic Interpolation

To develop further this technique, applying cubic interpolation to it, in the vicinity of the DFT peak at x_n , assume that $Y[x]$ is of the form

$$Y[x] = ax^3 + bx^2 + cx + d \quad (4.9)$$

Now consider the five measurements $|Y[x_n - 2]|$, $|Y[x_n - 1]|$, $|Y[x_n]|$, $|Y[x_n + 1]|$, $|Y[x_n + 2]|$ (written as y_{n-2} , y_{n-1} , y_n , y_{n+1} , and y_{n+2} respectively for the convenience of expression).

Note that we only need four points to accomplish the process of calculation. Therefore, there are two options to select four points for the interpolation. According to the analysis of these two different

choices, the quantitative distinction of ultimate consequences are almost negligible. However, to improve the accuracy of interpolation, it is plausible to choose the larger one between y_{n-2} and y_{n+2} .

Assuming y_{n-2} is the larger one now and applying Equation (4.9), these measurements will still satisfy the system of equations shown below

$$\begin{bmatrix} y_{n-2} \\ y_{n-1} \\ y_n \\ y_{n+1} \end{bmatrix} = \begin{bmatrix} (x_n - 2)^3 & (x_n - 2)^2 & x_n - 2 & 1 \\ (x_n - 1)^3 & (x_n - 1)^2 & x_n - 1 & 1 \\ x_n^3 & x_n^2 & x_n & 1 \\ (x_n + 1)^3 & (x_n + 1)^2 & x_n + 1 & 1 \end{bmatrix} \begin{bmatrix} a \\ b \\ c \\ d \end{bmatrix} \quad (4.10)$$

As shown before, the matrix of coefficients in Equation (4.10) has the structure of a Vandermonde matrix as well; its determinant is

$$\begin{vmatrix} (x_n - 2)^3 & (x_n - 2)^2 & x_n - 2 & 1 \\ (x_n - 1)^3 & (x_n - 1)^2 & x_n - 1 & 1 \\ x_n^3 & x_n^2 & x_n & 1 \\ (x_n + 1)^3 & (x_n + 1)^2 & x_n + 1 & 1 \end{vmatrix} \neq 0 \quad (4.11)$$

Therefore, a unique solution to this system of equations exists. As mentioned above, the coefficients of the interpolating polynomial can be obtained by solving the matrix Equation (4.10) or by other analysis approaches, all of which will lead to the same unique answer.

Assume Δx is still the location of the interpolated peak relative to the index of the central sample of the four DFT samples being applied to the estimate. The estimated location of the cubic peak relative to x_n can be obtained through the similar derivation described above, which is

$$\Delta x = \frac{y_{n-1} - 2y_n + y_{n+1}}{2(y_{n-2} - 3y_{n-1} + 3y_n - y_{n+1})} (x_{n+1} - x_n) \quad (4.12)$$

Now assuming y_{n+2} is the larger one and applying Eq. (4.9), the system of equations is shown below

$$\begin{bmatrix} y_{n-1} \\ y_n \\ y_{n+1} \\ y_{n+2} \end{bmatrix} = \begin{bmatrix} (x_n - 1)^3 & (x_n - 1)^2 & x_n - 1 & 1 \\ x_n^3 & x_n^2 & x_n & 1 \\ (x_n + 1)^3 & (x_n + 1)^2 & x_n + 1 & 1 \\ (x_n + 2)^3 & (x_n + 2)^2 & x_n + 2 & 1 \end{bmatrix} \begin{bmatrix} a \\ b \\ c \\ d \end{bmatrix} \quad (4.13)$$

And its Vandermonde determinant is

$$\begin{vmatrix} (x_n - 1)^3 & (x_n - 1)^2 & x_n - 1 & 1 \\ x_n^3 & x_n^2 & x_n & 1 \\ (x_n + 1)^3 & (x_n + 1)^2 & x_n + 1 & 1 \\ (x_n + 2)^3 & (x_n + 2)^2 & x_n + 2 & 1 \end{vmatrix} \neq 0 \quad (4.14)$$

The location of the interpolated peak relative to the index of the central sample of the four DFT samples Δx now can be written as

$$\Delta x = \frac{y_{n-1} - 2y_n + y_{n+1}}{2(y_{n-1} - 3y_n + 3y_{n+1} - y_{n+2})} (x_{n+1} - x_n) \quad (4.15)$$

The amplitude of the estimated peak $A' = Y[x_n + \Delta x]$ is therefore determined as well.

4.2.3 Quartic Interpolation

Now consider quartic interpolation, in the vicinity of the DFT peak at x_n , assume that $Y[x]$ is of the form

$$Y[x] = ax^4 + bx^3 + cx^2 + dx + e \quad (4.16)$$

Applying the five measurements $Y[x_n - 2]$, $Y[x_n - 1]$, $Y[x_n]$, $Y[x_n + 1]$, and $Y[x_n + 2]$ (written as y_{n-2} , y_{n-1} , y_n , y_{n+1} , and y_{n+2} respectively for the convenience of expression), with Equation (4.16), these measurements will still satisfy the system of equations

$$\begin{bmatrix} y_{n-2} \\ y_{n-1} \\ y_n \\ y_{n+1} \\ y_{n+2} \end{bmatrix} = \begin{bmatrix} (x_n - 2)^3 & (x_n - 2)^2 & x_n - 2 & 1 \\ (x_n - 1)^3 & (x_n - 1)^2 & x_n - 1 & 1 \\ x_n^3 & x_n^2 & x_n & 1 \\ (x_n + 1)^3 & (x_n + 1)^2 & x_n + 1 & 1 \\ (x_n + 2)^3 & (x_n + 2)^2 & x_n + 2 & 1 \end{bmatrix} \begin{bmatrix} a \\ b \\ c \\ d \\ e \end{bmatrix} \quad (4.17)$$

Its Vandermonde determinant is

$$\begin{vmatrix} (x_n - 2)^3 & (x_n - 2)^2 & x_n - 2 & 1 \\ (x_n - 1)^3 & (x_n - 1)^2 & x_n - 1 & 1 \\ x_n^3 & x_n^2 & x_n & 1 \\ (x_n + 1)^3 & (x_n + 1)^2 & x_n + 1 & 1 \\ (x_n + 2)^3 & (x_n + 2)^2 & x_n + 2 & 1 \end{vmatrix} \neq 0 \quad (4.18)$$

A unique solution to this system of equations exists, and the coefficients of the interpolating polynomial can be calculated. Assume Δx is still the location of the interpolated peak relative to the index of the central sample of the five DFT samples being applied to the estimate, then the estimated location of the cubic peak relative to x_n can be written as

$$(x + y)^k = \sum_{i=0}^k \binom{k}{i} x^{k-i} y^i \quad (4.21)$$

Integrated with derivation and induction, a general equation for K th order polynomial interpolator can be acquired and presented by the form of binomial coefficients eventually; the location of the interpolated peak relative to the index of the central sample of the applied DFT samples Δx can be written as

$$\Delta x = \begin{cases} \frac{\sum_{i=0}^k (-1)^{2i+1} \binom{k}{i} y_{n-k+i+2}}{2 \left[\left(\sum_{j=0}^k (-1)^{2j+1} \binom{k}{i} y_{n-k+j+1} \right) - y_{n+\frac{k+1}{2}} \right]} , & k \text{ is odd} \\ \frac{\sum_{i=0}^k (-1)^{2i+1} \binom{k}{i} y_{n-k+i+2} - (-1)^{2n+1} \binom{k}{n} y_n}{2 \sum_{j=0}^k (-1)^{2j+1} \binom{k}{i} y_{n-k+j+1}} , & k \text{ is even} \end{cases} \quad (4.22)$$

where $\binom{k}{i}$ is the corresponding coefficient of the binomial described above. Note that since the symmetrical property of an K th order polynomial will be different when K is odd or even, it is plausible to have a unique representation for different circumstances, respectively.

4.3 Method Description of Chirp-Z transform

Another non-coherent ranging technique is presented in this chapter. The fundamental definition of Z transform is described firstly, following by the algorithm realisation by Most-likelihood chirp Z transform (MLCZT). The CZT accurately implements the periodogram where only a narrow band spectrum is processed, and the concept of most-likelihood estimator is introduced to combine with CZT to acquire better ranging performance.

The algorithm stems from the values of the Z-transform on a circular or spiral contour can be expressed as a discrete convolution. For N and K moderately broad, the computation complexity is approximately proportional to $(K + N)/\log_2(K + N)$, while it will be proportional to $N \cdot K$ for calculation of the Z-transform at N points directly. Generally, using the K samples CZT algorithm can quickly calculate the Z transform at N points in the z-plane which lie on circular or spiral contours beginning at any arbitrary point in the z-plane. The angular spacing of the points is an arbitrary constant, and N and K are arbitrary integers [16]. This algorithm can be extended to the application of multi-target ranging and location as well, after the integration of iteration and state-transfer matrix.

[16] presented the fundamental concept and properties of Z transform. The Z-transform of a series of numbers y_k can be presented as

$$Y(z) = \sum_{k=-\infty}^{\infty} y_k z^{-k} \quad (4.23)$$

Now limit to the Z-transform with only a finite number K of nonzero points. Under such circumstance, it can be expressed as

$$Y(z) = \sum_{k=0}^{K-1} y_k z^{-k} \quad (4.24)$$

where the sum of the above expression converges for all z except $z = 0$.

Equations (4.23) and (4.24) are similar to the expressions of the Laplace transform for a set of equally divided impulses of magnitudes y_k . Set the interval of the impulses to be T , and the series of impulses be $\sum_k y_k \delta(t - kT)$. Then the Laplace transform is $\sum_k y_k e^{-skT}$ which is the same as $Y(z)$ if we let

$$z = e^{sT} \quad (4.25)$$

The Laplace transform of a set of impulses reiterate its quantities in a horizontal outline of the s -plane with the parallel interval of $2\pi/T$, while the Z-transform projects each of them into the whole z -plane, vice versa. The exterior is parallel to the right half of the s -plane, and the interior of the z -plane unit circle is parallel to the left half. Straight lines in the s -plane correspond to circles or spirals in the z -plane. Values of the Z-transform are typically calculated by the path of the $j\omega$ axis (unit circle). It is entirely equivalent to the Fourier transform and can be implemented to distinctive applications including the spectrum estimation, matched filtering, interpolation, and correlation. Now only calculate (4.24) at a finite number of points z_n

$$Y_n = Y(z_n) = \sum_{k=0}^{K-1} y_k z_n^{-k} \quad (4.26)$$

Assuming the series of points equally separated on the unit circle

$$z_n = \exp(j2\pi n/M), \quad n = 0, 1, \dots, M-1 \quad (4.27)$$

for which

$$Y_n = \sum_{k=0}^{K-1} y_k \exp(-j2\pi kn/M), \quad n = 0, 1, \dots, M-1 \quad (4.28)$$

Equation (4.28) is the well-known discrete Fourier transform. Now examine Z transform on a more general form

$$z_n = BS^{-n}, \quad n = 0, 1, \dots, N-1 \quad (4.29)$$

where M is an arbitrary integer and B and S are of the form

$$B = B_0 e^{j2\pi\omega_0} \quad (4.30)$$

and

$$S = S_0 e^{j2\pi\theta_0} \quad (4.31)$$

The case $B = 1$, $N = M$, and $S = \exp(-j2\pi/M)$ are equivalent to the DFT (refer to Figure 6.10). The general z -plane contour starts with the point $z = B$, and it is determined by the value of S , spirals in or out in terms of the start position. If $S_0 = 1$, the outline is an arc of a circle, while the angular spacing of the samples is $2\pi\theta_0$.

We can apply the FFT to compute the Z transform along the outline by using the sequence $S^{m^2/2}$. When $S_0 = 1$, the sequence $S^{m^2/2}$ is a complex sinusoid of linearly increasing frequency, and since a similar waveform used in some radar systems that we call it chirp, the algorithm is therefore named as the chirp Z transform (CZT). Furthermore, the extra benefits provided by the CZT include several aspects. The number of time samples can be unequal to the samples of the Z transform; Meanwhile, N and M need not be composite integers. Besides, point z_0 and the angular spacing of the z_n can be arbitrary.

4.4 Algorithm Realisation by Most-likelihood Chirp Z Transform

Following the thought introduced before, let us rewrite the expression of the CZT

$$Y_n = \sum_{k=0}^{K-1} y_k B^{-k} S^{kn}, \quad n = 0, 1, \dots, M-1 \quad (4.32)$$

Using the substitution

$$kn = \frac{k^2 + n^2 - (n-k)^2}{2} \quad (4.33)$$

For the exponent of S in (4.32), thus

$$Y_n = \sum_{k=0}^{K-1} y_k B^{-k} S^{(k^2/2)} S^{(n^2/2)} S^{-(n-k)^2/2} \quad (4.34)$$

where $n = 0, 1, \dots, M-1$. After the observation, (4.34) contains a three-step method.

Construct a new sequence g_k through weighting the y_k

$$g_k = y_k B^{-k} S^{k^2/2}, \quad n = 0, 1, \dots, M - 1 \quad (4.35)$$

Convolving g_k with the sequence r_k defined as

$$r_k = S^{-k^2/2} \quad (4.36)$$

to give a sequence h_n

$$h_n = \sum_{k=0}^{K-1} y_k r_{n-k}, \quad n = 0, 1, \dots, M - 1 \quad (4.37)$$

Multiplying h_n by $S^{n^2/2}$ to get Y_n

$$Y_n = h_n S^{n^2/2}, \quad n = 0, 1, \dots, M - 1 \quad (4.38)$$

The computational speed and flexibility of the CZT algorithm are related to the FFT. As known, ordinary convolutions can be calculated by adding zeroes to the end of one or both sequences so that the correct numerical consequences for the initial convolution can be derived by a circular convolution.

The procedures of the MLCZT algorithm can be described as follow:

- 1) Calculate a coarse FFT with a sequence of K points;
- 2) Search for the local maximum on the specific FFT range bin and locate its corresponding frequency in $\hat{\omega}$;
- 3) Set P as the desirable MLCZT frequency precision;
- 4) Calculate the CZT within the region $\left(\hat{\omega} - \frac{\pi}{K}, \hat{\omega} + \frac{\pi}{K}\right)$, and search for the maximum via Most-likelihood method, using the foreknowledge to asymptotically reach to the MVU estimator;
- 5) Repeat step 4 until attaining desirable precision of range performance.

Such thought could be easily extended to the applications of multi-target ranging estimation, which the procedures of the extended MLCZT algorithm for multi-target estimation can be presented as:

- 1) Calculate a coarse FFT with a sequence of K points;
- 2) Search for the local maximum on the specific FFT range bin and locate its corresponding frequency in $\hat{\omega}$;
- 3) Set P as the desirable MLCZT frequency precision;
- 4) For $u = 1, 2, \dots, r_u$,
 - (1) Calculate the CZT within the region $\left(\hat{\omega}_u - \frac{\pi}{K}, \hat{\omega}_u + \frac{\pi}{K}\right)$
 - (2) Search for the maximum via Most-likelihood method
 - (3) Using the foreknowledge to asymptotically reach to the MVU estimator;
- 5) Repeat step 4 until attaining desirable precision of range performance.

As mentioned previously, since the outline of the MLCTZ is a straight line segment in the s-plane, it is that reiterated application of the MLCZT can calculate the Z transform by a part of spiral in the z-plane or linear in the s-plane. For the scenario of all data samples on the unit circle in the MLCZT algorithm, the Z transform is similar to a Fourier transform. Unlike the DFT, given K points transform for K points of signal data, M and K can be unequal in the MLCZT. Moreover, the z_k can be equally spaced along an arc, not necessarily over the whole unit circle. Still, the MLCZT provides the degree of freedom to choose any value of K, without strongly affecting the computational speed.

4.5 Mathematical Derivation of Most-likelihood Process in Chirp Z Transform

In this section, a simplified signal model is introduced to validate the effectiveness of the most-likelihood process in chirp Z transform. Consider the estimation model $z_n = As_n + w_n$, $n = 0, 1, 2, \dots, N - 1$, where w_n is the zero-mean white Gaussian noise, and $\text{Var}(w_n) = \sigma^2$.

The estimation model can be written as the vector form

$$\mathbf{z} = A\mathbf{s} + \mathbf{w} \quad (4.39)$$

where $\mathbf{z} = (z_0, z_1, \dots, z_{N-1})^T$, $\mathbf{s} = (s_0, s_1, \dots, s_{N-1})^T$, $\mathbf{w} = (w_0, w_1, \dots, w_{N-1})^T$.

letting $\boldsymbol{\theta} = (A, \sigma^2)^T$, the joint PDF of the estimation model is

$$p(\mathbf{z}; A, \sigma^2) = \left(\frac{1}{2\pi\sigma^2}\right)^{N/2} \exp\left\{-\frac{1}{2\sigma^2}(\mathbf{z} - A\mathbf{s})^T(\mathbf{z} - A\mathbf{s})\right\} \quad (4.40)$$

The likelihood function of the log form of $\boldsymbol{\theta} = (A, \sigma^2)^T$ can be presented as

$$\begin{aligned} l(\boldsymbol{\theta}) &= \ln p(\mathbf{z}; A, \sigma^2) \\ &= -\frac{N}{2} \ln(2\pi) - \frac{N}{2} \ln(\sigma^2) - \frac{1}{2\sigma^2} (\mathbf{z} - A\mathbf{s})^T (\mathbf{z} - A\mathbf{s}) \end{aligned} \quad (4.41)$$

The first order of derivation is

$$\frac{\partial l(\boldsymbol{\theta})}{\partial A} = -\frac{1}{2\sigma^2} \cdot 2 \cdot (-\mathbf{s})^T (\mathbf{z} - A\mathbf{s}) = \frac{1}{\sigma^2} (\mathbf{s}^T \mathbf{z} - A\mathbf{s}^T \mathbf{s}) \quad (4.42)$$

and

$$\begin{aligned}\frac{\partial l(\boldsymbol{\theta})}{\partial \sigma^2} &= -\frac{N}{2} \frac{1}{\sigma^2} - \frac{1}{2} \frac{-1}{(\sigma^2)^2} (\mathbf{z} - A\mathbf{s})^T (\mathbf{z} - A\mathbf{s}) \\ &= \frac{N}{2(\sigma^2)^2} \left[\frac{1}{N} (\mathbf{z} - A\mathbf{s})^T (\mathbf{z} - A\mathbf{s}) - \sigma^2 \right]\end{aligned}\quad (4.42)$$

letting

$$\frac{\partial l(\boldsymbol{\theta})}{\partial \boldsymbol{\theta}} = \mathbf{0} \quad (4.44)$$

The most-likelihood estimation of $\boldsymbol{\theta}$,

$$\hat{\boldsymbol{\theta}}_{ml} = (\hat{A}_{ml}, \hat{\sigma}_{ml}^2)^T \quad (4.45)$$

where

$$\hat{A}_{ml} = (\mathbf{s}^T \mathbf{s})^{-1} \mathbf{s}^T \mathbf{z} \quad (4.46)$$

$$\hat{\sigma}_{ml}^2 = \frac{1}{N} (\mathbf{z} - \hat{A}_{ml} \mathbf{s})^T (\mathbf{z} - \hat{A}_{ml} \mathbf{s}) \quad (4.47)$$

Substituting \hat{A}_{ml} into the expression of $\hat{\sigma}_{ml}^2$

$$\begin{aligned}\hat{\sigma}_{ml}^2 &= \frac{1}{N} (\mathbf{z} - \mathbf{s}(\mathbf{s}^T \mathbf{s})^{-1} \mathbf{s}^T \mathbf{z})^T (\mathbf{z} - \mathbf{s}(\mathbf{s}^T \mathbf{s})^{-1} \mathbf{s}^T \mathbf{z}) \\ &= \frac{1}{N} \mathbf{z}^T [\mathbf{I}_N - \mathbf{s}(\mathbf{s}^T \mathbf{s})^{-1} \mathbf{s}^T] [\mathbf{I}_N - \mathbf{s}(\mathbf{s}^T \mathbf{s})^{-1} \mathbf{s}^T] \mathbf{z} \\ &= \frac{1}{N} \mathbf{z}^T [\mathbf{I}_N - \mathbf{s}(\mathbf{s}^T \mathbf{s})^{-1} \mathbf{s}^T] \mathbf{z} \\ &\stackrel{def}{=} \frac{1}{N} \mathbf{z}^T [\mathbf{I}_N - \mathbf{P}] \mathbf{z}\end{aligned}\quad (4.48)$$

where

$$\mathbf{P} = \mathbf{s}(\mathbf{s}^T \mathbf{s})^{-1} \mathbf{s}^T \quad (4.49)$$

is the projection matrix, and the idempotent matrix as well ($\mathbf{P}^2 = \mathbf{P}$). Therefore, $\mathbf{I}_N - \mathbf{P}$ is also the idempotent matrix.

Now analysing the second-order of the derivation of the likelihood function

$$\frac{\partial^2 l(\boldsymbol{\theta})}{\partial A^2} = -\frac{1}{\sigma^2} \mathbf{s}^T \mathbf{s} \quad (4.50)$$

$$\frac{\partial^2 l(\boldsymbol{\theta})}{\partial A \partial \sigma^2} = \frac{-1}{(\sigma^2)^2} (\mathbf{s}^T \mathbf{z} - A \mathbf{s}^T \mathbf{s}) \quad (4.51)$$

$$\frac{\partial^2 l(\boldsymbol{\theta})}{\partial A \partial \sigma^2} = \frac{-1}{(\sigma^2)^2} (\mathbf{s}^T \mathbf{z} - A \mathbf{s}^T \mathbf{s}) \quad (4.52)$$

$$\begin{aligned} \frac{\partial^2 l(\boldsymbol{\theta})}{\partial (\sigma^2)^2} &= \frac{-2\sigma^2}{2(\sigma^2)^4} (\mathbf{z} - A\mathbf{s})^T (\mathbf{z} - A\mathbf{s}) - \frac{-N}{2(\sigma^2)^2} \\ &= -\frac{N}{2(\sigma^2)^3} \left[\frac{1}{N} (\mathbf{z} - A\mathbf{s})^T (\mathbf{z} - A\mathbf{s}) - \frac{1}{2} \sigma^2 \right] \end{aligned} \quad (4.53)$$

Substituting \hat{A}_{ml} and $\hat{\sigma}_{ml}^2$ into (4.45), the quantity of the second order of derivation of likelihood function at $\hat{\boldsymbol{\theta}}_{ml} = (\hat{A}_{ml}, \hat{\sigma}_{ml}^2)^T$ can be expressed as

$$\left. \frac{\partial^2 l(\boldsymbol{\theta})}{\partial A^2} \right|_{\boldsymbol{\theta}=\hat{\boldsymbol{\theta}}_{ml}} = -\frac{1}{\hat{\sigma}_{ml}^2} \mathbf{s}^T \mathbf{s} \quad (4.54)$$

$$\left. \frac{\partial^2 l(\boldsymbol{\theta})}{\partial A \partial \sigma^2} \right|_{\boldsymbol{\theta}=\hat{\boldsymbol{\theta}}_{ml}} = \frac{-1}{(\hat{\sigma}_{ml}^2)^2} (\mathbf{s}^T \mathbf{z} - \hat{A}_{ml} \mathbf{s}^T \mathbf{s}) = 0 \quad (4.55)$$

$$\begin{aligned} \left. \frac{\partial^2 l(\boldsymbol{\theta})}{\partial (\sigma^2)^2} \right|_{\boldsymbol{\theta}=\hat{\boldsymbol{\theta}}_{ml}} &= -\frac{N}{2(\hat{\sigma}_{ml}^2)^3} \left[\frac{1}{N} (\mathbf{z} - \hat{A}_{ml} \mathbf{s})^T (\mathbf{z} - \hat{A}_{ml} \mathbf{s}) - \frac{1}{2} \hat{\sigma}_{ml}^2 \right] \\ &= -\frac{1}{2(\hat{\sigma}_{ml}^2)^2} \end{aligned} \quad (4.56)$$

Therefore, the Hessian matrix of the likelihood function at $\hat{\boldsymbol{\theta}}_{ml} = (\hat{A}_{ml}, \hat{\sigma}_{ml}^2)^T$ can be presented as

$$\left[\begin{array}{cc} \frac{\partial^2 l(\boldsymbol{\theta})}{\partial A^2} & \frac{\partial^2 l(\boldsymbol{\theta})}{\partial A \partial \sigma^2} \\ \frac{\partial^2 l(\boldsymbol{\theta})}{\partial A \partial \sigma^2} & \frac{\partial^2 l(\boldsymbol{\theta})}{\partial (\sigma^2)^2} \end{array} \right] \Bigg|_{\boldsymbol{\theta}=\hat{\boldsymbol{\theta}}_{ml}} = - \left[\begin{array}{cc} \frac{1}{\hat{\sigma}_{ml}^2} \mathbf{s}^T \mathbf{s} & 0 \\ 0 & \frac{N}{2(\hat{\sigma}_{ml}^2)^2} \end{array} \right] < \mathbf{0} \quad (4.57)$$

Thus, $\hat{\boldsymbol{\theta}}_{ml} = (\hat{A}_{ml}, \hat{\sigma}_{ml}^2)^T$ is indeed the maximum point of the likelihood function of log form, so that it is the most-likelihood estimation of parameter $\boldsymbol{\theta}$. Meanwhile, $\mathbf{z} \sim N(A\mathbf{s}, \sigma^2 \mathbf{I}_N)$, therefore,

$$\hat{A}_{ml} = (\mathbf{s}^T \mathbf{s})^{-1} \mathbf{s}^T \mathbf{z} \sim N(A, \sigma^2 (\mathbf{s}^T \mathbf{s})^{-1}) \quad (4.58)$$

so that \hat{A}_{ml} is the unbiased estimator of A ; while $\lim_{N \rightarrow +\infty} \mathbf{s}^T \mathbf{s} = +\infty$, \hat{A}_{ml} is also the consensus estimator.

Now investigating the PDF of $\hat{\sigma}_{ml}^2$, based on the definition of the projection matrix, $\mathbf{P}\mathbf{s} = \mathbf{s}$, $(\mathbf{I}_N - \mathbf{P})\mathbf{s} = \mathbf{0}$. Besides, the eigenvalues of the idempotent matrix can only be 1 or 0. Therefore, $\mathbf{I}_N - \mathbf{P}$ can be decomposed to

$$\mathbf{I}_N - \mathbf{P} = \mathbf{V} \begin{bmatrix} \mathbf{I}_{N-1} & \mathbf{0} \\ \mathbf{0} & \mathbf{0} \end{bmatrix} \mathbf{V}^T \quad (4.59)$$

where $\mathbf{V} = (\mathbf{v}_0, \mathbf{v}_1, \dots, \mathbf{v}_{N-1})$ is the orthogonal matrix consisting of the eigen-vectors.

$$\mathbf{V} = (\mathbf{V}_{0:N-2}, \mathbf{v}_{N-1}) \quad (4.60)$$

Letting

$$\mathbf{y} = \mathbf{V}_{0:N-2}^T \mathbf{z} \quad (4.61)$$

thus

$$E\mathbf{y} = \mathbf{V}_{0:N-2}^T E\mathbf{z} = A\mathbf{V}_{0:N-2}^T \mathbf{s} \quad (4.62)$$

and

$$(\mathbf{I}_N - \mathbf{P})\mathbf{s} = \mathbf{0} \quad (4.63)$$

therefore

$$\mathbf{V} \begin{bmatrix} \mathbf{I}_{N-1} & \mathbf{0} \\ \mathbf{0} & \mathbf{0} \end{bmatrix} \mathbf{V}^T \mathbf{s} = \mathbf{0} \quad (4.64)$$

Since \mathbf{V} is an orthogonal matrix so that it is invertible,

$$\begin{bmatrix} \mathbf{I}_{N-1} & \mathbf{0} \\ \mathbf{0} & \mathbf{0} \end{bmatrix} \begin{bmatrix} \mathbf{V}_{0:N-2}^T \\ \mathbf{v}_{N-1}^T \end{bmatrix} \mathbf{s} = \begin{bmatrix} \mathbf{V}_{0:N-2}^T \\ \mathbf{0} \end{bmatrix} \mathbf{s} = \mathbf{0} \quad (4.65)$$

where $\mathbf{V}_{0:N-2}^T \mathbf{s} = \mathbf{0}$, thus

$$E\mathbf{y} = A\mathbf{V}_{0:N-2}^T \mathbf{s} = \mathbf{0} \quad (4.66)$$

$$\text{Cov}(\mathbf{y}, \mathbf{y}) = \mathbf{V}_{0:N-2}^T \cdot \text{Cov}(\mathbf{z}, \mathbf{z}) \cdot \mathbf{V}_{0:N-2} = \sigma^2 \mathbf{I}_{N-1} \quad (4.67)$$

Obviously, $\mathbf{y} \sim N(\mathbf{0}, \sigma^2 \mathbf{I}_{N-1})$, and

$$\begin{aligned}
\hat{\sigma}_{ml}^2 &= \frac{1}{N} \mathbf{z}^T [\mathbf{I}_N - \mathbf{P}] \mathbf{z} = \frac{1}{N} \mathbf{z}^T \mathbf{V} \begin{bmatrix} \mathbf{I}_{N-1} & 0 \\ 0 & 0 \end{bmatrix} \mathbf{V}^T \mathbf{z} \\
&= \frac{1}{N} (\mathbf{y}^T, \mathbf{v}_{N-1}^T \mathbf{z}) \begin{bmatrix} \mathbf{I}_{N-1} & 0 \\ 0 & 0 \end{bmatrix} \begin{bmatrix} \mathbf{y} \\ \mathbf{v}_{N-1}^T \mathbf{z} \end{bmatrix} \\
&= \frac{1}{N} \mathbf{y}^T \mathbf{y}
\end{aligned} \tag{4.68}$$

thus,

$$\frac{N \hat{\sigma}_{ml}^2}{\sigma^2} = \frac{\mathbf{y}^T \mathbf{y}}{\sigma^2} \sim \chi^2(N-1) \tag{4.69}$$

therefore,

$$E \hat{\sigma}_{ml}^2 = \frac{N-1}{N} \sigma^2 \tag{4.70}$$

$$\text{Var}(\hat{\sigma}_{ml}^2) = \frac{2(N-1)}{N^2} \sigma^4 \tag{4.71}$$

And we can get the consequence,

$$\lim_{N \rightarrow +\infty} E \hat{\sigma}_{ml}^2 = \sigma^2 \tag{4.72}$$

$$\lim_{N \rightarrow +\infty} E [\hat{\sigma}_{ml}^2 - \sigma^2]^2 = \lim_{N \rightarrow +\infty} \{ [E \hat{\sigma}_{ml}^2 - \sigma^2]^2 + \text{Var}(\hat{\sigma}_{ml}^2) \} = 0 \tag{4.73}$$

which means that $\hat{\sigma}_{ml}^2$ is an asymptotically unbiased estimator, and it is a consensus estimator.

Now let us validate the asymptotical property of the most-likelihood estimator. Firstly, it is natural to calculate the Fisher information matrix (FIM) of the second-order derivation of the likelihood function.

$$\mathbf{I}(\boldsymbol{\theta}) = -E \frac{\partial^2 l(\boldsymbol{\theta})}{\partial \boldsymbol{\theta} \partial \boldsymbol{\theta}^T} = \begin{bmatrix} \frac{\mathbf{s}^T \mathbf{s}}{\sigma^2} & 0 \\ 0 & \frac{N}{2\sigma^4} \end{bmatrix} \tag{4.74}$$

Meanwhile, the limitation of CRLB of σ^2 can be expressed as

$$\lim_{N \rightarrow +\infty} \frac{\text{CRLB}(\sigma^2)}{\hat{\text{Var}}(\hat{\sigma}_{ml}^2)} = \frac{2\sigma^4/N}{2(N-1)\sigma^4/N^2} = 1 \tag{4.75}$$

Therefore, $\hat{\sigma}_{ml}^2$ is an asymptotically effective estimator. Particularly, according the Central Limit Theorems, $\hat{\sigma}_{ml}^2 \overset{a}{\sim} N(\sigma^2, \frac{2\sigma^4}{N})$. In general, a maximum likelihood estimator satisfies the property of progressive distribution, which indicates

$$\hat{\boldsymbol{\theta}}_{ml} \overset{a}{\sim} N(\boldsymbol{\theta}, \mathbf{I}^{-1}(\boldsymbol{\theta})) \quad (4.76)$$

This chapter presents two novel non-coherent ranging technique by Peak detection. A two-stage approach for the fine ranging estimate is applied to the DFT domain to achieve accurate interpolation and optimum precision. Method description is introduced, following with the algorithm realisation by KPI, which is one of the main works on the thesis. Polynomial interpolation is expounded, including the procedures of processing and the configuration of the parabolic, cubic and quartic functions. Then a general equation for *Kth*-order polynomial fit is derived and given eventually. Another non-coherent ranging technique uses chirp Z transform. The basic concept of Z transform is introduced firstly, following with the algorithm realisation by MLCZT. The CZT accurately implements the periodogram, and only a narrow band spectrum is processed. The concept of most-likelihood estimator is introduced to combine with CZT to acquire better ranging performance.

5. Mathematical derivation of Cramer-Rao Lower Bound of Two Ranging Algorithms

Based on the fundamental theory of statistical signal processing introduced in section 2.5, the vector form of Cramer-Rao lower bound (CRLB) and transformation of parameters is firstly presented. Mathematical expressions of CRLB of Kth-order Polynomial Interpolation (KPI) and Most-likelihood chirp Z transform (MLCZT) algorithms are derived as follow, namely the asymptotical CRLB under the distinctive circumstance and signal-to-noise ratio (SNR) regarding two algorithms respectively. I attempt to put the majority of algebra, mathematical proof and derivation of all parts of the thesis into this signal chapter without deteriorating the readability of the entire thesis.

As mentioned at section 2.5, the concept of minimum variance criterion and minimum variance unbiased (MVU) estimator in statistical signal processing can be widely used, as long as we correspondingly construct suitable models about those interested physical parameters. The physical parameters being estimated here are mainly the range variation and the accumulated signal-to-noise ratio (SNR) for the discussing of the Cramer-Rao Lower Bound (CRLB) of two algorithms.

5.1 Transformation of Parameters and CRLB of Vector Parameters

Since it is common to assume white Gaussian noise, it is worthwhile to derive the CRLB for this case. Consider that a deterministic signal with an unknown parameter ε is estimated in WGN as

$$f[m] = r[m; \varepsilon] + \omega[m] \quad m = 0, 1, \dots, M-1 \quad (5.1)$$

The dependence of the signal on ε is explicitly noted. The likelihood function is

$$p(\mathbf{y}; \varepsilon) = \frac{1}{(2\pi\sigma^2)^{\frac{M}{2}}} \exp\left\{-\frac{1}{2\sigma^2} \sum_{m=0}^{M-1} (f[m] - r[m; \varepsilon])^2\right\} \quad (5.2)$$

Differentiating once produces

$$\frac{\partial \ln p(\mathbf{y}; \varepsilon)}{\partial \varepsilon} = \frac{1}{\sigma^2} \sum_{m=0}^{M-1} (f[m] - r[m; \varepsilon]) \frac{\partial r[m; \varepsilon]}{\partial \varepsilon} \quad (5.3)$$

And a second differentiation results in

$$\frac{\partial^2 \ln p(\mathbf{y}; \varepsilon)}{\partial \varepsilon^2} = \frac{1}{\sigma^2} \sum_{m=0}^{M-1} \left\{ (f[m] - r[m; \varepsilon]) \frac{\partial^2 r[m; \varepsilon]}{\partial \varepsilon^2} - \left(\frac{\partial r[m; \varepsilon]}{\partial \varepsilon} \right)^2 \right\} \quad (5.4)$$

Taking the expected value yields

$$E\left(\frac{\partial^2 \ln p(\mathbf{y}; \varepsilon)}{\partial \varepsilon^2}\right) = \frac{1}{\sigma^2} \sum_{m=0}^{M-1} \left(\frac{\partial r[m; \varepsilon]}{\partial \varepsilon}\right)^2 \quad (5.5)$$

thus finally

$$\text{Var}(\hat{\varepsilon}) \geq \frac{\sigma^2}{\sum_{m=0}^{M-1} \left(\frac{\partial r[m; \varepsilon]}{\partial \varepsilon}\right)^2} \quad (5.6)$$

The form of the bound demonstrates the importance of the signal dependence on ε . Signals that change rapidly as the unknown parameter changes result in accurate estimators.

It frequently occurs in practice that the parameter we wish to estimate is a function of some more fundamental parameter. For example, we may not be interested in the sign of B but instead may wish to estimate B^2 or the power of the signal. Knowing the CRLB for B , we can quickly obtain it for B^2 or in general for any function of B . If it is desired to estimate $\delta = h(\varepsilon)$, then the CRLB is

$$\text{Var}(\hat{\varepsilon}) \geq \frac{\left(\frac{\partial h}{\partial \varepsilon}\right)^2}{-E\left[\frac{\partial^2 \ln p(\mathbf{y}; \varepsilon)}{\partial \varepsilon^2}\right]} \quad (5.7)$$

For the present example, this becomes $\delta = h(\varepsilon) = B^2$ and

$$\text{Var}(\widehat{B^2}) \geq \frac{(2B)^2}{M/\sigma^2} = \frac{4B^2\sigma^2}{M} \quad (5.8)$$

Note that in using (5.7) the CRLB is expressed in terms of ε . Although the sample mean estimator was efficient for B , \bar{y}^2 is not even an unbiased estimator of B^2 . Since $\bar{y} \sim \mathcal{N}(B, \sigma^2/M)$

$$E(\bar{y}^2) = E^2(\bar{y}) + \text{Var}(\bar{y}) = B^2 + \frac{\sigma^2}{M} \neq B^2 \quad (5.9)$$

Hence, it can be concluded that the efficiency of an estimator is destroyed by a non-linear transformation. That it is maintained for affine transformations is easily verified. Although efficiency is preserved only over linear transformations, it is approximately maintained over nonlinear transformations if the data record is large enough. This has great practical significance because we are frequently interested in estimating functions of parameters. As shown in the example above, \bar{y}^2 is biased but asymptotically unbiased (even unbiased as $M \rightarrow \infty$). Intuitively, this situation occurs because of the statistical linearity of the transformation. As M increases, the PDF of \bar{y} becomes

more concentrated about the mean B . Thus, the values of \bar{y} that are observed lie in a small interval, where the nonlinear transformation is approximately linear. Therefore, the transformation may be replaced by a linear one as a value of \bar{y} in the nonlinear region rarely occurs, and the estimator achieves the CRLB asymptotically.

Now extending the results of the previous derivation to the case of a vector parameter $\boldsymbol{\varepsilon} = [\varepsilon_1 \varepsilon_2 \cdots \varepsilon_n]^T$. It is assumed that the estimator $\hat{\boldsymbol{\varepsilon}}$ is unbiased, and the vector parameter CRLB will allow us to place a bound on the variance of each element. The CRLB is found as the $[u, v]$ element of the inverse of a matrix or

$$\text{Var}(\hat{\varepsilon}_u) \geq \left[\mathbf{I}^{-1}(\boldsymbol{\varepsilon}) \right]_{uv} \quad (5.10)$$

where is the $n \times n$ Fisher information matrix. The latter is defined by

$$[\mathbf{I}(\boldsymbol{\varepsilon})]_{uv} = -E \left[\frac{\partial^2 \ln p(\mathbf{y}; \boldsymbol{\varepsilon})}{\partial \varepsilon_u \partial \varepsilon_v} \right] \quad (5.11)$$

for $u = 1, 2, \dots, n; v = 1, 2, \dots, n$.

The scalar parameter form of CRLB has been introduced in section 2.5; now, it is time to present the vector parameter form for further derivation. It is assumed that PDF $p(\mathbf{y}; \boldsymbol{\varepsilon})$ satisfies the regularity conditions

$$E \left[\frac{\partial \ln p(\mathbf{y}; \boldsymbol{\varepsilon})}{\partial \boldsymbol{\varepsilon}} \right] = 0 \quad \text{for all } \boldsymbol{\varepsilon} \quad (5.12)$$

where the expectation is taken concerning $p(\mathbf{y}; \boldsymbol{\varepsilon})$. Then, the covariance matrix of any unbiased estimator $\hat{\boldsymbol{\varepsilon}}$ satisfies

$$\mathbf{C}_{\hat{\boldsymbol{\varepsilon}}} - \mathbf{I}^{-1}(\boldsymbol{\varepsilon}) \geq 0 \quad (5.13)$$

where ≥ 0 is interpreted as meaning that the matrix is positive semidefinite. The Fisher information matrix $\mathbf{I}(\boldsymbol{\varepsilon})$ is presented as

$$[\mathbf{I}(\boldsymbol{\varepsilon})]_{uv} = -E \left[\frac{\partial^2 \ln p(\mathbf{y}; \boldsymbol{\varepsilon})}{\partial \varepsilon_u \partial \varepsilon_v} \right] \quad (5.14)$$

where the derivatives are evaluated at the true value of $\boldsymbol{\varepsilon}$, and the expectation is taken concerning $p(\mathbf{y}; \boldsymbol{\varepsilon})$. Moreover, an unbiased estimator may be found that attains the bound in that $\mathbf{C}_{\hat{\boldsymbol{\varepsilon}}} = \mathbf{I}^{-1}(\boldsymbol{\varepsilon})$ if and only if

$$\frac{\partial \ln p(\mathbf{y}; \boldsymbol{\varepsilon})}{\partial \boldsymbol{\varepsilon}} = \mathbf{I}(\boldsymbol{\varepsilon})(\mathbf{h}(\mathbf{y}) - \boldsymbol{\varepsilon}) \quad (5.15)$$

for some s -dimensional function \mathbf{h} and some $s \times s$ matrix \mathbf{I} . That estimator, which is the MVU estimator, is $\hat{\boldsymbol{\varepsilon}} = \mathbf{h}(\mathbf{y})$, and its covariance matrix is $\mathbf{I}^{-1}(\boldsymbol{\varepsilon})$.

That (5.7) follows from (5.11) is shown by noting that for a positive semidefinite matrix, the diagonal elements are nonnegative. Therefore,

$$[\mathbf{C}_{\hat{\boldsymbol{\varepsilon}}} - \mathbf{I}^{-1}(\boldsymbol{\varepsilon})]_{uv} \geq 0 \quad (5.16)$$

and thus

$$\text{Var}(\hat{\varepsilon}_u) = [\mathbf{C}_{\hat{\boldsymbol{\varepsilon}}}]_{uv} \geq [\mathbf{I}^{-1}(\boldsymbol{\varepsilon})]_{uv} \quad (5.17)$$

Additionally, when equality holds or $\mathbf{C}_{\hat{\boldsymbol{\varepsilon}}} = \mathbf{I}^{-1}(\boldsymbol{\varepsilon})$, then (5.17) holds with equality also. The conditions for the CRLB to be acquired are of particular interest since then $\hat{\boldsymbol{\varepsilon}} = \mathbf{h}(\mathbf{y})$ is efficient and therefore is the MVU estimator.

In finding MVU estimators for a vector parameter, the CRLB theorem presents a powerful assist. It mainly permits us to find the MVU estimator for an essential class of data models. Suffice it to say that if we can model our data in the linear model form, then the MVU estimator and its performance are easily found.

It is natural to extend the expression of transformation to the vector case now. Assume that it is desired to estimate $\boldsymbol{\delta} = \mathbf{h}(\boldsymbol{\varepsilon})$ for \mathbf{h} , an s -dimensional function

$$\mathbf{C}_{\hat{\boldsymbol{\omega}}} - \frac{\partial \mathbf{h}(\boldsymbol{\varepsilon})}{\partial \boldsymbol{\varepsilon}} \mathbf{I}^{-1}(\boldsymbol{\varepsilon}) \frac{\partial \mathbf{h}(\boldsymbol{\varepsilon})^T}{\partial \boldsymbol{\varepsilon}} \geq 0 \quad (5.18)$$

where, as before, ≥ 0 is also to be interpreted as positive semidefinite. In (5.18), $\partial \mathbf{h}(\boldsymbol{\varepsilon})/\partial \boldsymbol{\varepsilon}$ is the $u \times v$ Jacobian matrix defined as

$$\frac{\partial \mathbf{h}(\boldsymbol{\varepsilon})}{\partial \boldsymbol{\varepsilon}} = \begin{bmatrix} \frac{\partial h_1(\boldsymbol{\varepsilon})}{\partial \varepsilon_1} & \frac{\partial h_1(\boldsymbol{\varepsilon})}{\partial \varepsilon_2} & \dots & \frac{\partial h_1(\boldsymbol{\varepsilon})}{\partial \varepsilon_v} \\ \frac{\partial h_2(\boldsymbol{\varepsilon})}{\partial \varepsilon_1} & \frac{\partial h_2(\boldsymbol{\varepsilon})}{\partial \varepsilon_2} & \dots & \frac{\partial h_2(\boldsymbol{\varepsilon})}{\partial \varepsilon_v} \\ \vdots & \vdots & \ddots & \vdots \\ \frac{\partial h_u(\boldsymbol{\varepsilon})}{\partial \varepsilon_1} & \frac{\partial h_u(\boldsymbol{\varepsilon})}{\partial \varepsilon_2} & \dots & \frac{\partial h_u(\boldsymbol{\varepsilon})}{\partial \varepsilon_v} \end{bmatrix} \quad (5.19)$$

5.2 CRLB of K^{th} -order Polynomial Interpolation Algorithm

The CRLB for a vector parameter $\boldsymbol{\omega} = \mathbf{h}(\boldsymbol{\varepsilon})$ is derived firstly from the following application of KPI and MLZCT algorithms. The PDF is characterised by $\boldsymbol{\varepsilon}$. Assuming unbiased estimators as

$$E(\hat{\omega}_u) = \omega_u = [\mathbf{h}(\boldsymbol{\varepsilon})]_u \quad u = 1, 2, \dots, n \quad (5.20)$$

The regularity conditions are

$$E \left[\frac{\partial \ln p(\mathbf{y}; \boldsymbol{\varepsilon})}{\partial \boldsymbol{\varepsilon}} \right] = 0 \quad (5.21)$$

so that

$$\int (\hat{\omega}_u - \omega_u) \frac{\partial \ln p(\mathbf{y}; \boldsymbol{\varepsilon})}{\partial \varepsilon_u} p(\mathbf{y}; \boldsymbol{\varepsilon}) d\mathbf{y} = \frac{\partial [\mathbf{h}(\boldsymbol{\varepsilon})]_u}{\partial \varepsilon_u} \quad (5.22)$$

Now considering for $v \neq u$

$$\begin{aligned} \int (\hat{\omega}_u - \omega_u) \frac{\partial \ln p(\mathbf{y}; \boldsymbol{\varepsilon})}{\partial \varepsilon_u} p(\mathbf{y}; \boldsymbol{\varepsilon}) d\mathbf{y} &= \int (\hat{\omega}_u - \omega_u) \frac{\partial p(\mathbf{y}; \boldsymbol{\varepsilon})}{\partial \varepsilon_u} d\mathbf{y} \\ &= \frac{\partial}{\partial \varepsilon_v} \int \hat{\varepsilon}_u p(\mathbf{y}; \boldsymbol{\varepsilon}) d\mathbf{y} - \omega_u E \left[\frac{\partial \ln p(\mathbf{y}; \boldsymbol{\varepsilon})}{\partial \varepsilon_v} \right] \\ &= \frac{\partial \omega_u}{\partial \varepsilon_v} = \frac{\partial [\mathbf{h}(\boldsymbol{\varepsilon})]_u}{\partial \varepsilon_v} \end{aligned} \quad (5.23)$$

Combining (5.22) and (5.23) into matrix form

$$\int (\hat{\boldsymbol{\omega}} - \boldsymbol{\omega}) \frac{\partial \ln p(\mathbf{y}; \boldsymbol{\varepsilon})}{\partial \boldsymbol{\varepsilon}_u} p(\mathbf{y}; \boldsymbol{\varepsilon}) d\mathbf{y} = \frac{\partial \mathbf{h}(\boldsymbol{\varepsilon})}{\partial \boldsymbol{\varepsilon}} \quad (5.24)$$

Now pre-multiply by \mathbf{a}^T and post-multiply by \mathbf{b} , where \mathbf{a} and \mathbf{b} are arbitrary $s \times 1$ and $t \times 1$ vectors, respectively, to yield

$$\int \mathbf{a}^T (\hat{\boldsymbol{\omega}} - \boldsymbol{\omega}) \frac{\partial \ln p(\mathbf{y}; \boldsymbol{\varepsilon})}{\partial \boldsymbol{\varepsilon}_u} \mathbf{b} p(\mathbf{y}; \boldsymbol{\varepsilon}) d\mathbf{y} = \mathbf{a}^T \frac{\partial \mathbf{h}(\boldsymbol{\varepsilon})}{\partial \boldsymbol{\varepsilon}} \mathbf{b} \quad (5.25)$$

Let

$$q(\mathbf{y}) = p(\mathbf{y}; \boldsymbol{\varepsilon}) \quad (5.26)$$

$$f(\mathbf{y}) = \mathbf{a}^T (\hat{\boldsymbol{\omega}} - \boldsymbol{\omega}) \quad (5.27)$$

$$k(\mathbf{y}) = \frac{\partial \ln p(\mathbf{y}; \boldsymbol{\varepsilon})}{\partial \boldsymbol{\varepsilon}_u} \mathbf{b} \quad (5.28)$$

Now applying the Cauchy-Schwarz inequality

$$\left[\int a(y)b(y)e(y)dy \right]^2 \leq \int a(y)b^2(y)dy \int a(y)e^2(y)dy \quad (5.29)$$

which hold equality if and only if $b(y) = c \cdot e(y)$, for c some constant not dependent on y . The functions b and e are arbitrary scalar functions, while $a(y) \geq 0$ for all y .

$$\begin{aligned} \left(\mathbf{a}^T \frac{\partial \mathbf{h}(\boldsymbol{\varepsilon})}{\partial \boldsymbol{\varepsilon}} \mathbf{b} \right)^2 &\leq \int \mathbf{a}^T (\hat{\boldsymbol{\omega}} - \boldsymbol{\omega}) (\hat{\boldsymbol{\omega}} - \boldsymbol{\omega})^T \mathbf{a} p(\mathbf{y}; \boldsymbol{\varepsilon}) d\mathbf{y} \\ &\cdot \int \mathbf{b}^T \frac{\partial \ln p(\mathbf{y}; \boldsymbol{\varepsilon})}{\partial \boldsymbol{\varepsilon}_u} \frac{\partial \ln p(\mathbf{y}; \boldsymbol{\varepsilon})^T}{\partial \boldsymbol{\varepsilon}_v} \mathbf{b} p(\mathbf{y}; \boldsymbol{\varepsilon}) d\mathbf{y} = \mathbf{a}^T \mathbf{C}_{\hat{\boldsymbol{\omega}}} \mathbf{a} \mathbf{b}^T \mathbf{I}(\boldsymbol{\varepsilon}) \mathbf{b} \end{aligned} \quad (5.30)$$

Since as in the scalar case

$$E \left[\frac{\partial \ln p(\mathbf{y}; \boldsymbol{\varepsilon})}{\partial \boldsymbol{\varepsilon}_u} \frac{\partial \ln p(\mathbf{y}; \boldsymbol{\varepsilon})}{\partial \boldsymbol{\varepsilon}_v} \right] = -E \left[\frac{\partial^2 \ln p(\mathbf{y}; \boldsymbol{\varepsilon})}{\partial \boldsymbol{\varepsilon}_u \partial \boldsymbol{\varepsilon}_v} \right] = [\mathbf{I}(\boldsymbol{\varepsilon})]_{uv} \quad (5.31)$$

Since \mathbf{b} was arbitrary, let

$$\mathbf{b} = \mathbf{I}^{-1}(\boldsymbol{\varepsilon}) \frac{\partial \mathbf{h}(\boldsymbol{\varepsilon})^T}{\partial \boldsymbol{\varepsilon}} \mathbf{a} \quad (5.32)$$

To yield

$$\left(\mathbf{a}^T \frac{\partial \mathbf{h}(\boldsymbol{\varepsilon})}{\partial \boldsymbol{\varepsilon}} \mathbf{I}^{-1}(\boldsymbol{\varepsilon}) \frac{\partial \mathbf{h}(\boldsymbol{\varepsilon})^T}{\partial \boldsymbol{\varepsilon}} \mathbf{a} \right)^2 \leq \mathbf{a}^T \mathbf{C}_{\hat{\boldsymbol{\omega}}} \mathbf{a} \left(\mathbf{a}^T \frac{\partial \mathbf{h}(\boldsymbol{\varepsilon})}{\partial \boldsymbol{\varepsilon}} \mathbf{I}^{-1}(\boldsymbol{\varepsilon}) \frac{\partial \mathbf{h}(\boldsymbol{\varepsilon})^T}{\partial \boldsymbol{\varepsilon}} \mathbf{a} \right) \quad (5.33)$$

Since $\mathbf{I}(\boldsymbol{\varepsilon})$ is the positive definite, so is $\mathbf{I}^{-1}(\boldsymbol{\varepsilon})$, and $\frac{\partial \mathbf{h}(\boldsymbol{\varepsilon})}{\partial \boldsymbol{\varepsilon}} \mathbf{I}^{-1}(\boldsymbol{\varepsilon}) \frac{\partial \mathbf{h}(\boldsymbol{\varepsilon})^T}{\partial \boldsymbol{\varepsilon}}$ is at least positive semidefinite. The term inside the parentheses is therefore nonnegative, and it has

$$\mathbf{a}^T \left(\mathbf{C}_{\hat{\boldsymbol{\omega}}} - \frac{\partial \mathbf{h}(\boldsymbol{\varepsilon})}{\partial \boldsymbol{\varepsilon}} \mathbf{I}^{-1}(\boldsymbol{\varepsilon}) \frac{\partial \mathbf{h}(\boldsymbol{\varepsilon})^T}{\partial \boldsymbol{\varepsilon}} \right) \mathbf{a} \geq 0 \quad (5.34)$$

Because of \mathbf{a} as well as \mathbf{b} are arbitrary, so that (5.30) follows. If $\boldsymbol{\omega} = \mathbf{h}(\boldsymbol{\varepsilon}) = \boldsymbol{\varepsilon}$, then $\frac{\partial \mathbf{h}(\boldsymbol{\varepsilon})}{\partial \boldsymbol{\varepsilon}} = \mathbf{I}$ and (5.24) follows. The conditions for equality are $f(\mathbf{y}) = c \cdot k(\mathbf{y})$, where c is a constant not dependent on y . This condition becomes

$$\mathbf{a}^T (\hat{\boldsymbol{\omega}} - \boldsymbol{\omega}) = c \frac{\partial \ln p(\mathbf{y}; \boldsymbol{\varepsilon})^T}{\partial \boldsymbol{\varepsilon}} \mathbf{b} = c \frac{\partial \ln p(\mathbf{y}; \boldsymbol{\varepsilon})^T}{\partial \boldsymbol{\varepsilon}} \mathbf{I}^{-1}(\boldsymbol{\varepsilon}) \frac{\partial \mathbf{h}(\boldsymbol{\varepsilon})^T}{\partial \boldsymbol{\varepsilon}} \mathbf{a} \quad (5.35)$$

Since \mathbf{a} was arbitrary

$$\frac{\partial \mathbf{h}(\boldsymbol{\varepsilon})}{\partial \boldsymbol{\varepsilon}} \mathbf{I}^{-1}(\boldsymbol{\varepsilon}) \frac{\partial \ln p(\mathbf{y}; \boldsymbol{\varepsilon})}{\partial \boldsymbol{\varepsilon}} = \frac{1}{c} (\hat{\boldsymbol{\omega}} - \boldsymbol{\omega}) \quad (5.36)$$

Consider the case when $\boldsymbol{\omega} = \mathbf{h}(\boldsymbol{\varepsilon}) = \boldsymbol{\varepsilon}$, so that $\frac{\partial \mathbf{h}(\boldsymbol{\varepsilon})}{\partial \boldsymbol{\varepsilon}} = \mathbf{I}$, then

$$\frac{\partial \ln p(\mathbf{y}; \boldsymbol{\varepsilon})}{\partial \boldsymbol{\varepsilon}} = \frac{1}{c} \mathbf{I}(\boldsymbol{\varepsilon})(\hat{\boldsymbol{\varepsilon}} - \boldsymbol{\varepsilon}) \quad (5.37)$$

Note that c may depend on $\boldsymbol{\varepsilon}$, it has

$$\frac{\partial \ln p(\mathbf{y}; \boldsymbol{\varepsilon})}{\partial \varepsilon_u} = \sum_{n=1}^m \frac{[\mathbf{I}(\boldsymbol{\varepsilon})]_{uv}}{c(\boldsymbol{\varepsilon})} (\hat{\varepsilon}_n - \varepsilon_n) \quad (5.38)$$

and differentiating once more

$$\frac{\partial^2 \ln p(\mathbf{y}; \boldsymbol{\varepsilon})}{\partial \varepsilon_u \partial \varepsilon_v} = \sum_{n=1}^m \left(\frac{[\mathbf{I}(\boldsymbol{\varepsilon})]_{un}}{c(\boldsymbol{\varepsilon})} (-\delta_{nu}) + \frac{\partial \left(\frac{[\mathbf{I}(\boldsymbol{\varepsilon})]_{un}}{c(\boldsymbol{\varepsilon})} \right)}{\partial \varepsilon_v} (\hat{\varepsilon}_n - \varepsilon_n) \right) \quad (5.39)$$

Finally, there is

$$[\mathbf{I}(\boldsymbol{\varepsilon})]_{uv} = -E \left[\frac{\partial^2 \ln p(\mathbf{y}; \boldsymbol{\varepsilon})}{\partial \varepsilon_u \partial \varepsilon_v} \right] = \frac{[\mathbf{I}(\boldsymbol{\varepsilon})]_{uv}}{c(\boldsymbol{\varepsilon})} \quad (5.40)$$

since $E(\hat{\omega}_n) = \omega_n$. Clearly, $c(\boldsymbol{\varepsilon}) = 1$ and the condition for equality follows.

Now Deriving the form of KPI of general Gaussian CRLB. Assume that $\mathbf{y} \sim N(\boldsymbol{\eta}(\boldsymbol{\varepsilon}), \mathbf{M}(\boldsymbol{\varepsilon}))$, where $\boldsymbol{\eta}(\boldsymbol{\varepsilon})$ is the $N \times 1$ mean vector and $\mathbf{M}(\boldsymbol{\varepsilon})$ is the $N \times N$ covariance matrix, both of which depend on $\boldsymbol{\varepsilon}$. Then the PDF is

$$p(\mathbf{y}; \boldsymbol{\varepsilon}) = \frac{1}{(2\pi)^{\frac{N}{2}} \det^{\frac{1}{2}}[\mathbf{M}(\boldsymbol{\varepsilon})]} \exp \left[-\frac{1}{2} (\mathbf{y} - \boldsymbol{\eta}(\boldsymbol{\varepsilon}))^T \mathbf{M}^{-1}(\boldsymbol{\varepsilon}) (\mathbf{y} - \boldsymbol{\eta}(\boldsymbol{\varepsilon})) \right] \quad (5.41)$$

we can make use of the following identities

$$\frac{\partial \ln \det[\mathbf{M}(\boldsymbol{\varepsilon})]}{\partial \varepsilon_n} = \text{tr} \left(\mathbf{M}^{-1}(\boldsymbol{\varepsilon}) \frac{\partial \mathbf{M}(\boldsymbol{\varepsilon})}{\partial \varepsilon_n} \right) \quad (5.42)$$

where $\partial \mathbf{M}(\boldsymbol{\varepsilon}) / \partial \varepsilon_n$ is the $N \times N$ matrix with $[u, v]$ element $\partial [\mathbf{M}(\boldsymbol{\varepsilon})]_{uv} / \partial \varepsilon_n$ and

$$\frac{\partial \mathbf{M}^{-1}(\boldsymbol{\varepsilon})}{\partial \varepsilon_n} = -\mathbf{M}^{-1}(\boldsymbol{\varepsilon}) \frac{\partial \mathbf{M}(\boldsymbol{\varepsilon})}{\partial \varepsilon_n} \mathbf{M}^{-1}(\boldsymbol{\varepsilon}) \quad (5.43)$$

To establish (6.42) we first note

$$\frac{\partial \ln \det[\mathbf{M}(\boldsymbol{\varepsilon})]}{\partial \varepsilon_n} = \frac{1}{\det[\mathbf{M}(\boldsymbol{\varepsilon})]} \frac{\partial \det[\mathbf{M}(\boldsymbol{\varepsilon})]}{\partial \varepsilon_n} \quad (5.42)$$

Since $\det[\mathbf{M}(\boldsymbol{\varepsilon})]$ depends on all the elements of $\mathbf{M}(\boldsymbol{\varepsilon})$

$$\begin{aligned} \frac{\partial \det[\mathbf{M}(\boldsymbol{\varepsilon})]}{\partial \varepsilon_n} &= \sum_{u=1}^N \sum_{v=1}^N \frac{\partial \det[\mathbf{M}(\boldsymbol{\varepsilon})]}{\partial [\mathbf{M}(\boldsymbol{\varepsilon})]_{uv}} \frac{\partial [\mathbf{M}(\boldsymbol{\varepsilon})]_{uv}}{\partial \varepsilon_n} \\ &= \text{tr} \left(\frac{\partial \det[\mathbf{M}(\boldsymbol{\varepsilon})]}{\partial \mathbf{M}(\boldsymbol{\varepsilon})} \frac{\partial \mathbf{M}^T(\boldsymbol{\varepsilon})}{\partial \varepsilon_n} \right) \end{aligned} \quad (5.43)$$

where $\partial \det[\mathbf{M}(\boldsymbol{\varepsilon})]/\partial \mathbf{M}(\boldsymbol{\varepsilon})$ is an $N \times N$ matrix with $[u, v]$ element $\partial [\mathbf{M}(\boldsymbol{\varepsilon})]_{uv}/\partial [\mathbf{M}(\boldsymbol{\varepsilon})]_{uv}$ and the identity

$$\text{tr}(\mathbf{A}\mathbf{B}^T) = \sum_{u=1}^N \sum_{v=1}^N [\mathbf{A}]_{uv} [\mathbf{B}]_{uv} \quad (5.44)$$

has been used. Now by the definition of the determinant

$$\det[\mathbf{M}(\boldsymbol{\varepsilon})] = \sum_{u=1}^N [\mathbf{M}(\boldsymbol{\varepsilon})]_{uv} [\mathbf{L}]_{uv} \quad (5.45)$$

where \mathbf{L} is the $N \times N$ cofactor matrix and v can take any value from 1 to N . Thus,

$$\frac{\partial \det[\mathbf{M}(\boldsymbol{\varepsilon})]}{\partial [\mathbf{M}(\boldsymbol{\varepsilon})]_{uv}} = [\mathbf{L}]_{uv} \quad (6.45)$$

or

$$\frac{\partial \det[\mathbf{M}(\boldsymbol{\varepsilon})]}{\partial \mathbf{M}(\boldsymbol{\varepsilon})} = \mathbf{L} \quad (5.46)$$

It is well known, however, that

$$\mathbf{M}^{-1}(\boldsymbol{\varepsilon}) = \frac{\mathbf{L}^T}{\det[\mathbf{M}(\boldsymbol{\varepsilon})]} \quad (5.46)$$

so that

$$\frac{\partial \det[\mathbf{M}(\boldsymbol{\varepsilon})]}{\partial \mathbf{M}(\boldsymbol{\varepsilon})} = \mathbf{M}^{-1}(\boldsymbol{\varepsilon}) \det[\mathbf{M}(\boldsymbol{\varepsilon})] \quad (5.47)$$

Using this in (5.42) and (5.43), we have the desired result as follow

$$\begin{aligned} \frac{\partial \ln \det[\mathbf{M}(\boldsymbol{\varepsilon})]}{\partial \varepsilon_n} &= \frac{1}{\det[\mathbf{M}(\boldsymbol{\varepsilon})]} \text{tr} \left(\mathbf{M}^{-1}(\boldsymbol{\varepsilon}) \det[\mathbf{M}(\boldsymbol{\varepsilon})] \frac{\partial \mathbf{M}(\boldsymbol{\varepsilon})}{\partial \varepsilon_n} \right) \\ &= \text{tr} \left(\mathbf{M}^{-1}(\boldsymbol{\varepsilon}) \frac{\partial \mathbf{M}(\boldsymbol{\varepsilon})}{\partial \varepsilon_n} \right) \end{aligned} \quad (5.48)$$

The second identity (5.43) is easily established as follows. Consider

$$\mathbf{M}^{-1}(\boldsymbol{\varepsilon}) \mathbf{M}(\boldsymbol{\varepsilon}) = \mathbf{I} \quad (5.49)$$

Differentiating each element of the matrices and expressing in the matrix form, we have

$$\mathbf{M}^{-1}(\boldsymbol{\varepsilon}) \frac{\partial \mathbf{M}(\boldsymbol{\varepsilon})}{\partial \varepsilon_n} + \frac{\partial \mathbf{M}^{-1}(\boldsymbol{\varepsilon})}{\partial \varepsilon_n} \mathbf{M}(\boldsymbol{\varepsilon}) = \mathbf{0} \quad (5.50)$$

which leads to the desired result.

It is time to evaluate the CRLB. Taking the first derivation

$$\frac{\partial \ln p(\mathbf{y}; \boldsymbol{\varepsilon})}{\partial \varepsilon_n} = -\frac{1}{2} \frac{\partial \ln \det[\mathbf{M}(\boldsymbol{\varepsilon})]}{\partial \varepsilon_n} - \frac{1}{2} \frac{\partial}{\partial \varepsilon_n} \left[(\mathbf{y} - \boldsymbol{\eta}(\boldsymbol{\varepsilon}))^T \mathbf{M}^{-1}(\boldsymbol{\varepsilon}) (\mathbf{y} - \boldsymbol{\eta}(\boldsymbol{\varepsilon})) \right] \quad (5.51)$$

The first term has already been evaluated using (5.48); therefore, now consider the second term:

$$\begin{aligned} & \frac{\partial}{\partial \varepsilon_n} \left[(\mathbf{y} - \boldsymbol{\eta}(\boldsymbol{\varepsilon}))^T \mathbf{M}^{-1}(\boldsymbol{\varepsilon}) (\mathbf{y} - \boldsymbol{\eta}(\boldsymbol{\varepsilon})) \right] \\ &= \frac{\partial}{\partial \varepsilon_n} \sum_{u=1}^N \sum_{v=1}^N (y[u] - [\boldsymbol{\eta}(\boldsymbol{\varepsilon})]_u) [\mathbf{M}^{-1}(\boldsymbol{\varepsilon})]_{uv} (y[v] - [\boldsymbol{\eta}(\boldsymbol{\varepsilon})]_v) \\ &= \sum_{u=1}^N \sum_{v=1}^N \{ (y[u] - [\boldsymbol{\eta}(\boldsymbol{\varepsilon})]_u) [[\mathbf{M}^{-1}(\boldsymbol{\varepsilon})]_{uv} \left(\frac{\partial [\boldsymbol{\eta}(\boldsymbol{\varepsilon})]_v}{\partial \varepsilon_n} \right) \right. \\ & \quad \left. + \frac{\partial [\mathbf{M}^{-1}(\boldsymbol{\varepsilon})]_{uv}}{\partial \varepsilon_n} (y[v] - [\boldsymbol{\eta}(\boldsymbol{\varepsilon})]_v) \right. \\ & \quad \left. + \left(-\frac{\partial [\boldsymbol{\eta}(\boldsymbol{\varepsilon})]_u}{\partial \varepsilon_n} \right) [\mathbf{M}^{-1}(\boldsymbol{\varepsilon})]_{uv} (y[v] - [\boldsymbol{\eta}(\boldsymbol{\varepsilon})]_v) \right\} \\ &= -(\mathbf{y} - \boldsymbol{\eta}(\boldsymbol{\varepsilon}))^T \mathbf{M}^{-1}(\boldsymbol{\varepsilon}) \frac{\partial \boldsymbol{\eta}(\boldsymbol{\varepsilon})}{\partial \varepsilon_n} + (\mathbf{y} - \boldsymbol{\eta}(\boldsymbol{\varepsilon}))^T \frac{\partial \mathbf{M}^{-1}(\boldsymbol{\varepsilon})}{\partial \varepsilon_n} (\mathbf{y} - \boldsymbol{\eta}(\boldsymbol{\varepsilon})) \\ & \quad - \frac{\partial \boldsymbol{\eta}(\boldsymbol{\varepsilon})^T}{\partial \varepsilon_n} \mathbf{M}^{-1}(\boldsymbol{\varepsilon}) (\mathbf{y} - \boldsymbol{\eta}(\boldsymbol{\varepsilon})) \\ &= -2 \frac{\partial \boldsymbol{\eta}(\boldsymbol{\varepsilon})^T}{\partial \varepsilon_n} \mathbf{M}^{-1}(\boldsymbol{\varepsilon}) (\mathbf{y} - \boldsymbol{\eta}(\boldsymbol{\varepsilon})) + (\mathbf{y} - \boldsymbol{\eta}(\boldsymbol{\varepsilon}))^T \frac{\partial \mathbf{M}^{-1}(\boldsymbol{\varepsilon})}{\partial \varepsilon_n} (\mathbf{y} - \boldsymbol{\eta}(\boldsymbol{\varepsilon})) \end{aligned} \quad (5.52)$$

Using (5.42) and the previous result, there is

$$\begin{aligned} \frac{\partial \ln p(\mathbf{y}; \boldsymbol{\varepsilon})}{\partial \varepsilon_n} &= -\frac{1}{2} \text{tr} \left(\mathbf{M}^{-1}(\boldsymbol{\varepsilon}) \frac{\partial \mathbf{M}(\boldsymbol{\varepsilon})}{\partial \varepsilon_n} \right) + \frac{\partial \boldsymbol{\eta}(\boldsymbol{\varepsilon})^T}{\partial \varepsilon_n} \mathbf{M}^{-1}(\boldsymbol{\varepsilon}) (\mathbf{y} - \boldsymbol{\eta}(\boldsymbol{\varepsilon})) \\ & \quad - \frac{1}{2} (\mathbf{y} - \boldsymbol{\eta}(\boldsymbol{\varepsilon}))^T \frac{\partial \mathbf{M}^{-1}(\boldsymbol{\varepsilon})}{\partial \varepsilon_n} (\mathbf{y} - \boldsymbol{\eta}(\boldsymbol{\varepsilon})) \end{aligned} \quad (5.53)$$

Let $\mathbf{y} = \mathbf{x} - \boldsymbol{\eta}(\boldsymbol{\varepsilon})$. Evaluating

$$[\mathbf{I}(\boldsymbol{\varepsilon})]_{nl} = E \left[\frac{\partial \ln p(\mathbf{y}; \boldsymbol{\varepsilon})}{\partial \varepsilon_n} \frac{\partial \ln p(\mathbf{y}; \boldsymbol{\varepsilon})}{\partial \varepsilon_l} \right] \quad (5.54)$$

which is equivalent to (5.46), yields

$$\begin{aligned} [\mathbf{I}(\boldsymbol{\varepsilon})]_{nl} &= \frac{1}{4} \text{tr} \left(\mathbf{M}^{-1}(\boldsymbol{\varepsilon}) \frac{\partial \mathbf{M}(\boldsymbol{\varepsilon})}{\partial \varepsilon_n} \right) \text{tr} \left(\mathbf{M}^{-1}(\boldsymbol{\varepsilon}) \frac{\partial \mathbf{M}(\boldsymbol{\varepsilon})}{\partial \varepsilon_l} \right) \\ &+ \frac{1}{2} \text{tr} \left(\mathbf{M}^{-1}(\boldsymbol{\varepsilon}) \frac{\partial \mathbf{M}(\boldsymbol{\varepsilon})}{\partial \varepsilon_n} \right) E \left(\mathbf{x}^T \frac{\partial \mathbf{M}^{-1}(\boldsymbol{\varepsilon})}{\partial \varepsilon_l} \mathbf{x} \right) \\ &+ \frac{\partial \boldsymbol{\eta}(\boldsymbol{\varepsilon})^T}{\partial \varepsilon_n} \mathbf{M}^{-1}(\boldsymbol{\varepsilon}) E[\mathbf{x}\mathbf{x}^T] \mathbf{M}^{-1}(\boldsymbol{\varepsilon}) \frac{\partial \boldsymbol{\eta}(\boldsymbol{\varepsilon})}{\partial \varepsilon_l} \\ &+ \frac{1}{4} E \left[\mathbf{x}^T \frac{\partial \mathbf{M}^{-1}(\boldsymbol{\varepsilon})}{\partial \varepsilon_n} \mathbf{x}\mathbf{x}^T \frac{\partial \mathbf{M}^{-1}(\boldsymbol{\varepsilon})}{\partial \varepsilon_l} \mathbf{x} \right] \end{aligned} \quad (5.55)$$

where we note that all odd-order moments are zero. Continuing, there is

$$\begin{aligned} [\mathbf{I}(\boldsymbol{\varepsilon})]_{nl} &= \frac{1}{4} \text{tr} \left(\mathbf{M}^{-1}(\boldsymbol{\varepsilon}) \frac{\partial \mathbf{M}(\boldsymbol{\varepsilon})}{\partial \varepsilon_n} \right) \text{tr} \left(\mathbf{M}^{-1}(\boldsymbol{\varepsilon}) \frac{\partial \mathbf{M}(\boldsymbol{\varepsilon})}{\partial \varepsilon_l} \right) \\ &- \frac{1}{2} \text{tr} \left(\mathbf{M}^{-1}(\boldsymbol{\varepsilon}) \frac{\partial \mathbf{M}(\boldsymbol{\varepsilon})}{\partial \varepsilon_n} \right) \text{tr} \left(\mathbf{M}^{-1}(\boldsymbol{\varepsilon}) \frac{\partial \mathbf{M}(\boldsymbol{\varepsilon})}{\partial \varepsilon_l} \right) \\ &+ \frac{\partial \boldsymbol{\eta}(\boldsymbol{\varepsilon})^T}{\partial \varepsilon_n} \mathbf{M}^{-1}(\boldsymbol{\varepsilon}) \frac{\partial \boldsymbol{\eta}(\boldsymbol{\varepsilon})}{\partial \varepsilon_l} + \frac{1}{4} E \left[\mathbf{x}^T \frac{\partial \mathbf{M}^{-1}(\boldsymbol{\varepsilon})}{\partial \varepsilon_n} \mathbf{x}\mathbf{x}^T \frac{\partial \mathbf{M}^{-1}(\boldsymbol{\varepsilon})}{\partial \varepsilon_l} \mathbf{x} \right] \end{aligned} \quad (5.56)$$

where $E(\mathbf{x}^T \mathbf{z}) = \text{tr}[E(\mathbf{z}\mathbf{x}^T)]$ for \mathbf{x} , \mathbf{z} $N \times 1$ vectors and (6.43) have been used. To evaluate the last term, the following equation is introduced

$$E(\mathbf{x}^T \mathbf{A}\mathbf{x}\mathbf{x}^T \mathbf{B}\mathbf{x}) = \text{tr}(\mathbf{A}\mathbf{C})\text{tr}(\mathbf{B}\mathbf{C}) + 2\text{tr}(\mathbf{A}\mathbf{C}\mathbf{B}\mathbf{C}) \quad (5.57)$$

where $\mathbf{M} = E(\mathbf{x}^T \mathbf{x})$ and \mathbf{A} and \mathbf{B} are symmetric matrices. Thus, this term becomes

$$\begin{aligned} &\frac{1}{4} \text{tr} \left(\frac{\partial \mathbf{M}^{-1}(\boldsymbol{\varepsilon})}{\partial \varepsilon_n} \mathbf{M}(\boldsymbol{\varepsilon}) \right) \text{tr} \left(\frac{\partial \mathbf{M}^{-1}(\boldsymbol{\varepsilon})}{\partial \varepsilon_l} \mathbf{M}(\boldsymbol{\varepsilon}) \right) \\ &+ \frac{1}{2} \text{tr} \left(\frac{\partial \mathbf{M}^{-1}(\boldsymbol{\varepsilon})}{\partial \varepsilon_n} \mathbf{M}(\boldsymbol{\varepsilon}) \frac{\partial \mathbf{M}^{-1}(\boldsymbol{\varepsilon})}{\partial \varepsilon_l} \mathbf{M}(\boldsymbol{\varepsilon}) \right) \end{aligned} \quad (5.58)$$

Next, using the relationship (5.43), this term becomes

$$\frac{1}{4} \text{tr} \left(\mathbf{M}^{-1}(\boldsymbol{\varepsilon}) \frac{\partial \mathbf{M}(\boldsymbol{\varepsilon})}{\partial \varepsilon_n} \right) \text{tr} \left(\mathbf{M}^{-1}(\boldsymbol{\varepsilon}) \frac{\partial \mathbf{M}(\boldsymbol{\varepsilon})}{\partial \varepsilon_l} \right) \quad (5.59)$$

$$+ \frac{1}{2} \text{tr} \left(\mathbf{M}^{-1}(\boldsymbol{\varepsilon}) \frac{\partial \mathbf{M}(\boldsymbol{\varepsilon})}{\partial \varepsilon_n} \mathbf{M}^{-1}(\boldsymbol{\varepsilon}) \frac{\partial \mathbf{M}(\boldsymbol{\varepsilon})}{\partial \varepsilon_l} \right)$$

And finally, using (5.59) in (5.56) produces the desired result.

According to the processing techniques derived above, the mathematical expression will be directly given to save pages for long derivation again. the CRLB of Kth-order polynomial interpolation (KPI) algorithm can be presented as

$$CRLB(\hat{p}_k) = \frac{\lambda_e^2}{64\pi^2 SNR_k T_A^{2k}} \sum_{n=1}^k (2k-1) \cdot \left[\sum_{m=0}^{2(n-k)} \frac{(-1)^m}{2^{2m+1}} \binom{k}{n} \binom{k}{m} \frac{(2n-2m)!}{m!(n-m)!(n-k-2m)!} \right]^2 \quad (5.60)$$

where $SNR_k = kA^2/\sigma^2$ is the accumulated signal-to-noise ratio (SNR), $\gamma = t_0/T_A$ is the normalised index for the benchmark time t_0 and accumulated reference T_A , and λ_e is the equivalent waveform.

5.3 CRLB of Most-likelihood Chirp Z Transform Algorithm

Under specific circumstances, it is hard to calculate the CRLB as it is required to invert the covariance matrix. Asymptotical CRLB can be applied as an alternative to Gaussian processes, which is easily computed and provides sufficient information because of its simplified form. The primary negative is that it is valid only as of the data record length $M \rightarrow \infty$ or asymptotically. However, it can provide a desirable approximation to the identical CRLB if M is substantially larger than the correlation time of the pro, which refers to the maximum lag i of the ACF $c_y(i) = E[y[m]y[m+i]]$ for which the ACF is essentially nonzero. Therefore, for processes with broad PSDs, the approximation will be good for moderate length data records, while for narrowband processes, longer length data records are required. The elements of the Fisher information are therefore approximately ($M \rightarrow \infty$)

$$[\mathbf{I}(\boldsymbol{\varepsilon})]_{uv} = \frac{M}{2} \int_{-\frac{1}{2}}^{\frac{1}{2}} \frac{\partial \ln P_y(h; \boldsymbol{\varepsilon})}{\partial \varepsilon_u} \frac{\partial \ln P_y(h; \boldsymbol{\varepsilon})}{\partial \varepsilon_v} dh \quad (5.61)$$

where $P_y(h; \boldsymbol{\varepsilon})$ is the PSD of the process with the explicit dependence on $\boldsymbol{\varepsilon}$ shown. It is assumed that the mean of $y[m]$ is zero. This form allows us to examine the accuracy with which PSD, or equivalently, covariance parameters may be estimated.

It can be proven that almost any WSS Gaussian random processing $y[m]$ maybe represented as the output of a causal linear invariant filter driven at the input by white Gaussian noise $n[m]$ or

$$y[m] = \sum_{i=0}^{\infty} g[i]n[m-i] \quad (5.62)$$

where $g[0] = 1$. The only condition is that the PSD must satisfy

$$\int_{-\frac{1}{2}}^{\frac{1}{2}} \ln P_y(h) dh > -\infty \quad (5.63)$$

With this representation the PSD of $y[m]$ is

$$P_y(h) = |G(h)|^2 \sigma_n^2 \quad (5.64)$$

since σ_n^2 is the variance of $n[m]$ and

$$G(h) = \sum_{i=0}^{\infty} g[i] \exp(-j2\pi hi) \quad (5.65)$$

is the filter frequency response. If the observation is $\{y[0], y[1], \dots, y[m-1]\}$ and M is large; then the representation is approximated by

$$\begin{aligned} y[m] &= \sum_{i=0}^m g[j]n[m-i] + y[m] + \sum_{i=m+1}^{\infty} g[j]n[m-i] \\ &\approx \sum_{i=0}^m g[j]n[m-i] \end{aligned} \quad (5.66)$$

This is equivalent to setting $n[m] = 0$ for $m < 0$. As $m \rightarrow \infty$, the approximate representation becomes better for $y[m]$. It is clear, however, that the beginning samples will be poorly represented unless the impulse response $g[i]$ is small for $i > m$. For large M , most of the samples will be accurately represented if M is much greater than the impulse response length. Since

$$c_y[i] = \sigma_n^2 \sum_{m=0}^{\infty} g[m]g[m+i] \quad (5.67)$$

the correlation time of $c_y[i]$ is the same as the impulse response length. Hence, because the CRLB to be derived is based on (5.66), the asymptotic CRLB will be a good approximation if the data record length is much greater than the correlation time.

To find the PDF of y we used (5.62), which is a transformation from $\mathbf{n} = [n[0] n[1] \dots n[M-1]]^T$ to $\mathbf{y} = [y[0] y[1] \dots y[M-1]]^T$ or

$$\mathbf{y} = \begin{bmatrix} g[0] & 0 & 0 & \cdots & 0 \\ g[1] & g[0] & 0 & \cdots & 0 \\ \vdots & \vdots & \vdots & \ddots & \vdots \\ g[M-1] & g[M-2] & g[M-3] & \cdots & g[0] \end{bmatrix} \mathbf{n} \quad (5.68)$$

Note that \mathbf{G} has a determinant of $(g[0])^M = 1$ and hence is invertible. Since $\mathbf{n} \sim N(\mathbf{0}, \sigma_n^2 \mathbf{I})$, the PDF of \mathbf{y} is $N(\mathbf{0}, \sigma_n^2 \mathbf{G}\mathbf{G}^T)$ or

$$p(\mathbf{y}; \boldsymbol{\varepsilon}) = \frac{1}{(2\pi)^{\frac{M}{2}} \det^{\frac{1}{2}}(\sigma_n^2 \mathbf{G}\mathbf{G}^T)} \exp\left[-\frac{1}{2} \mathbf{y}^T (\sigma_n^2 \mathbf{G}\mathbf{G}^T)^{-1} \mathbf{y}\right] \quad (5.69)$$

while

$$\det(\sigma_n^2 \mathbf{G}\mathbf{G}^T) = \sigma_n^{2M} \det^2(\mathbf{G}) = \sigma_n^{2M} \quad (5.70)$$

also,

$$\mathbf{y}^T (\sigma_n^2 \mathbf{G}\mathbf{G}^T)^{-1} \mathbf{y} = \frac{1}{\sigma_n^2} (\mathbf{G}^{-1} \mathbf{y})^T (\mathbf{G}^{-1} \mathbf{y}) = \frac{1}{\sigma_n^2} \mathbf{N}^T \mathbf{N} \quad (5.71)$$

So that

$$p(\mathbf{y}; \boldsymbol{\varepsilon}) = \frac{1}{(2\pi\sigma_n^2)^{\frac{M}{2}}} \exp\left(-\frac{1}{2\sigma_n^2} \mathbf{N}^T \mathbf{N}\right) \quad (5.72)$$

from (5.66) it has approximately

$$Y(h) = G(h)N(h) \quad (5.73)$$

where

$$Y(h) = \sum_{m=0}^{M-1} y[m] \exp(-j2\pi hm) \quad (5.74)$$

$$N(h) = \sum_{m=0}^{M-1} n[m] \exp(-j2\pi hm)$$

are the Fourier transforms of the truncated sequences. By Parseval's theorem

$$\begin{aligned} \frac{1}{\sigma_n^2} \mathbf{N}^T \mathbf{N} &= \frac{1}{\sigma_n^2} \sum_{m=0}^{M-1} n^2[m] = \frac{1}{\sigma_n^2} \int_{-\frac{1}{2}}^{\frac{1}{2}} |N(h)|^2 dh \\ &\approx \int_{-\frac{1}{2}}^{\frac{1}{2}} \frac{|Y(h)|^2}{\sigma_n^2 |G(h)|^2} dh = \int_{-\frac{1}{2}}^{\frac{1}{2}} \frac{|Y(h)|^2}{P_y(h)} dh \end{aligned} \quad (5.75)$$

Also,

$$\begin{aligned}
\ln\sigma_n^2 &= \int_{-\frac{1}{2}}^{\frac{1}{2}} \sigma_n^2 dh = \int_{-\frac{1}{2}}^{\frac{1}{2}} \ln\left(\frac{P_y(h)}{|G(h)|^2}\right) dh \\
&= \int_{-\frac{1}{2}}^{\frac{1}{2}} \ln P_y(h) dh - \int_{-\frac{1}{2}}^{\frac{1}{2}} \ln |G(h)|^2 dh
\end{aligned} \tag{5.76}$$

while

$$\begin{aligned}
\int_{-\frac{1}{2}}^{\frac{1}{2}} \ln |G(h)|^2 dh &= \int_{-\frac{1}{2}}^{\frac{1}{2}} \ln G(h) + \ln G^*(h) dh = 2\operatorname{Re} \int_{-\frac{1}{2}}^{\frac{1}{2}} \ln G(h) dh \\
&= 2\operatorname{Re} \oint_C \ln G(z) \frac{dz}{2\pi j z} = 2\operatorname{Re} [Z^{-1}\{\ln G(z)\}|_{m=0}]
\end{aligned} \tag{5.77}$$

where C is the unit circle in the z plane. Since $G(z)$ corresponds to the system function of a causal filter, it converges outside a circle of radius $r < 1$; since $G(z)$ is assumed to exist on the unit circle for the frequency response to exist. Hence, $\ln G(z)$ also converges outside a circle of radius $r < 1$, so that the corresponding sequence is causal. By the initial value theorem which is valid for causal sequence

$$Z^{-1}\{\ln G(z)\}|_{m=0} = \lim_{z \rightarrow \infty} \ln G(z) = \ln \lim_{z \rightarrow \infty} G(z) = \ln g[0] = 0 \tag{5.78}$$

Therefore

$$\int_{-\frac{1}{2}}^{\frac{1}{2}} \ln |G(h)|^2 dh = 0 \tag{5.79}$$

then

$$\ln\sigma_n^2 = \int_{-\frac{1}{2}}^{\frac{1}{2}} \ln P_y(h) dh \tag{5.80}$$

Substituting (5.75) and (5.80) into (5.69) produces for the log PDF

$$\ln p(\mathbf{y}; \boldsymbol{\varepsilon}) = -\frac{M}{2} \ln 2\pi - \frac{M}{2} \int_{-\frac{1}{2}}^{\frac{1}{2}} \ln P_y(h) dh - \frac{1}{2} \int_{-\frac{1}{2}}^{\frac{1}{2}} \frac{|Y(h)|^2}{P_y(h)} dh \tag{5.81}$$

Hence, the asymptotic log PDF is

$$\ln p(\mathbf{y}; \boldsymbol{\varepsilon}) = -\frac{M}{2} \ln 2\pi - \frac{M}{2} \int_{-\frac{1}{2}}^{\frac{1}{2}} \left[\ln P_y(h) + \frac{1}{M} \frac{|Y(h)|^2}{P_y(h)} \right] dh \quad (5.82)$$

To determine the CRLB

$$\begin{aligned} \frac{\partial \ln p(\mathbf{y}; \boldsymbol{\varepsilon})}{\partial \varepsilon_u} &= -\frac{M}{2} \int_{-\frac{1}{2}}^{\frac{1}{2}} \left(\frac{1}{P_y(h)} - \frac{1}{M} \frac{|Y(h)|^2}{P_y^2(h)} \right) \frac{\partial P_y(h)}{\partial \varepsilon_u} dh \\ \frac{\partial^2 \ln p(\mathbf{y}; \boldsymbol{\varepsilon})}{\partial \varepsilon_u \partial \varepsilon_v} &= -\frac{M}{2} \int_{-\frac{1}{2}}^{\frac{1}{2}} \left(\frac{1}{P_y(h)} - \frac{1}{M} \frac{|Y(h)|^2}{P_y^2(h)} \right) \frac{\partial^2 P_y(h)}{\partial \varepsilon_u \partial \varepsilon_v} \\ &\quad + \left(-\frac{1}{P_y^2(h)} - \frac{2}{M} \frac{|Y(h)|^2}{P_y^3(h)} \right) \frac{\partial P_y(h)}{\partial \varepsilon_u} \frac{\partial P_y(h)}{\partial \varepsilon_v} dh \end{aligned} \quad (5.83)$$

In taking the expected value, we encounter the term $E[|Y(h)|^2/M]$, for large M this is now shown to be $P_y(h)$. Note that $|Y(h)|^2/M$ is termed the periodogram spectral estimator.

$$\begin{aligned} E\left(\frac{1}{M} |Y(h)|^2\right) &= E\left(\frac{1}{M} \sum_{n=0}^{M-1} \sum_{m=0}^{M-1} y[n]y[m] \exp[-j2\pi h(n-m)]\right) \\ &= \frac{1}{M} \sum_{n=0}^{M-1} \sum_{m=0}^{M-1} c_y[n-m] \exp[-j2\pi h(n-m)] \\ &= \sum_{i=-(M-1)}^{M-1} \left(1 - \frac{|i|}{M}\right) c_y[i] \exp[-j2\pi hi] \end{aligned} \quad (5.84)$$

where we have used the identity

$$\sum_{n=0}^{M-1} \sum_{m=0}^{M-1} k[n-m] = \sum_{i=-(M-1)}^{M-1} (M - |i|) k[i] \quad (5.85)$$

As $M \rightarrow \infty$,

$$\left(1 - \frac{|i|}{M}\right) c_y[i] \rightarrow c_y[i] \quad (5.86)$$

Assuming that the ACF dies out sufficiently rapidly. Therefore,

$$E\left(\frac{1}{M} |Y(h)|^2\right) \approx P_y(h) \quad (5.87)$$

After taking expectations in (5.81), this first section is zero, thus,

$$[I(\boldsymbol{\varepsilon})]_{uv} = \frac{M}{2} \int_{-\frac{1}{2}}^{\frac{1}{2}} \frac{1}{P_y^2(h)} \frac{\partial P_y(h)}{\partial \varepsilon_u} \frac{\partial P_y(h)}{\partial \varepsilon_v} dh = \frac{M}{2} \int_{-\frac{1}{2}}^{\frac{1}{2}} \frac{\partial \ln P_y(h)}{\partial \varepsilon_u} \frac{\partial \ln P_y(h)}{\partial \varepsilon_v} dh \quad (5.88)$$

which is (5.75) without the explicit dependence of the PSD on $\boldsymbol{\varepsilon}$ shown.

According to the processing techniques derived above, the CRLB of K points most-likelihood chirp Z transform (MLCZT) algorithm can be presented as

$$CRLB(\hat{p}_k) = \frac{\lambda_e^2}{16\pi^2 SNR_k T_A^{2k}} \frac{(k!)^2}{2k+1} \cdot \left[\sum_{m=0}^{2(n-k)} \frac{(-1)^m}{2m-1} \binom{k}{m} (m+1) \right]^2 \quad (5.89)$$

where $SNR_k = kA^2/\sigma^2$ is the accumulated signal-to-noise ratio (SNR), $\gamma = t_0/T_A$ is the normalised index for the benchmark time t_0 and accumulated reference T_A , and λ_e is the equivalent waveform.

Mathematical expressions of CRLB of KPI and MLCZT algorithms are derived in this chapter. It contains the majority of mathematical proofing and derivation of all parts of the thesis. The vector form of CRLB is firstly introduced, then the derivation of asymptotical CRLB under the distinctive circumstance and SNR regarding two techniques, respectively. A mathematical derivation is also presented to validate the most-likelihood method in the CZT at the end of this chapter.

6. Simulation Results and Analysis

This chapter analyses the results and data obtained with simulations and laboratory experiments as well, beginning with pre-processing the acquired raw time-domain data, then following the results of K -order polynomial interpolation (KPI) and most-likelihood chirp Z transform (MLCZT) techniques. Relative drawbacks and improvements are discussed from several aspects under different conditions. A variety of simulation outcomes based on non-coherent technique are demonstrated in the following sections.

6.1 Results of Peak Detection by K^{th} -order Polynomial Interpolation

The pre-processing and processing results of quadratic, cubic and quartic interpolators by Matlab are presented, as well as the estimation error under conditions of different zero-padding factor p .

6.1.1 Pre-processing of Zero-padding

It is desirable to pre-process signal data by zero-padding. Zero-padding refers to adding zeros to the end of a time-domain signal. It can enhance the FFT resolution of a time-domain signal, rather than merely increase the length of the given sequence. At the same time, zero-padding cannot improve the spectral resolution (the minimum fraction between two frequencies that can be distinguished).

In early applications, zero-padding is introduced to fill the data points N so that the radix-2 FFT algorithm (N is required to a power of 2) can be applied directly to the original data sequence. Zero-padding is also useful when the frequency sample of the given signal is too sparse to give a good enough resolution of the continuous-frequency estimated spectrum. It may reveal more delicate details in the spectrum through implementing the FFT to the signal sequence after zero-padding. Since the estimation of continuous-frequency spectral is the same for both the original signal data and the zero-padding sequence, zero-padding cannot enhance the spectral resolution of the periodogram method for sure [35].

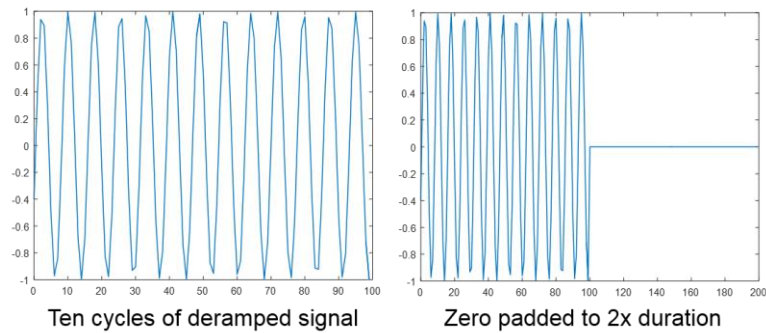


Figure 6.1 Deramped signal and zero-padding

As shown in Figure. 6.1, the left figure is the ten cycles of the deramped signal, corresponding range $10(c/2B)$. The term Padding factor p can be introduced to describe the numbers of zero added to the signal sequence. $p = 1$ represents that no extra zero is added to the current signal data; $p = 2$ represents that the numbers of added zero are as many as the original signal data; $p = 4$ represents that the numbers added zero are tripled than the original data points, etc.

6.1.2 Results of Quadratic Interpolation

As discussed previously, a DFT sample will not present identically on the peak of asinc function. Therefore, the magnitude of the DFT sample accounts for detection, but its frequency is approximate to the actual location of the asinc peak. That is to say, the range can be estimated from the shape of the discrete peak, for comparison with the measured range from the FFT, to derive the difference (error range) for calibration. Polynomial fit is used to the several points closest to the peak to find and locate the position of the peak relative to the central point.

In terms of figures of section 6.1.2, X axis represents the estimated peak position using polynomial interpolation technique, and the unit is range bin; Y axis represents the actual peak position with the unit of both range bin and millimetre. The target is discrete point scatter and the SNR is set to 20 dB; simulation parameters of polynomial interpolation are presented to the Table 6.1. The principle factors of radar system constructed during the simulation environment can be found below. Note that all the simulation results of polynomial interpolation technique shown in this chapter operate on the identical parameters if there is no other special explanation.

Table 6.1 Simulation Parameters of Polynomial Interpolation

Carrier frequency f_c	300 MHz
Sweep bandwidth B	200MHz
Pulse duration T	1 s
Pulse interval	1.6384 s
Chirp phase offset	0
ADC sample interval	4×10^{-6} s
ADC Sampling rate	250 kHz
Medium dielectric constant	$\epsilon_r = 1.2$

Figure 6.2 illustrates the estimation performance of the quadratic interpolation when the zero-padding factor $p = 2$. As the figure shows, estimated peak positions fluctuate around the actual peak position. The interpolated range estimation is best when the actual range is either very close to a sample range or exactly halfway (± 0.25 here due to zero-padding factor $p = 2$) between two sample ranges. At the same time, the worst-case error of 0.018 bins (13.5 millimetres when bandwidth = 200 MHz) occurs when the actual peak is 0.016 bins away from a sample range.

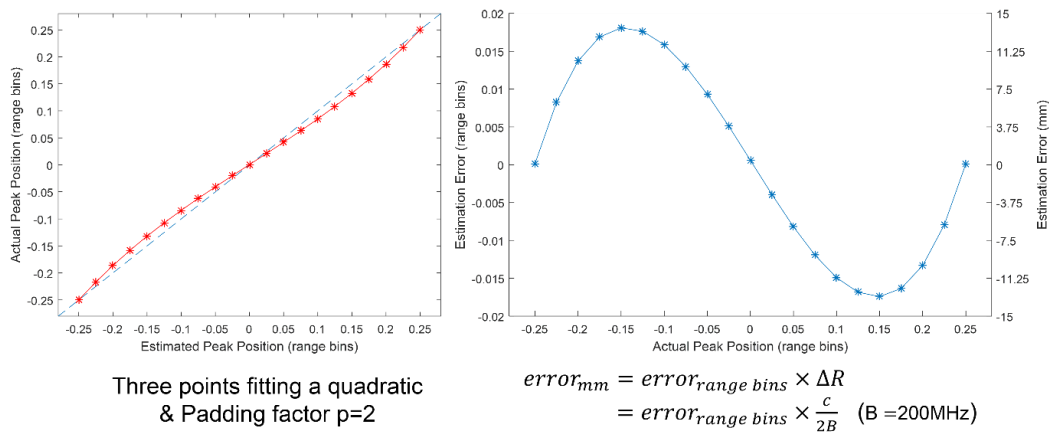


Figure 6.2 Quadratic interpolation with padding factor p=2

The equation of estimation calculation shown in Figure 6.2 is

$$\begin{aligned} error_{mm} &= error_{range\ bins} \times \Delta R \\ &= error_{range\ bins} \times \frac{c}{2B} \end{aligned} \quad (6.1)$$

It is therefore convenient to convert the estimation error by range bins to that by millimetres.

When the zero-padding factor $p = 1$, the estimation performance of the quadratic interpolation can be shown in Figure 6.3. Estimated peak positions still fluctuate around the actual peak position. Estimation performance is best when the actual range is either very close to a sample range or exactly halfway between two sample ranges. At the same time, the worst-case error of -0.23 bins (172.5 millimetres when bandwidth $B = 200$ MHz) occurs when the actual peak is -0.355 bins away from a sample range.

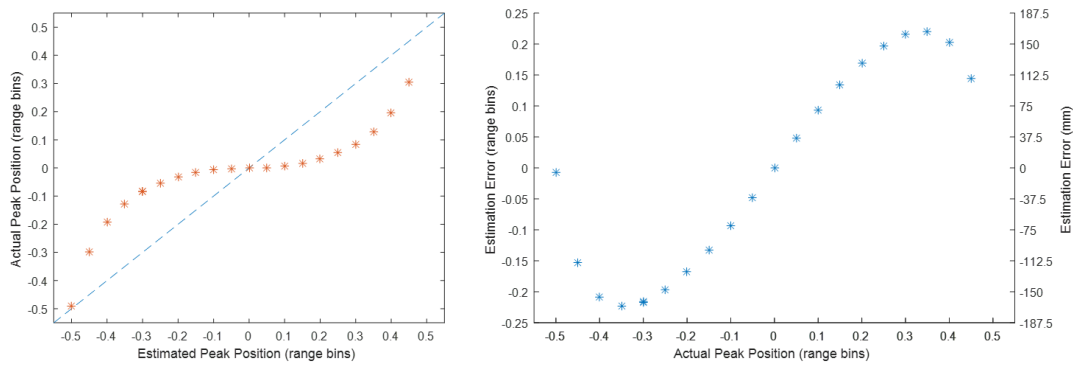
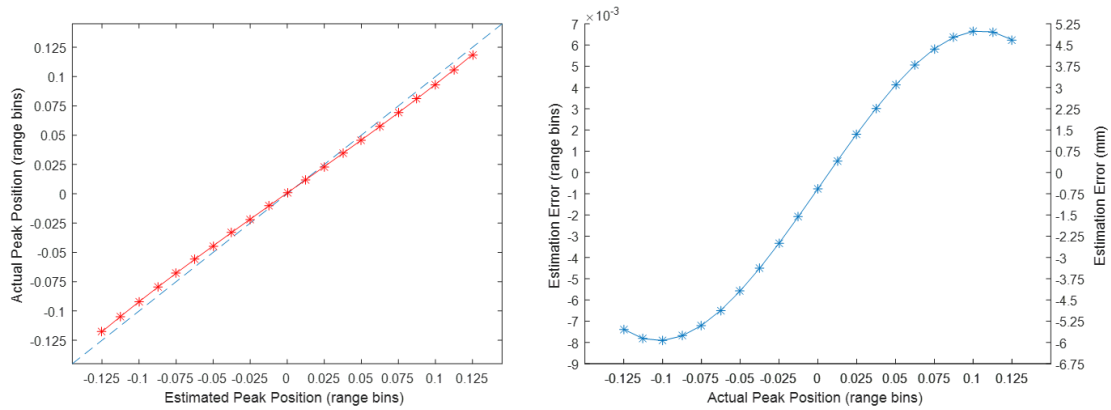


Figure 6.3 Quadratic interpolation with padding factor $p=1$

Figure 6.4 presents the estimation performance of the quadratic interpolation when the zero-padding factor $p = 4$. The interpolated range estimation is best when the actual range is either very close to a sample range or exactly halfway (± 0.125 here due to zero-padding factor $p = 4$) between two sample ranges. At the same time, the worst-case error of 0.008 bins (6 millimetres when bandwidth $B = 200$ MHz) occurs when the actual peak is -0.105 bins away from a sample range.

Figure 6.4 Quadratic interpolation with padding factor $p=4$

6.1.3 Results of Cubic Interpolation

In the scenario of cubic interpolation shown as Figure 6.5, when the zero-padding factor $p = 2$, estimated peak positions still fluctuate around the actual peak and the worst-case error of -0.054 bins (40.5 millimetres when bandwidth $B = 200$ MHz) occurs when the actual peak is -0.25 bins away from a sample range.

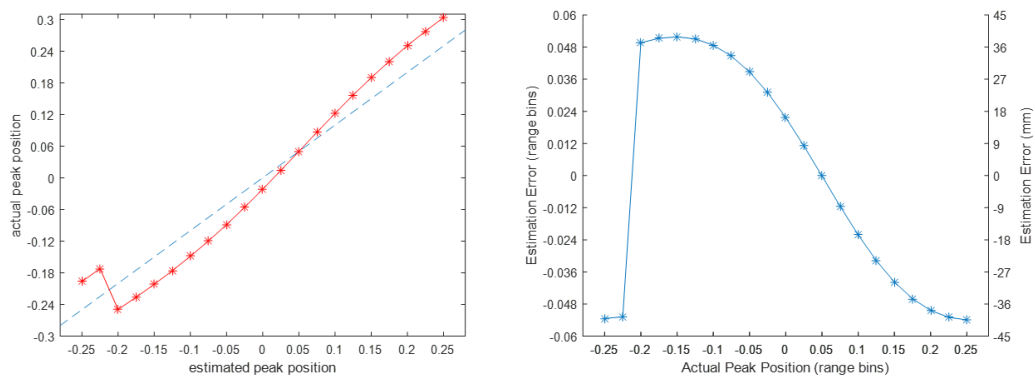
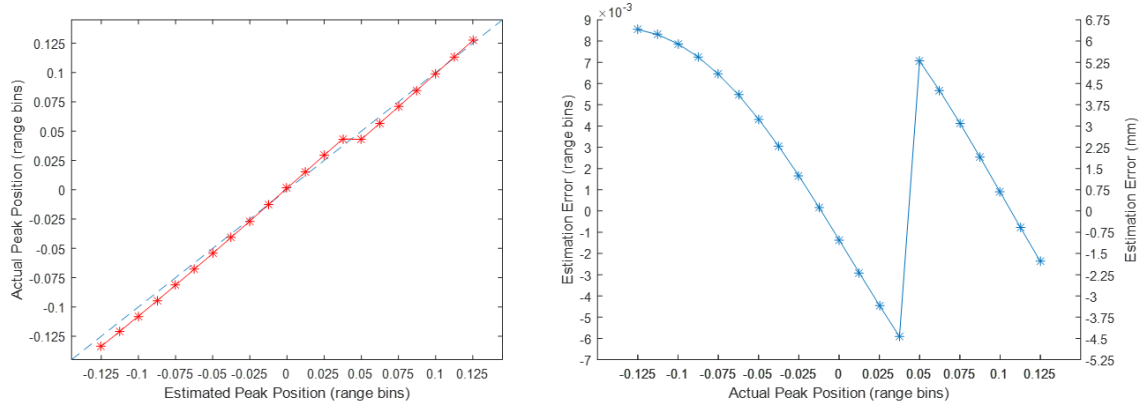
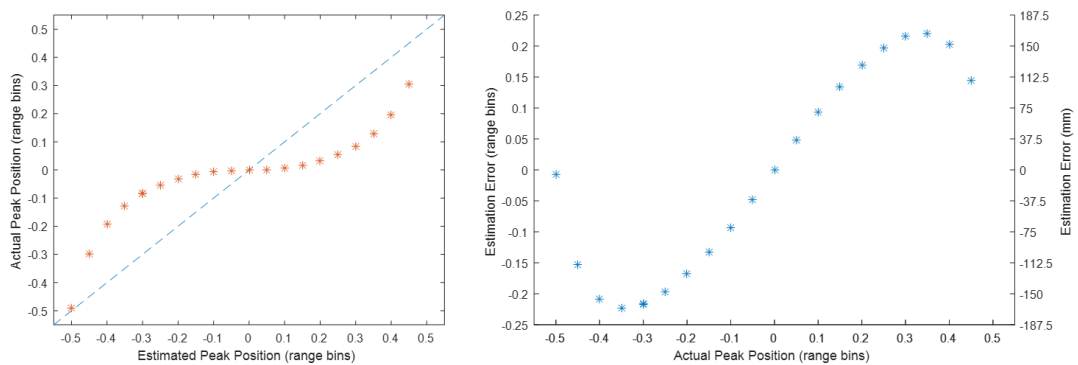
Figure 6.5 Cubic interpolation with padding factor $p=2$

Figure 6.6 presents the estimation performance of the quadratic interpolation when the zero-padding factor $p = 4$. The worst-case error of 0.0086 bins (6.45 millimetres when bandwidth $B = 200$ MHz) occurs when the actual peak is -0.125 bins away from a sample range.

Figure 6.6 Cubic interpolation with padding factor $p=4$

6.1.4 Results of Quartic Interpolation

For quartic interpolation shown as Figure 6.7 and 6.8, estimated peak positions still fluctuate around the actual peak position, and estimation performance is best when the actual range is either very close to a sample range or exactly halfway between two sample ranges. On the contrary, the worst-case error of -0.23 bins (172.5 millimetres when bandwidth $B = 200$ MHz) occurs when the actual peak is -0.355 bins away from a sample range with the zero-padding factor $p = 1$ and that of -0.23 bins (172.5 millimetres when bandwidth $B = 200$ MHz) when the actual peak is -0.355 bins away from a sample range with the zero-padding factor $p = 4$.

Figure 6.7 Quartic interpolation with padding factor $p=1$

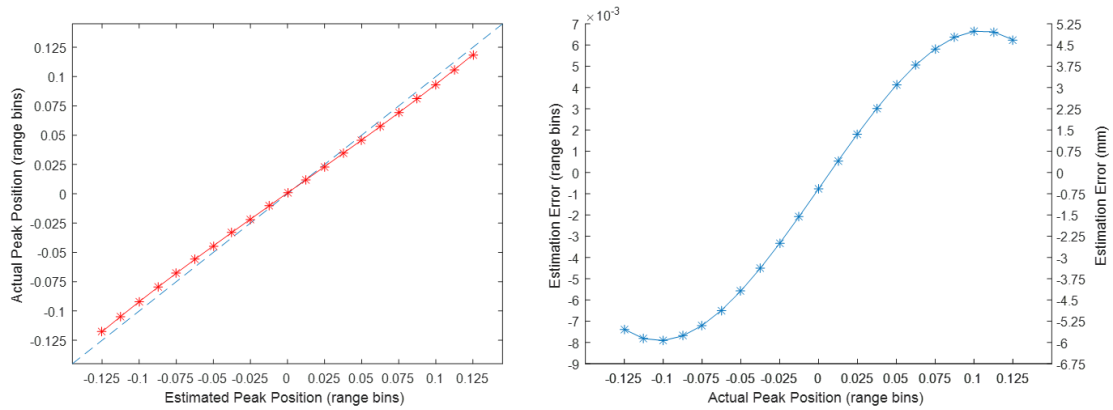


Figure 6.8 Quartic interpolation with padding factor p=4

6.2 Results of Most-likelihood Chirp Z Transform

As introduced in chapter 3 and 4, the most-likelihood chirp Z-transform (MLCZT) is computational effective to evaluate the Z-transform with a spiral contour, and it is useful in computing a subset of the DFT for a sequence. Unlike the DFT, the CZT is not restricted to operate along the unit circle but can evaluate along contours as the complex starting point. One possible spiral is illustrated as follow.

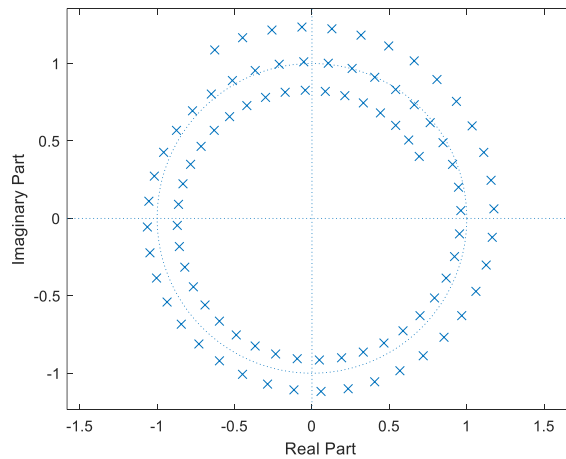


Figure 6.9 A spiral contour of MLCZT

If data samples are evenly presented around the unit circle ($A=1$ and $W=\exp(-j\pi/M)$), the Z-transform is exact the DFT under such circumstance; and CZT can be faster than the FFT function for computing the DFT of sequences with specific odd lengths.

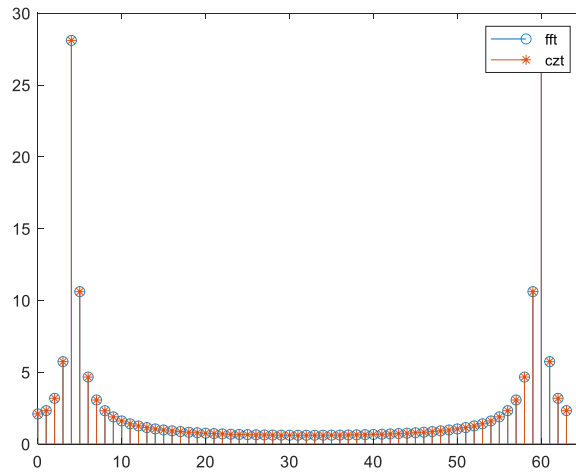


Figure 6.10 CTZ and FFT

Figure 6.11 illustrates the estimation performance of the MLCZT. As the figure is shown, estimated range bins fluctuate around the actual peak position. The range estimation is best when the actual range is either very close to a sample range, or exactly halfway between two sample ranges while the worst-case error of 0.019 bins occurs when the actual peak is 0.017 bins away from a sample range.

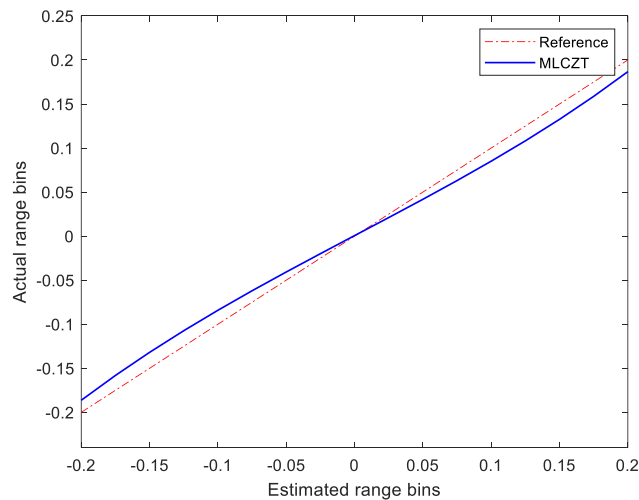


Figure 6.11 MLCZT error in range bins

As mentioned in the previous chapter, [63] introduced a chirp Z transform algorithm for an optimized FMCW application, and it proposed to calculate the phase via the CZT, as the CZT already calculated the complex frequency spectrum. However, its precision is limited due to the real-time requirement by means of FPGA fulfillment.

On the other hand, [97] presented a multi-target precise-ranging algorithm based on the CZT as well, for FMCW systems. It described that the performance was better than the FFT and MUSIC in white noise background; but its multi-target algorithm still needs to be optimized in the implementation of the periodogram.

Apart from the intrinsic advantage of chirp Z transform and absorbing the positive thoughts mentioned above, the CZT-based algorithm stated in the thesis utilised the most-likelihood process (estimator) creatively for improving range performance, by introducing and applying the concept and thought of statistical signal processing.

Besides, in terms of multi targets MLCZT algorithm, the multiple sinusoids estimate attained by the method of nonlinear least squares (NLS). The precise frequency estimation is attained through a data-fitting minimisation in the NLS approach. The estimation is asymptotically optimal under the circumstance of white Gaussian noise. The covariance matrix corresponds to the specific Cramer-Rao lower bound (CRLB). Thus, the covariance matrix of the chirp Z transform under white Gaussian noise can be presented with the form of a diagonal matrix (K is the observation index)

$$cov(\hat{\epsilon}) = \frac{6\sigma^2}{K^3} \begin{bmatrix} \frac{1}{a_0^2} & 0 & \cdots & 0 \\ 0 & \frac{1}{a_1^2} & \cdots & 0 \\ \vdots & \vdots & \ddots & \vdots \\ 0 & 0 & \cdots & \frac{1}{a_k^2} \end{bmatrix} \quad (6.2)$$

where σ^2 is the noise variance and $(a_0^2, a_1^2, \dots, a_k^2)$ are the amplitudes of the sinusoids. NLS algorithm performs decently in both white and coloured noise.

This chapter analyses the results and data obtained by simulations, beginning with pre-processing the acquired raw time-domain data, then the processing results of polynomial interpolation and most-likelihood chirp-Z transform technique as well. Relative drawbacks and improvements are discussed from several aspects under different conditions.

7. Experimental Results and Discussion

Those primary processing results have been analysed above, and further discussion is undertaken in this section for practical improvements. As derived in Chapter 4, the amplitude of the estimated peak $A' = Y[x_n + \Delta x]$ of the quadratic interpolation can be written as

$$Y[x_n + \Delta x] = \frac{1}{2} \{ (\Delta x - 1)(\Delta x)y_{n-1} - 2(\Delta x - 1)(\Delta x + 1)y_n + (\Delta x + 1)(\Delta x)y_{n+1} \} \quad (7.1)$$

which Δx is the displacement of the estimated peak from the centre of the DFT sample point.

Note that the formula for Δx acts in instinctively satisfying ways. On the one hand, if the first and third DFT magnitude sample points are equal, $\Delta x = 0$; the middle point is the estimated peak for sure. On the other hand, if the first and second DFT magnitude sample points are equal, $\Delta x = 1/2$, indicating the estimated peak is halfway between the two sample points; an almost identical result exists if the second and third DFT magnitude sample points are equal.

This interpolation technique is ineffective when the width of the presumed interpolated main lobe is quite narrow so that the apparent peak and its two adjacent samples are not on the same lobe of the response. This occurs when the spectrum is sampled at the Nyquist rate in Doppler when the DFT size K equals the number of data sample N . Meanwhile, no window is applied to the data, and the data frequency does not coincidentally fall on a DFT frequency sample, which is the very situation where interpolation is considerably requisite. If the interpolation procedure is applied to these data, poor results will be achieved because the assumption that the three points are on an approximately quadratic curve segment is not valid. For these specific data, the interpolation technique will estimate the “true” frequency and amplitude of the spectral peak. The amplitude estimate is enhanced only faintly. The relative frequency error is decreased remarkably; however, it is still substantial.

This problem can be avoided by ensuring that the sample set is dense enough within computational feasibility, to guarantee that the three samples are all on the main lobe. One approach to solve this is to oversample in the Doppler domain; for example, selecting the DFT size K larger than the number of data sample N . Another practical way is to window the sample data. For most common windows, the expansion of the main lobe that results is sufficient to guarantee that the apparent peak samples and its two neighbours fall on the same lobe, so that the underlying assumption of a parabolic segment is more valid.

7.1 FFT Process with Window Functions

As mentioned above, the Doppler resolution depends on the observation time of the measurement. More extended observation provides better Doppler resolution. Because of the high side lobes, it is common to use a data window function $w[m]$ to weight the slow-time data samples $y[m]$ before computing the DTFT. Consider a radar tracking an object over a dwell of N pulses, and assume the target is present in a particular range bin. The slow time received signal after quadrature demodulation can be presented as

$$y[m] = Ae^{j2\pi F_D m T} \quad m = 0, \dots, M-1 \quad (7.2)$$

where F_D is the Doppler shift stemming from the target's velocity; T is the PRI of the radar, which is the effective sampling interval in the slow time domain. Now converting Equation to the formation of analogue frequency

$$Y(F) = A \frac{\sin[\pi(F - F_D)MT]}{\sin[\pi(F - F_D)T]} e^{-j\pi(m-1)(F-F_D)T} \quad F \in [-PRF/2, PRF/2] \quad (7.3)$$

Replacing $y[n]$ by $w[m]y[m]$, and using the form of Equation (4.3) again. After converting from normalised frequency to hertz and recognising that $y[m]$ is finite length

$$Y_\omega[F] = A \sum_{m=0}^{M-1} w[m] e^{-j2\pi(F-F_D)mT} \quad (7.4)$$

From Equation (7.3), the peak value of $|Y(F)|^2$ when no window is used is $A^2 M^2$. Evaluating Equation (4.5) at $F = F_D$ gets the peak power when a window is used

$$|Y(F_D)|^2 = \left| A \sum_{m=0}^{M-1} w[m] e^{-j2\pi(0)mT} \right|^2 = A^2 \left| \sum_{m=0}^{M-1} w[m] \right|^2 \quad (7.5)$$

The ratio $|Y(F_D)|^2 / |Y(F)|^2$ can be called the loss in processing gain (LPG)

$$LPG = \frac{|Y(F_D)|^2}{|Y(F)|^2} = \frac{1}{M^2} \left| \sum_{m=0}^{M-1} w[m] \right|^2 \quad (7.6)$$

From the equation above, it can be calculated that $LPG \leq 1$, the loss in dB is, therefore, a negative number. The LPG can be computed for any window by Equation (7.6). Explicit values depend on the specific window function, which 5 to 8 dB are typical, but the LPG is typically a weak function of the window length M , highest for small M and the rapidly approaching an asymptotic value for large M .

Although the window reduces the peak amplitude considerably, it reduces noise power as well. Processing loss (PL) is the reduction in SNR at the peak of the DTFT. Denoting the SNR with and without

the window as χ and χ_ω , respectively, it is reasonable to separate the effects of the window on the target and noise components of the signal

$$\frac{\chi_\omega}{\chi} = \frac{(S_\omega/N_\omega)}{(S/N)} = \left(\frac{S_\omega}{S}\right)\left(\frac{N_\omega}{N}\right) = LPG\left(\frac{N}{N_\omega}\right) \quad (7.7)$$

To determine the window's effect on the noise power N , suppose $y[n]$ is a zero-mean stationary white noise with variance σ^2 . Therefore, the windowed noise power is

$$\begin{aligned} \sigma_\omega^2 &= E\left\{\left(\sum_{m=0}^{M-1} w[m] y[m]\right)\left(\sum_{m=0}^{M-1} w^*[n] y^*[n]\right)\right\} \\ &= E\left\{\left(\sum_{m=0}^{M-1} |w[m] y[m]|^2\right) + \text{cross terms}\right\} \\ &= \sigma^2 \sum_{m=0}^{M-1} |w[m]|^2 = N_\omega \end{aligned} \quad (7.8)$$

The un-windowed noise power can be given by Equation, setting $w[m] = 1$ for all m , assuming $N = M\sigma^2$. Combining Equation (7.6) and (7.8) obtains the processing loss

$$PL = \frac{|\sum_{m=0}^{M-1} w[m]|^2}{M \sum_{m=0}^{M-1} |w[m]|^2} \quad (7.9)$$

Table 7.1 Properties of a variety of common data windows [41]

Window	Main lobe width	Peak gain (dB)	Peak side lobe(dB)	SNR loss(dB)
Rectangular	1.0	0.0	-13	0
Hamming	1.46	-5.4	-43	-1.35
Hanning	1.62	-6.0	-32	-1.76
Kaiser, $\alpha=2.0$	1.61	-6.2	-46	-1.76
Kaiser, $\alpha=2.5$	1.76	-8.1	-57	-2.17
Dolph-Chebyshev (50-dB equiripple)	1.49	-5.5	-50	-1.43
Dolph-Chebyshev (70-dB equiripple)	1.74	-6.9	-70	-2.10

Similar to the loss in peak gain, the processing loss is also a weak function of N that is higher for small N but swiftly approaches an asymptotic value. For instance, the loss in SNR ratio for Hamming

window is -1.75dB for a short window, decreasing asymptotically to about -1.35dB for the long window. Table 7.1 summarises four primary characteristics of several common windows. The main lobe width and peak gain are both relative to the rectangular window. SNR loss refers to the signal-to-noise ratio-loss.

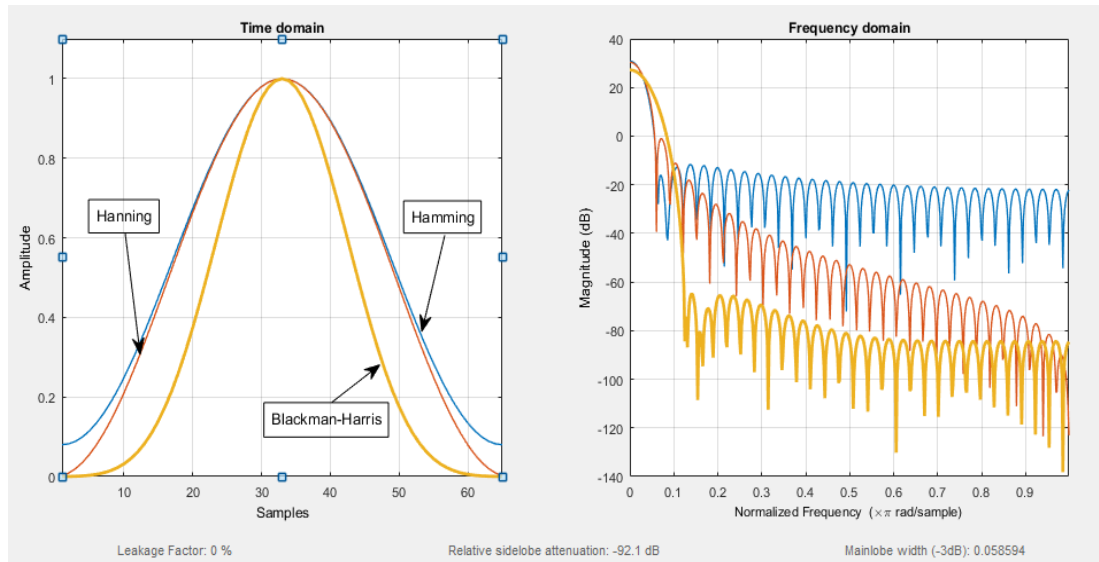


Figure 7.1 Features of three kinds of window function

Implementing an N -point window to the full length of a zero-padded sequence has the effect of multiplying the data by a truncated and asymmetric window, leading to substantially increased side lobes. Moreover, rectangular windows are equivalent to no window. In contrast, non-rectangular windows cause an increase in main lobe width, a decrease in peak amplitude, and a decrease in SNR in exchange for substantial reductions in peak sidelobe level. Figure 7.1 illustrates the features of three window functions which are commonly used, from both time and frequency domain. For most common windows introduced above, the expansion of the main lobe that results is sufficient to ensure that the apparent peak samples and its two adjacent points fall on the just same lobe, in that the underlying assumption of a polynomial segment is more valid.

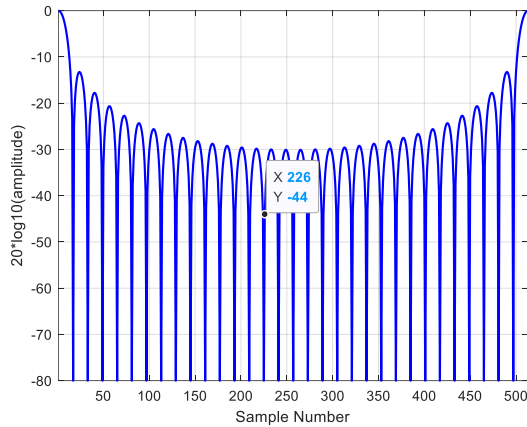


Figure 7.2 Normalised Amplitude Spectrum of Rectangle Window

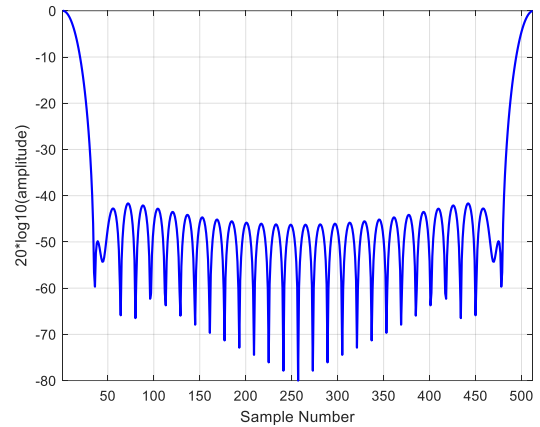


Figure 7.3 Normalised Amplitude Spectrum of Hamming Window

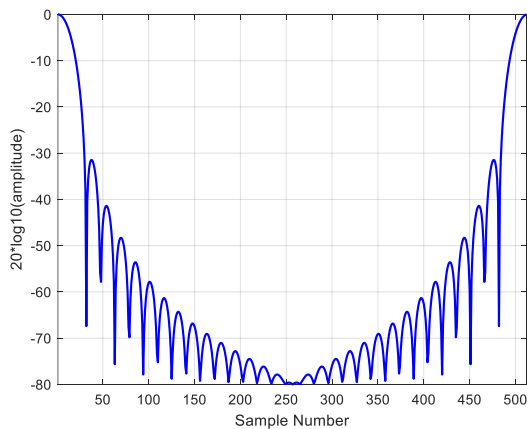


Figure 7.4 Normalised Amplitude Spectrum of Hanning Window

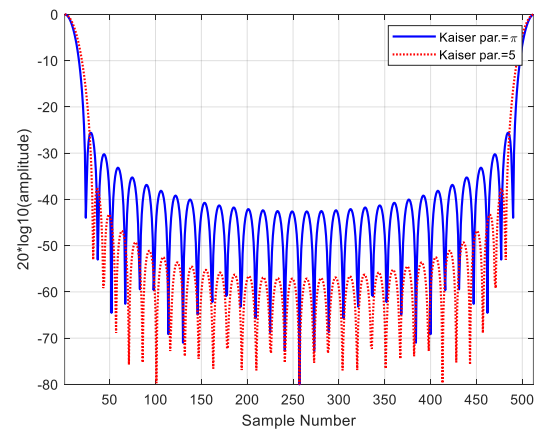


Figure 7.5 Normalised Amplitude Spectrum of Kaiser Window

The figures illustrated above present the normalised amplitude spectrum of several common window functions which are used frequently. Figure 7.2 shows the normalised amplitude spectrum of a rectangular window; Figure 7.3 illustrates the normalised amplitude spectrum of a Hamming window. The normalised amplitude spectrum of Hanning and Kaiser windows are presented in Figures 7.4 and 7.5 correspondingly.

7.2 Further Results of Polynomial Interpolation

Ten cycles of the deramped signal are illustrated in Figure 7.6. The original signal is zero-padded and windowed; the function of the Hamming window in the time-domain is shown as well.

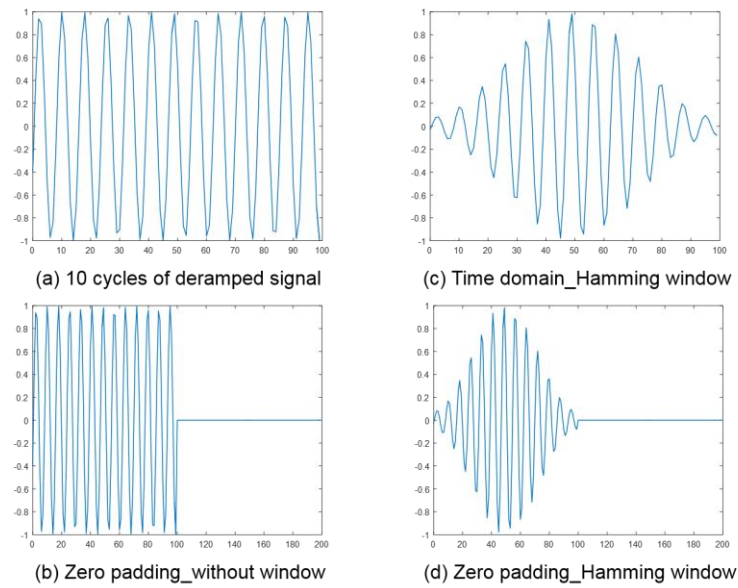


Figure 7.6 Deramped Signal with zero-padding and window

The target is a range extent target; the SNR is distinctive, and the precision of detection deteriorates if SNR decreases notably. In terms of clutter, it consists of the faint multi-scattering and multi-reflection of the target and multi-path effect by the surrounding walls, etc. (desks and chairs had been removed and the whole room was cleared as possible except the set instruments before the experiments.)

Figure 7.7 illustrates the estimation performance of the parabolic interpolation, both without and with Hanning windowing, on a sinusoidal data sequence. The interpolated range estimates are best when the actual range is either very close to a sample range or exactly halfway (± 0.25 here due to zero-padding factor $p = 2$) between two sample ranges. If no window is used, the worst-case error of 0.018 bins (13.5 millimetres when bandwidth $B = 200$ MHz) occurs when the actual peak is 0.15 bins away from a sample range; a Hanning window decreases this maximum error to 0.007 bins (5.25 millimetres when bandwidth $B = 200$ MHz) at an offset of 0.16 bins.

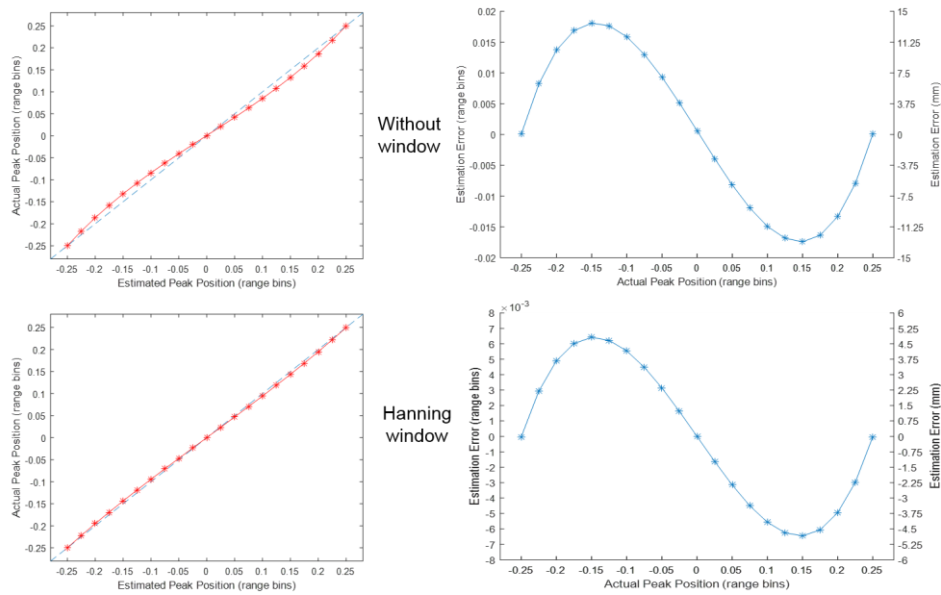
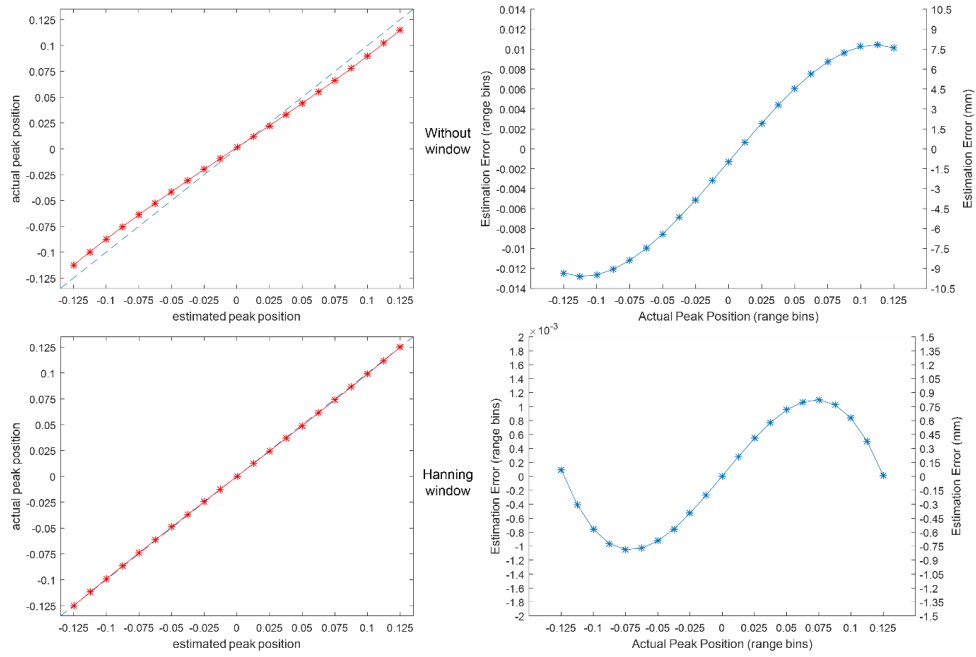


Figure 7.7 Estimation Performance of Quadratic Interpolation with/without window function

The estimation performance of the quartic interpolation is shown in Figure 7.8, both without and with Hanning windowing as well. Similar as the circumstance of the quadratic interpolator, the interpolated range estimates here are best when the actual range is either very close to a sample range, or exactly halfway (± 0.125 here due to zero-padding factor $p = 4$) between two sample ranges. If no window is used, the worst-case error of 0.013 bins (9.75 millimetres when bandwidth $B = 200$ MHz) occurs when the actual peak is 0.11 bins away from a sample range; a Hanning window decreases this maximum error to 0.0011 bins (0.85 millimetres when bandwidth $B = 200$ MHz) at an offset of 0.075 bins.



Five points fitting a quartic & padding factor p=4

Figure 7.8 Estimation Performance of Quartic Interpolation with/without window function

Table 7.2 presents the processing error of polynomial interpolators with different factors and conditions. These results confirm that the interpolators perform better with the higher order of the polynomial, though the computational effectiveness drops correspondingly; polynomial performance can be enhanced by zero-padding before processing and windowing during the processing at a certain extend. Note that those outcomes shown above may look decent, however, after introducing a higher noise figure into the processing, the performances of polynomial interpolators deteriorate noticeably. Further research will concentrate on anti-noise potential and robustness of the algorithm to mitigate the performance distinction between the ideal simulation and practical usage.

Table 7.2 Polynomial interpolation Error under several conditions

	RMS Error (range bin)	RMS Error (mm)
Quadratic interpolation, $p=1$, no window	0.1051	78.825
Quadratic interpolation, $p=2$, no window	0.0124	9.300
Quadratic interpolation, $p=4$, no window	0.0056	4.200
Quadratic interpolation, $p=2$, Hanning window	0.0045	3.375
Quartic interpolation, $p=4$, no window	0.0118	8.850
Quartic interpolation, $p=4$, Hanning window	0.0037	2.775

Besides, as described above, rectangular windows are equivalent to no window. In contrast, non-rectangular windows cause an increase in main lobe width, a decrease in peak amplitude, and a decrease in signal-to-noise ratio in exchange for significant reductions in peak sidelobe level. Moreover, the FFT algorithm is a practical computational method to compute the DFT; the DFT computes K samples of the DTFT evenly spaced across one period of the DTFT. Therefore, the peak value of the DFT acquired regarding the desired target signal is highest when the Doppler frequency falls on one of the DFT sample frequency coincidentally, while the value decreases when the target signal is between DFT frequencies. This reduction in amplitude is called a Doppler straddle loss. The amount of loss depends on the particular window applied. Meanwhile, for a given frequency, the maximum straddle loss increases when the DFT size K is decreased. Considering the smallest DFT size $K = M$, the straddle loss is obtained via the definition of the DFT

$$Y[k] = \sum_{m=0}^{M-1} y[m] e^{-j2\pi mk/K} \quad k = 0, \dots, K-1 \quad (7.10)$$

and evaluating the equation above with $y[m] = \omega[m]$, $K = M$, and $k = 1/2$. This is the gain at the halfway point between the $k = 0$ and $k = 1$ DFT bins, which is the same halfway between other bins as well. The computation can be repeated with $k = 0$ to obtain the peak gain, and the ratio evaluated. Consider the scenario of the rectangular window

$$|Y[k]| = \left| \sum_{m=0}^{K-1} e^{-j2\pi mk/K} \right| = \left| \frac{\sin(\pi k)}{\sin(\pi k/K)} \right| \quad (7.11)$$

evaluating at $k = 1/2$ yields

$$\left| Y \left[\frac{1}{2} \right] \right| = \left| \frac{\sin(\pi/2)}{\sin(\pi/2K)} \right| = \frac{1}{\sin(\pi/2K)} \approx \frac{2K}{\pi} \quad (7.12)$$

The last procedure was obtained by assuming that K is large enough to allow a small angle approximation to the sine function in the denominator. Meanwhile, $Y[0] = K$ can be computed by Equation (5.13). Thus the maximum straddle loss for the DFT filter-bank with no windowing (equivalent to a rectangular window) is $20 \log_{10}(2/\pi) = -3.92 \text{ dB}$ in decibels; while there is a smaller maximum straddle loss of 1.74 dB for Hamming window by a similar calculation. And in consequence, any non-rectangular window leads to a reduction in peak gain, and typical windows have the desirable characteristic of having less variability in gain because of the variance of the target's Doppler shift. The variation in amplitude is substantially less for the window data, which means the amplitude response is more consistent. This greater consistency of response is, therefore, an underappreciated benefit of the window. Therefore, some caution is needed in applying a data window during the process procedures, and parts of factors among them entail further research on it.

7.3 Comparison between Coherent and Non-Coherent Ranging Approaches

A variety of simulation outcomes based on non-coherent technique are demonstrated in the previous sections. As a contrast, the following part is devoted to a coherent ranging approach. The system structure of the FMCW radar (ApRES system) is described in Chapter 3; experimental results are shown below. This ApRES system applies an Analog Devices AD9910 DDS synthesiser, generating a 200-400 MHz chirp signal with a 1 GHz clock. A pair of Mini-Circuits ZX76-31-PP+ digital step attenuators are employed to provide a range of receiver gain setting. Careful hardware designs and processing approaches are applied to attain stable and precise range estimation. FMCW signal processing is used to detect the targets and measure their coarse ranges. Then phase-sensitive signal processing is applied to determine their exact ranges from the central unit.

Figure 7.9 presents an experimental layout in the Marconi Room and the primary part of system hardware; important parameters of the FMCW radar are shown in Table 7.3. Besides of the FMCW radar system (ApRES prototype), there were several other instruments applied, including bow-tie antennas (Tx and Rx), antennas stand, transponder, cables, and oscilloscope Tektronix MDO4140-6, etc.

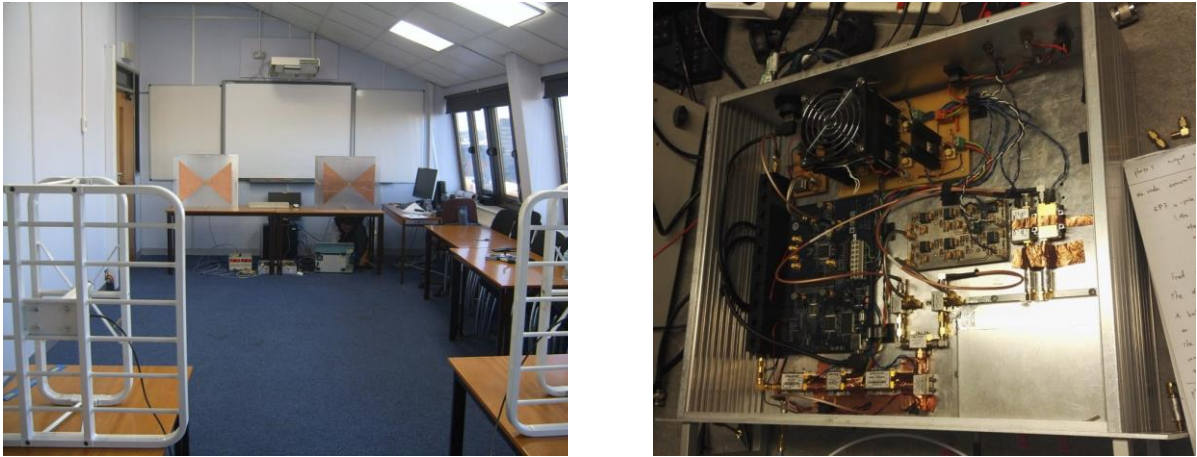


Figure 7.9 Experimental System and Layout of an FMCW radar prototype

Table 7.3 Principal Radar Parameters

Operating (Central) frequency f_c	300 MHz
FM sweep bandwidth B	200MHz
RF power P_t	20 dBm
Antenna gain G_t, G_r	10 dBi
Noise figure N	6 dB (F=4)
Pulse duration	1 S
ADC Sampling rate	> 12 ksamples/s

The deramped signal of loop test is illustrated in Figure 7.10; the IF (intermediate frequency) signal was measured directly out of the mixers of IF port. Meanwhile, auxiliary in-line attenuators (30 dB and 50 dB) were applied to ensure RF (radio frequency) input to the mixer was desired below its saturation point. A 145 Hz signal is shown at $1.01 V_{pp}$ into high impedance load, consequently the 50Ω power level of -1.95 dBm and -21.06 dBm with the 30 dB and 50 dB attenuators, respectively. The deramped frequency in both figures is 145 Hz; the PRF (pulse repetition frequency) is 20 Hz in the right figure.

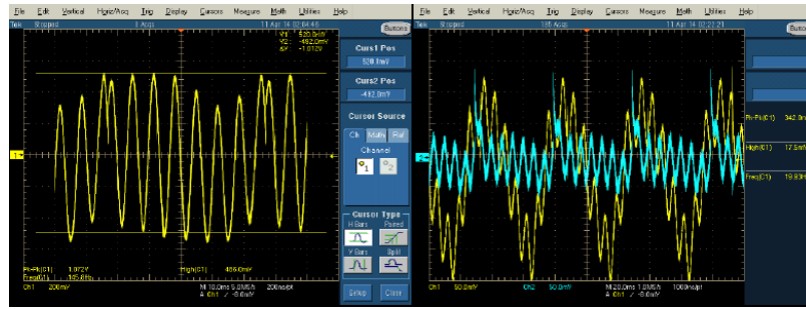


Figure 7.10 Deramped Signals of Loop Test

Figure 7.11 illustrates the frequency spectrum and range profile of the loop test, and both I and Q channels flowing through the oscilloscope. As shown in Table 7.4, as an experimental cable with the full length of 270 m, the rough estimation of range bin is 135.2190 metres as half (270.4380 metres totally); the phase peak degree is -136.9048 , and the range error is -0.1736 metres; the final estimated range obtained from the phase-sensitive processing is 135.0454 metres as half (270.0908 metres totally), indicating that the estimated error is diminished and the estimation performance is enhanced after applying the phase-sensitive processing.

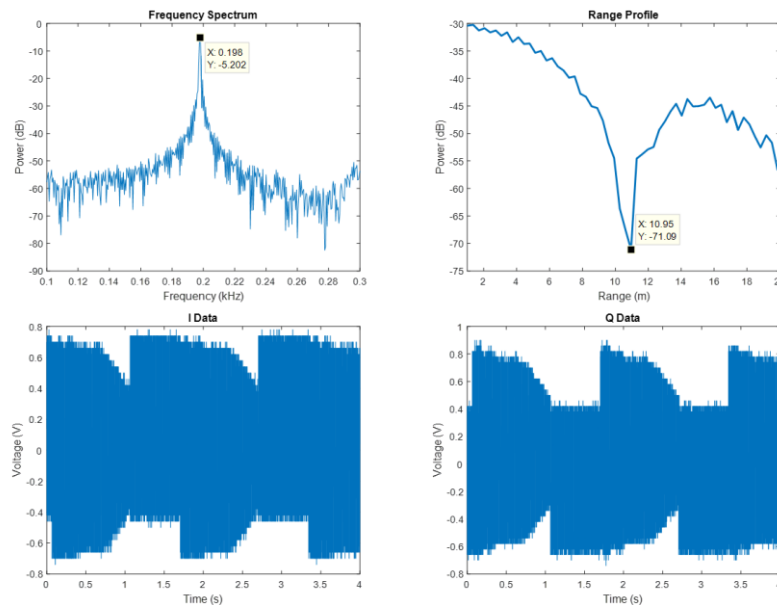


Figure 7.11 Frequency Spectrum and Range Profile of Loop Test

Table 7.4 Processing Results of Loop Test

Range bin metres	Cable length	Phase peak degrees	Range error	Estimated range metres	Vrms
135.2190	270.4380	-136.9048	-0.1736	135.0454	1.1572

Now set transponder distance to radar 4 metres, local oscillator (LO) power 15.5 dB, and use double antennas with 50 centimetres separation, the frequency spectrum and range profile can be seen in Figure 7.12 (both I and Q channels still flowing through the oscilloscope). Meanwhile, in Table 7.5, the rough estimation of range bin is 135.2190 metres as half (270.4380 metres totally); the phase peak degree is -74.7725; the final estimated range obtained from the phase-sensitive processing is 135.1242 metres as half (270.2484 metres totally), and the range error is -0.0948 metres.

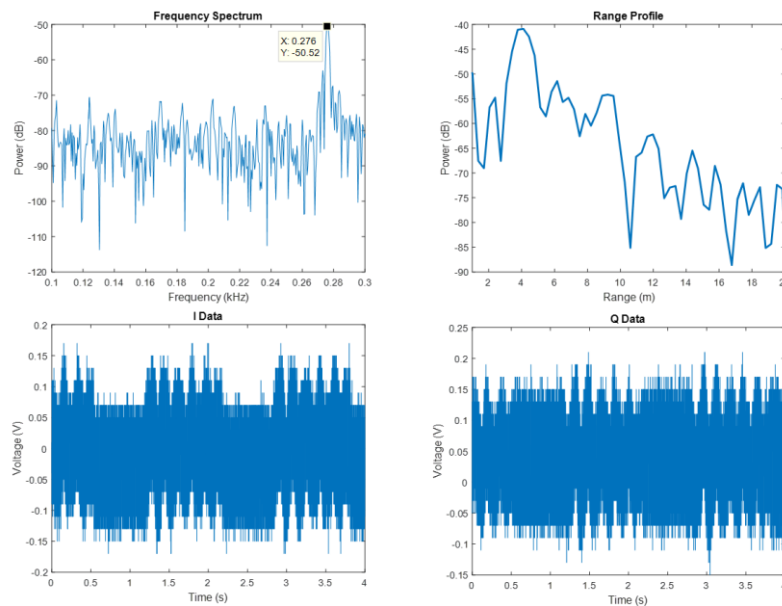


Figure 7.12 Frequency Spectrum and Range Profile with LO power 10.5 dBm

Table 7.5 Processing Results with LO power 10.5 dBm

Range bin metres	Cable length	Phase peak degrees	Range error	Estimated range metres	Vrms
135.2190	270.4380	-74.7725	-0.0948	135.1242	0.0960

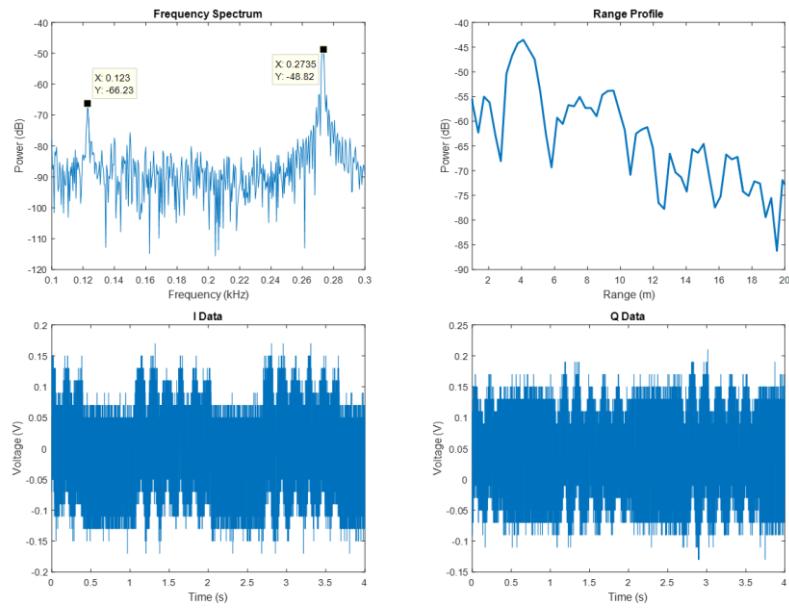


Figure 7.13 Frequency Spectrum and Range Profile with LO power 15.5 dBm

Table 7.6 Processing Results with LO power 15.5 dBm

Range bin metres	Cable length	Phase peak degrees	Range error	Estimated range metres	Vrms
134.5344	269.0687	18.6624	0.0237	134.5580	0.0930

Now keep all other conditions fixed and just alter local oscillator (LO) power to 15.5 dB, the frequency spectrum and range profile can be seen in Figure 7.13 (both I and Q channels still flowing through the oscilloscope). Meanwhile, in Table 7.6, the rough estimation of range bin is 134.5344 metres as half (269.0688 metres totally); the phase peak degree is 18.6624; the final estimated range obtained from the phase-sensitive processing is 134.5580 metres as half (269.1160 metres totally), and the range error is 0.0237 metres.

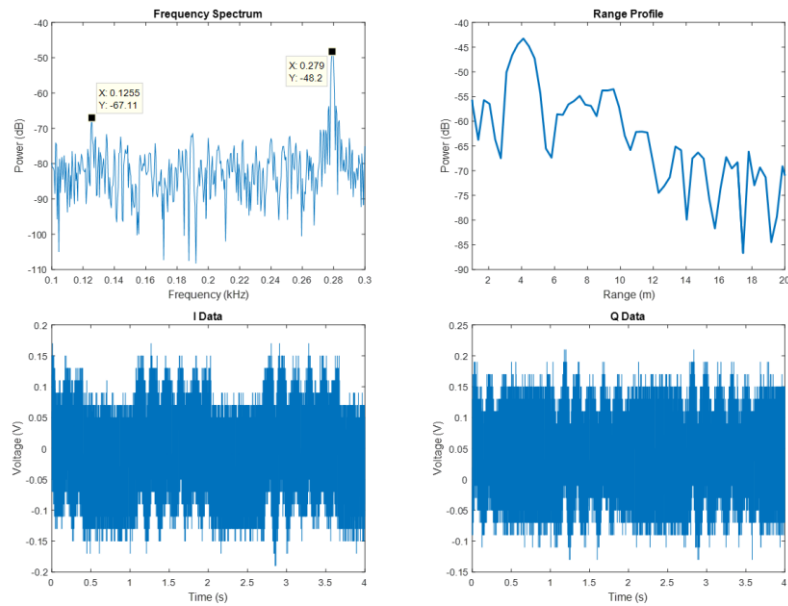


Figure 7.14 Frequency Spectrum and Range Profile with LO power 17.5 dBm

Table 7.7 Processing Results with LO power 17.5 dBm

Range bin metres	Cable length	Phase peak degrees	Range error	Estimated range metres	Vrms
134.1920	268.3841	145.5005	0.1845	134.3765	0.0979

Keep all other conditions fixed and just alter local oscillator (LO) power to 17.5 dB, the frequency spectrum and range profile can be seen in Figure 7.14 (both I and Q channels still flowing through the oscilloscope). In Table 7.7, the rough estimation of range bin is 134.1920 metres as half (268.3840 metres totally); the phase peak degree is 145.5005; the final estimated range obtained from the phase-sensitive processing is 134.3765 metres as half (268.7530 metres totally), and the range error is 0.1845 metres.

A practical deficiency needed to mention here is that the results section shows distances measured to 0.0001 metres accuracy. However, based on the precision of the gauging system, it may not necessarily be easy to validate in practice regarding the 0.0001 metres accuracy statement (i.e., the precise length of the test cable).

For the length of a physical RF cable, there is still a method of the finite difference to present results to 4 decimal places by means of the difference. The absolute value of length may not be feasible to achieve mm-level precision under current circumstance while the result of difference of two sections of a range extent cable could reach close but not exact precision.

Though the finite difference method mentioned previously may contribute to the statement of accuracy, to some extent, I must admit that 0.0001 metres accuracy is currently not practically achievable; it is not practical to justify such precise experimental results without using corresponding accurate measurements. The feasible level of precision should be 0.001 metres, which can be credibly measured and validated by means of regular gauging tools.

When it comes to the structure of radar systems, whether the radar is coherent or non-coherent depends on both the hardware and the processing, respectively. Since the phase information has been introduced to the procedure of process, the hardware of a coherent radar will differ from the non-coherent system (e.g., an extra mixer and the following signal conditioning circuit among the post-processing chain). On the other hand, a typical FMCW radar may use phase-sensitive processing or non-coherent processing, but it's not the same radar architecture.

As a coherent ranging approach (ApRES system) presented above, the primary comparison is that with ApRES, the approximate position of the peak of the FFT is measured and used in conjunction with the phase of the FFT to get high precision. In contrast, the non-coherent approach derived in the thesis is to attempt to measure the peak position more precisely, using interpolation. Further free-space experimental validations will be undertaken, and precise quantitative analysis will be conducted in the next phase.

Experimental results and discussion are presented in this chapter. Window functions are introduced to evaluate and analyse the performance of these techniques. Further results of polynomial interpolation are presented as well. At the rest part of the chapter, coherent and non-coherent ranging approaches are compared based on experimental data to summarise several advantages and disadvantages as conclusions for further research.

8. Conclusions and Future Work

This chapter describes the conclusion of this thesis and the future work plan. It summarises the whole thesis and goes on to convey the next steps needed to be taken to develop and trial a location system that uses non-coherent techniques and compare/contrast it with a coherent approach (i.e., the ApRES system).

8.1 Conclusions

This thesis presents the derivation, simulation and experimental results of two novel ranging techniques with high-precision performance, namely, the K th-order polynomial interpolation technique and most-likelihood chirp-Z transform technique. In terms of the KPI technique, a desired ranging performance is achieved by a general expression of N th order polynomial interpolation for the non-coherent ranging estimate. The excellent ranging estimate is obtained through a two-stage method applied to DFT domain precision via interpolating around the peak of range profiles of the deramped signals. An N -point DFT is implemented to attain a coarse estimation; an accurate process around the point of interests determined in the first stage is conducted. This approach is an uncomplicated and efficient solution to compromise the instinct deficit of the non-coherent structure.

Assume that the DFT $Y[x]$ is a function of a continuous frequency index x , since the goal is to estimate a peak location assumed to be between actual sample locations; in the vicinity of the DFT peak at x_n , considering those measurements respectively. Quadratic, cubic, and quartic interpolator are presented to measure the distinctive of the location of the interpolated peak relative to the index of the central sample of the DFT samples applied to the algorithm. The estimated peak positions fluctuate around the actual peak position. The interpolated range estimation is best when the actual range is either very close to a sample range or exactly halfway

An inner mathematical law can be found that the coefficients of both numerators and denominators satisfy the format of Pascal's triangle, which is a triangular array of the binomial coefficients indeed. A general expression for K th order polynomial interpolator can be therefore presented by the form of binomial coefficients, where $\binom{k}{i}$ is the corresponding binomial coefficient. Note that since the symmetrical property of an K th order polynomial will be apparently different when K is odd or even, it is plausible to have a unique representation for different circumstances, respectively.

For the most-likelihood chirp-Z transform technique, the computational speed and flexibility of the CZT algorithm are related to the FFT. As known, ordinary convolutions can be calculated by adding zeroes to the end of one or both sequences so that the correct numerical consequences for the initial convolution can be derived by a circular convolution.

The procedures of the MLCZT algorithm can be described as follow:

- 1) Calculate a coarse FFT with a sequence of K points;
- 2) Search for the local maximum on the specific FFT range bin and locate its corresponding frequency in $\hat{\omega}$;
- 3) Set P as the desirable MLCZT frequency precision;
- 4) Calculate the CZT within the region $\left(\hat{\omega} - \frac{\pi}{K}, \hat{\omega} + \frac{\pi}{K}\right)$, and search for the maximum via Most-likelihood method, using the foreknowledge to asymptotically reach to the MVU estimator;
- 5) Repeat step 4 until attaining desirable precision of range performance.

Such thought could be easily extended to the applications of multi-target ranging estimation, which the procedures of the extended MLCZT algorithm for multi-target estimation.

To evaluate the performance of developed ranging techniques, it is beneficial in practical applications to set a lower bound on the variance of any unbiased estimator. Generally, it permits us to evaluate whether an estimator is an MVU estimator or not. Meanwhile, it presents a reference to compare the performance of any unbiased estimator. It also indicates that it is physically impossible to search for an unbiased estimator with the variance less than the bound. Despite the existence of various similar variance bounds, the Cramer-Rao lower bound (CRLB) is by far the easiest to determine. Besides, the theory permits us to evaluate whether an estimator can hit the bound conveniently. If no such estimator exists, then we understand to search for estimators which are asymptotically close to the bound.

Mathematical expressions of CRLB of KPI and MLCZT algorithms are derived in chapter 5, namely the asymptotical CRLB under the distinctive circumstance and SNR regarding two algorithms respectively. The CRLB of KPI and MLZCT will be further researched to evaluate these techniques precisely and computationally conveniently. The CRLB of Kth-order polynomial interpolation (KPI) and most-likelihood chirp Z transform (MLCZT) algorithm can be presented as the factors of SNR and other significant parameters.

During the experimental validation shown in Chapter 6 and 7, several processing techniques as zero-padding and windowing are introduced to enhance ranging performance via distinct perspectives. Zero-padding can enhance the FFT resolution of a time-domain signal, rather than merely increase the length of the given sequence. At the same time, zero-padding cannot improve the spectral resolution

(the minimum fraction between two frequencies that can be distinguished). Applying an N-point window to the full length of a zero-padded sequence has the effect of multiplying the data by a truncated and asymmetric window, leading to substantially increased side lobes. Moreover, rectangular windows are equivalent to no window. In contrast, non-rectangular windows cause an increase in main lobe width, a decrease in peak amplitude, and a decrease in signal-to-noise ratio in exchange for substantial reductions in peak sidelobe level. For most common windows introduced above, the expansion of the main lobe that results are sufficient to ensure that the apparent peak samples and its two adjacent points fall on the just same lobe, in that the underlying assumption of a polynomial segment is more valid.

Range estimation can be operated by both non-coherent and coherent approaches; two distinct approaches have their pros and cons correspondingly. The non-coherent approaches are more straightforward, more robust to environmental effects such as multipath and clutter. Still, it provides lower precision while the coherent techniques offer higher precision but are more vulnerable to noise and clutter and phase wrap errors, particularly in a complex or harsh environment. A variety of processing techniques are employed to both structures for achieving desired ranging precision wherever they emanate from initially.

Processing outcomes illustrated in Chapter 4 confirm that the interpolators perform better with the higher order of the polynomial, though the computational effectiveness drops correspondingly; polynomial performance can be enhanced by zero-padding before processing and windowing during the processing at a certain extend. Note that those outcomes shown above may look decent, however, after introducing a higher noise figure into the processing of simulations, the performances of polynomial interpolators deteriorate noticeably. Further research will concentrate on anti-noise processing and robustness of the algorithm to mitigate the performance distinction between the ideal simulation and practical usage.

Compared with previous non-coherent ranging techniques, coherent range estimation is based not only on the amplitude of the signal but on its phase characteristics as well, allowing for greater precision than that given by the classic range resolution expression. The received vector is measured by relating the phase of the received signal to that of a stable reference oscillator in the radar system. The phase relationship is measured and processed over an extended time relative to the range delay time. Experimental data stemming from an FMCW radar system are therefore presented in comparison with the non-coherent approach. This ApRES system operates on a 200-400 MHz chirp signal with a 1 GHz clock. Careful hardware designs and processing techniques are applied to achieve a reliable and high-precision performance of range estimation. FMCW signal processing is used to detect the targets and measure their coarse ranges. Then phase-sensitive signal processing is applied

to determine their exact ranges from the central unit. Signal processing techniques are implemented to integrate standard FFT-based algorithm, providing a rough range estimate to the closest range bin, $n\Delta R$, with a delicate estimation determined by the phase information. Precise phase estimation is needed to determine the exact range bin close where a distinct target is located, and then calculate the fractional range within that specific range bin. The fine range is obtained from the phase of the range bin with the maximum magnitude

8.2 Future Work

8.2.1 System Development

Further research will be kept pushing forward to eventually develop and trial a location system using non-coherent techniques and make a comparison to coherent approaches. Potential two-step technical schedules in the future are shown as follow:

Technical Objective 1: Algorithm optimisation and Field Validation of Prototype

Based on the prototype of the ApRES radar, the primary technical objective is to establish an optimized architecture for the system and validate the performance of the prototype operating in a realistic field environment via outdoor tests. Meanwhile, radar signal processing algorithms will be optimised based on current research outcomes to establish a robust method for an estimate the range with millimetre-precision and also to attain a user-friendly interface for recording and display. Moreover, there is another task to achieve the credible validation regarding the 0.0001 metres precise measurement (0.001 metres currently by means of regular gauging tools). It is crucial to justify such accurate experimental measurements with corresponding measuring approaches which are required to extra considerate considerations .

Technical Objective 2: Cost-Optimisation and Commercialisation

The aim is to achieve system integration and cost-optimisation study for commercialisation of the proposed radar system. This will explore the opportunities for outsourcing radar manufacture in production perspective. Additionally, the experimental results achieved from the laboratory and field trials, which will be benchmarked against an existing system, will be used to help find and secure the potential opportunity of the proposed radar system.

8.2.2 High-precision Ranging on radar communication integration

Apart from the objective of system development, there is also another work proposal concentrated on the application of deep learning into the realm of digital radar and radar communication integration

Deep learning has been used for radar signal processing as target classification [120, 121]. It has promising potential for radar processing beyond that, for example, adaptive waveform design, precise localisation, optimal interference mitigation, and other related applications. In parallel to the described deep learning application in radar, the concepts of digital radar based on digital modulation like orthogonal frequency-division multiplexing (OFDM) [122, 123] and Phase modulated continuous wave (PMCW) have drawn attention much. Differing from FMCW radar, they generate digital waveforms and perform digital demodulation. For OFDM radar system, its structure provides sufficient flexibility in the waveform choice, which grants available capabilities to embed communication information into the radar waveform, even for an adaptive and software-defined pattern.

The OFDM waveform consists of a series of orthogonal components, and its complex amplitudes are modulated with radar modulation pattern or communication data. The OFDM waveform can be quickly produced through the inverse fast Fourier transform (IFFT) due to the intrinsic characteristics of the discrete Fourier transform (DFT). Correspondingly, the radar modulation pattern or communication data can be easily extracted at the receiver side via FFT. It provides efficient digital demodulation of radar waveforms, and decent efficiency and simple extraction of communication data.

In terms of a PMCW radar system, the phase-modulated waveforms can be efficiently generated by CMOS devices. A bank of digital correlators is applied to achieve range detection, while the Doppler processing is conducted by FFT or other methods. Multiply transmitting channels can operate simultaneously as the usage of orthogonal codes, and so that enables MIMO processing. Moreover, varies code selection brings the robustness against interference. Besides, compared to an OFDM radar system, Doppler shift harms PMCW waveforms because of the autocorrelation and cross-correlation properties, which leads to extra compensation in the domain of signal processing.

Comparing to typical Fourier-based processing, the performance of radar resolution and range unambiguity for related measurement parameters depend individually on sampling frequency and observation length to the corresponding dimension. Super-resolution frequency estimation methods are introduced to enhance a decent resolution; it can be concluded as a maximum-likelihood method,

subspace method, and compressed-sensing method. Furthermore, with the development of 5G (International Mobile Telecommunication 2020, IMT2020), the high-performance ranging techniques and algorithm can be widely used on massive MIMO systems, autonomous vehicles for detection and obstacle avoidance, wearable sensing equipment, Internet of Things, collaborative situational awareness, and radar-communication integration.

Appendixes

Appendix A: Matlab codes of polynomial interpolation

```

%% Quadratic Interpolation
clear all
close all

t=0:99;
L=length(t);
i=1;
dataactual=[];
dataestimated=[];
error=[];
for N=12.75:0.025:13.25

% generate CW signal
%N=13.2; %N to vary over ±0.5 for p=1, ±0.25 for p=2, ±0.125 for p=4, etc
f=N/L;
y=sin(2*pi*f*(t-0.5));
%y=y.*transpose(hanning(L)); %add window function
%y=awgn(y,10); %add white Gaussian noise to signal, SNR=10dB
%figure
%plot(t,y,'LineWidth',1);
% find spectrum
spec=abs(fft(y));
spec=spec(1:round(L/2))/max(spec);
%figure
%plot(t(1:round(L/2)),spec,'LineWidth',1)
%xlabel('number of cycles')

% zero pad
p=2;
if p>1
    y(101:p*100)=0;
end
f=0:p*100-1;
%figure
%plot(f,y,'LineWidth',1);
%m=fft(y);

```

```

% find spectrum
spec=abs(fft(y));
spec=spec/max(spec);
%figure
%f=f/p;
%plot(f,spec,'LineWidth',1)
% plot(t,spec,'*')
%axis([round(N)-3 round(N)+3 0 1])
%xlabel('number of cycles')
%
% estimate peak position from quadratic fit
[a,b]=max(spec);
% 3 points fit
yn=a;
ynminus1=spec(b-1);
ynplus1=spec(b+1);
actualdeltapeakpos=N-round(N);
estimateddeltaPeakpos=(ynminus1-ynplus1)/(ynminus1-2*yn+ynplus1)/2/p;
%estimateddeltaPeakpos=((yn-ynplus1)/(ynminus1-2*yn+ynplus1)+0.5)/p; %
different form, exactly same result
%
% calibration (without window/hamming/blackman--i>12;hanning--i>13;)
if i>20
    estimateddeltaPeakpos=estimateddeltaPeakpos+0.5;
end
dataactual(i)=actualdeltapeakpos;
dataestimated(i)=estimateddeltaPeakpos;
error(i)=dataestimated(i)-dataactual(i);
i=i+1;
end
%
% plot the estimated peak against actual position
x=-1:0.1:1;
zn=x;
figure
plot(x,zn,'--');
hold on

```

```

axis([-0.28 0.28 -0.28 0.28]) ⌘
plot(dataactual,dataestimated,'r-*') ⌘
xlabel('Estimated Peak Position (range bins)') ⌘
ylabel('Actual Peak Position (range bins)') ⌘
hold off ⌘
⌘
% plot delta estimation against actual position with double-y axes (range
bins/mm & without using function of 'plotyy') ⌘
figure ⌘
plot(dataactual,error,'-*') ⌘
axis([-0.28 0.28 -0.008 0.008]) ⌘
set(gca,'xtick',[-0.25:0.05:0.25]) ⌘
set(gca,'ytick',[-0.008:0.001:0.008]) ⌘
ax1=gca; ⌘
ax2=axes('position',get(ax1,'position'),'yaxislocation','right','color','no
ne'); ⌘
axis([-0.28 0.28 -6 6]) ⌘
set(gca,'xtick',[-0.25:0.05:0.25]) ⌘
set(gca,'ytick',[-6:0.75:6]) ⌘
set(ax1,'box','off') ⌘
xlabel('Actual Peak Position (range bins)') ⌘
ylabel(ax1,'Estimation Error (range bins)') ⌘
ylabel(ax2,'Estimation Error (mm)') %  $\Delta x \cdot \Delta R$ 
( $\Delta R=c/2B, B=200\text{MHz}$ ) ⌘
⌘
% error analysis ⌘
averageerror=mean(error) ⌘
rmserror=rms(error) ⌘
⌘
%% Cubic Interpolation ⌘
clear all ⌘
close all ⌘
⌘
t=0:99; ⌘
L=length(t); ⌘
i=1; ⌘
dataactual=[]; ⌘
dataestimated=[]; ⌘
error=[]; ⌘
for N=12.7:0.05:13.7 ⌘
⌘

```

```

% generate CW signal
%N=13.2; %N to vary over +/-0.5 for p=1, +/-0.25 for p=2, +/-0.125 for p=4,
etc
f=N/L;
y=sin(2*pi*f*(t-0.5));
%y=y.*transpose(blackman(L)); % add window function
%y=awgn(y,10); %add white Gaussian noise to signal, SNR=10dB
%figure
%plot(t,y,'LineWidth',1);
% find spectrum
spec=abs(fft(y));
spec=spec(1:round(L/2))/max(spec);
%figure
%plot(t(1:round(L/2)),spec,'LineWidth',1)
%xlabel('number of cycles')
%
% zero pad
p=1;
if p>1
    y(101:p*100)=0;
end
f=0:p*100-1;
%figure
%plot(f,y,'LineWidth',1);
%m=fft(y);
% find spectrum
spec=abs(fft(y));
spec=spec/max(spec);
%figure
f=f/p;
%plot(f,spec,'LineWidth',1)
% plot(t,spec,'*')
%axis([round(N)-3 round(N)+3 0 1])
%xlabel('number of cycles')
%
% estimate peak position from quadratic fit
[a,b]=max(spec);
yn=a;
ynminus1=spec(b-1);
ynplus1=spec(b+1);
ynminus2=spec(b-2);

```

```

ynplus2=spec(b+2);

$$\hat{a} > 0$$

actualdeltapeakpos=N-round(N);
if ynminus2<ynplus2
    if ynplus2-3*ynplus1+3*yn-ynminus1>0 % a>0
        estimateddeltaPeakpos=((ynplus1-2*yn+ynminus1)/(-ynplus2+3*ynplus1-3*yn+ynminus1)-sqrt(((ynplus1-2*yn+ynminus1)/(ynplus2-3*ynplus1+3*yn-ynminus1))^2+(ynplus1-ynminus1)/(-ynplus2+3*ynplus1-3*yn+ynminus1)+1/3))/p;
    else
        estimateddeltaPeakpos=((ynplus1-2*yn+ynminus1)/(-ynplus2+3*ynplus1-3*yn+ynminus1)+sqrt(((ynplus1-2*yn+ynminus1)/(ynplus2-3*ynplus1+3*yn-ynminus1))^2+(ynplus1-ynminus1)/(-ynplus2+3*ynplus1-3*yn+ynminus1)+1/3))/p;
    end
else
    if ynplus1-3*yn+3*ynminus1-ynminus2>0
        estimateddeltaPeakpos=((ynplus1-2*yn+ynminus1)/(-ynplus1+3*yn-3*ynminus1+ynminus2)-sqrt(((ynplus1-2*yn+ynminus1)/(ynplus1-3*yn+3*ynminus1-ynminus2))^2+(ynplus1-ynminus1)/(-ynplus1+3*yn-3*ynminus1+ynminus2)+1/3))/p;
    else
        estimateddeltaPeakpos=((ynplus1-2*yn+ynminus1)/(-ynplus1+3*yn-3*ynminus1+ynminus2)+sqrt(((ynplus1-2*yn+ynminus1)/(ynplus1-3*yn+3*ynminus1-ynminus2))^2+(ynplus1-ynminus1)/(-ynplus1+3*yn-3*ynminus1+ynminus2)+1/3))/p;
    end
end

$$\hat{a} < 0$$

%estimateddeltaPeakpos=((ynplus1-2*yn+ynminus1)/(-ynplus1+3*yn-3*ynminus1+ynminus2)
%
% calibration (p=2, i>12; p=4, i>5)
%if i>12
% estimateddeltaPeakpos=estimateddeltaPeakpos+0.5;
%end

$$\hat{a} < 0$$


```

```

dataactual(i)=actualdeltapeakpos;
dataestimated(i)=estimateddeltaPeakpos;
error(i)=dataactual(i)-dataestimated(i);
i=i+1;
end

% plot the estimated peak against actual position
x=-1:0.1:1;
zn=x;
figure
plot(x,zn,'--');
hold on
axis([-0.55 0.55 -0.55 0.55])
plot(dataactual,dataestimated,'*')
xlabel('Estimated Peak Position (range bins)')
ylabel('Actual Peak Position (range bins)')
hold off

% plot delta estimation against actual position with double-y axes (range
bins/mm & without using function of 'plotyy')
figure
plot(dataactual,error,'*')
axis([-0.55 0.55 -0.45 0.45])
set(gca,'xtick',[-0.5:0.1:0.5])
set(gca,'ytick',[-0.45:0.09:0.45])
ax1=gca;
ax2=axes('position',get(ax1,'position'),'yaxislocation','right','color','no
ne');
axis([-0.55 0.55 -337.5 337.5])
set(gca,'xtick',[-0.5:0.1:0.5])
set(gca,'ytick',[-337.5:67.5:337.5])
set(ax1,'box','off')
xlabel('Actual Peak Position (range bins)')
ylabel(ax1,'Estimation Error (range bins)')
ylabel(ax2,'Estimation Error (mm)') %  $\Delta x \cdot \Delta R$ 
( $\Delta R = c/2B, B=200\text{MHz}$ )

% error analysis
averageerror=mean(error)
varaverageerror=var(error)

```

```

%% Quartic Interpolation
clear all
close all
t=0:99;
L=length(t);
i=1;
dataactual=[];
dataestimated=[];
error=[];
for N=12.875:0.0125:13.125
    % generate CW signal
    %N=13.2; %N to vary over +/-0.5 for p=1, +/-0.25 for p=2, +/-0.125 for p=4,
    etc
    f=N/L;
    y=sin(2*pi*f*(t-0.5));
    %y=y.*transpose(hanning(L)); % add window function
    %y=awgn(y,10); %add white Gaussian noise to signal, SNR=10dB
    %figure
    %plot(t,y,'LineWidth',1);
    % find spectrum
    spec=abs(fft(y));
    spec=spec(1:round(L/2))/max(spec);
    %figure
    %plot(t(1:round(L/2)),spec,'LineWidth',1)
    %xlabel('number of cycles')
    % zero pad
    p=4;
    if p>1
        y(101:p*100)=0;
    end
    f=0:p*100-1;
    %figure
    %plot(f,y,'LineWidth',1);
    %m=fft(y);
    % find spectrum
    spec=abs(fft(y));
    spec=spec/max(spec);
    %figure
    f=f/p;

```

```

%plot(f,spec,'LineWidth',1)
% plot(t,spec,'*')
%axis([round(N)-3 round(N)+3 0 1])
%xlabel('number of cycles')
%
% estimate peak position from quartic fit
[a,b]=max(spec);
yn=a;
ynminus1=spec(b-1);
ynplus1=spec(b+1);
ynminus2=spec(b-2);
ynplus2=spec(b+2);
actualdeltapeakpos=N-round(N);
estimateddeltaPeakpos=-(ynplus2-2*ynplus1+2*ynminus1-ynminus2)/(ynplus2-
4*ynplus1+6*yn-4*ynminus1+ynminus2)/2/p;
%
%estimateddeltaPeakpos=(ynminus1-3*yn+3*ynplus1-ynplus2)/(ynminus2-
4*ynminus1+6*yn-4*ynplus1+ynplus2)+0.5)/p; % different form, exactly same
result
%
%if i<2
%  estimateddeltaPeakpos=estimateddeltaPeakpos+0.25;
%end
%
dataactual(i)=actualdeltapeakpos;
dataestimated(i)=estimateddeltaPeakpos;
error(i)=dataactual(i)-dataestimated(i);
i=i+1;
end
%
% plot the estimated peak against actual position
x=-1:0.1:1;
zn=x;
figure
plot(x,zn,'--');
hold on
axis([-0.135 0.135 -0.135 0.135])
set(gca,'xtick',[-0.125:0.025:0.125]);
set(gca,'ytick',[-0.125:0.025:0.125]);
plot(dataactual,dataestimated,'r-*')
xlabel('estimated peak position')

```

```

ylabel('actual peak position')
hold off
% plot delta estimation against actual position with double-y axes (range
bins/mm & without using function of 'plotyy')
figure
plot(dataactual,error,'-*')
axis([-0.15 0.15 -0.014 0.014])
set(gca,'xtick',[-0.125:0.025:0.125])
set(gca,'ytick',[-0.014:0.002:0.014])
ax1=gca;
ax2=axes('position',get(ax1,'position'),'yaxislocation','right','color','no
ne');
axis([-0.15 0.15 -10.5 10.5])
set(gca,'xtick',[-0.125:0.025:0.125])
set(gca,'ytick',[-10.5:1.5:10.5])
set(ax1,'box','off')
xlabel('Actual Peak Position (range bins)')
ylabel(ax1,'Estimation Error (range bins)')
ylabel(ax2,'Estimation Error (mm)')           %  $\Delta x \cdot \Delta R$ 
(delta_R=c/2B,B=200MHz)
% error analysis
averageerror=mean(error)
rmserror=rms(error)

```

Appendix B: Matlab codes of the normalised amplitude spectrum of window functions

```

% normalised amplitude spectrum of window functions
%
clear all
close all
%
eps=0.0001;
N=32;
win_rect(1:N)=1;
win_ham=hamming(N);
win_han=hanning(N);
win_kaiser=kaiser(N,pi);
win_kaiser2=kaiser(N,5);
Yrect=abs(fft(win_rect,512));
Yrectn=Yrect./max(Yrect);
Yham=abs(fft(win_ham,512));
Yhamn=Yham./max(Yham);
Yhan=abs(fft(win_han,512));
Yhann=Yhan./max(Yhan);
Ykaiser=abs(fft(win_kaiser,512));
Ykaisern=Ykaiser./max(Ykaiser);
Ykaiser2=abs(fft(win_kaiser2,512));
Ykaisern2=Ykaiser2./max(Ykaiser2);
%
figure(1)
plot(20*log10(Yrectn+eps),'k','linewidth',1.5,'color','b')
xlabel('Sample Number')
ylabel('20*log10(amplitude)')
axis tight
grid
%
figure(2)
plot(20*log10(Yhamn+eps),'k','linewidth',1.5,'color','b')
xlabel('Sample Number')
ylabel('20*log10(amplitude)')
axis tight
grid
%

```

```
figure(3) ↵
plot(20*log10(Yhann+eps), 'k', 'linewidth', 1.5, 'color', 'b') ↵
xlabel('Sample Number') ↵
ylabel('20*log10(amplitude)') ↵
axis tight ↵
grid ↵
↵
figure(4) ↵
plot(20*log10(Ykaisern+eps), 'k', 'linewidth', 1.5, 'color', 'b') ↵
grid ↵
hold on ↵
plot(20*log10(Ykaisern2+eps), 'k:', 'linewidth', 1.5, 'color', 'r') ↵
xlabel('Sample Number') ↵
ylabel('20*log10(amplitude)') ↵
legend('Kaiser par.=\pi', 'Ykaisern2+eps') ↵
axis tight ↵
hold off ↵
```

Appendix C: Matlab codes of the normalised amplitude spectrum of window functions

```
% Probability Density Function (PDF) of Gaussian and Rayleigh models
%
clear all
close all
xg=linspace(-10,10,1000);
xr=linspace(0,10,1000);
mu=0;
sigma=2;
yg=normpdf(xg,mu,sigma);
yr=raylpdf(xr,sigma);
%
figure
plot(xg,yg,'k','linewidth',1.5,'color','b');
grid
hold on
plot(xr,yr,'k:', 'linewidth',1.5,'color','r');
legend('Gaussian pdf','Rayleigh pdf')
xlabel('x')
ylabel('Probability density')
gtext('\mu=0;\sigma=2')
gtext('\sigma=2')
axis tight
hold off
```

Appendix D: Matlab codes of the phase-sensitive process of FMCW radar system

```

% Phase-sensitive FMCW radar processing routine %
%
clear all
close all
%
%%
filename = 'C:\Tracy Wu\FMCW Radar\Data\EXP1\tek0002ALL.csv';
%
filename = 'C:\Tracy Wu\FMCW Radar\Data\EXP1\tek0001ALL.csv';
%
delimiter = ',';
startRow = 22;
|
formatSpec = '%f%f%f%f%[\n\r]';
%
fileID = fopen(filename,'r');
textscan(fileID, '%[\n\r]', startRow-1, 'WhiteSpace', ',', 'ReturnOnError',
false);
dataArray = textscan(fileID, formatSpec, 'Delimiter', delimiter,
'EmptyValue', NaN, 'HeaderLines', startRow-1, 'ReturnOnError', false);
fclose(fileID);
%
TIME = dataArray{: , 1};
CH1 = dataArray{: , 2};
CH2 = dataArray{: , 3};
CH3 = dataArray{: , 4};
%
clearvars filename delimiter formatSpec fileID dataArray ans raw col
numericData rawData row regexstr result numbers invalidThousandsSeparator
thousandsRegExp me rawNumericColumns rawCellColumns R;
%
% data = [CH2,CH3];
%
%%
%
% Set parameters %
c=3e8; % Speed of light
fc=300e6; % Carrier frequency (Hz)
B=200e6; % Sweep bandwidth (Hz)

```

```

T=1;_____ % Pulse duration (s) ↵
Ti=1.6384;_____ % Pulse interval (s) ↵
phi0=0;_____ % Chirp phase offset (0 = Cos (normal), -pi/2 = Sin (Q
reference chirp)) ↵
↵
si = 4e-6;_____ % ADC sample interval ↵
fs=25e4;_____ % ADC sampling rate (Hz) ↵
er=1.2;_____ % Medium dielectric constant ↵
↵
phi0=0;_____ % Chirp phase offset (0 = Cos, -pi/2 = Sin) ↵
% phi1=0*2*pi/360; ↵
% phi2=0*2*pi/360; ↵
↵
% foff=8000;_____ % Active target LO frequency (Hz) ↵
↵
deltaT=0;_____ % Timing delay of ADC wrt chirp ↵
pulseN=1;_____ % Pulse number to be processed ↵
↵
k=2*pi*B/T;_____ % Sweep rate (rad/s/s) ↵
wc=2*pi*fc;_____ % Carrier frequency (rad/s) ↵
↵
% Data 1 ↵
% start = 90424; ↵
% start = 90382; ↵
T=1;_____ % Pulse duration (s) ↵
Ti=1.6384;_____ % Pulse interval (s) ↵
phi0=0;_____ % Chirp phase offset (0 = Cos (normal), -pi/2 = Sin (Q
reference chirp)) ↵
↵
si = 4e-6;_____ % ADC sample interval ↵
fs=25e4;_____ % ADC sampling rate (Hz) ↵
er=1.2;_____ % Medium dielectric constant ↵
↵
phi0=0;_____ % Chirp phase offset (0 = Cos, -pi/2 = Sin) ↵
% phi1=0*2*pi/360; ↵
% phi2=0*2*pi/360; ↵
↵
% foff=8000;_____ % Active target LO frequency (Hz) ↵
↵

```

```

↵
deltaT=0;      % Timing delay of ADC wrt chirp↵
pulseN=1;     % Pulse number to be processed↵
↵
k=2*pi*B/T;     % Sweep rate (rad/s/s)↵
wc=2*pi*fc;  % Carrier frequency (rad/s)↵
↵
% Data 1↵
% start = 90424;↵
% start = 90382;↵
% stop = start+fs-1;↵
↵
% Data 2↵
% start = 90382;↵
% stop = start+fs-1;↵
↵
% Data 3↵
% start = 1158;↵
% stop = 4230;↵
↵
% Data 4↵
% start = 164572;↵
% stop = start+fs-1;↵
↵
% Data 5↵
% start = 90382;↵
% stop = start+fs-1;↵
↵
% Data 6↵
% start = 90382;↵
% stop = start+fs-1;↵
↵
% vif=transpose(data(start:stop));↵
% t=0:1/fs:(length(vif)-1)/fs;↵
% figure↵
% plot(t,vif)↵
% xlabel('Time (s)')↵
% ylabel('Voltage (V)')↵
↵

```

```

↵
% CH2=transpose(CH2(start:stop)); ↵
↵
↵
% CH3=transpose(CH3(start:stop)); ↵
% t=0:1/fs:(length(CH2)-1)/fs; ↵
% figure ↵
% plot(t,CH2) ↵
% figure|↵
% plot (t,CH3) ↵
% xlabel('Time (s)') ↵
% ylabel('Voltage (V)') ↵
↵
%% ↵
↵
dataI=CH2; ↵
dataQ=CH1; ↵
% dataI=CH2(start:stop); ↵
% dataQ=CH3(start:stop); ↵
↵
t=0:1/fs:(length(dataI)-1)/fs; ↵
figure ↵
plot(t,dataI) ↵
title ('I Data') ↵
xlabel('Time (s)') ↵
ylabel('Voltage (V)') ↵
figure ↵
plot (t,dataQ) ↵
title ('Q Data') ↵
xlabel('Time (s)') ↵
ylabel('Voltage (V)') ↵
↵
for n=1:round(length(dataI)/fs/Ti-0.5) ↵
    vif2(n,1:fs)=dataI((n-1)*fs*Ti+1:(n-1)*fs*Ti+fs*T)+j*dataQ((n-
1)*fs*Ti+1:(n-1)*fs*Ti+fs*T); ↵
end ↵
↵

```

```

%%
% Range processing %
↵
vif=vif2(pulseN,1:fs);
↵
vif=vif-mean(vif); % Zero-mean
↵
% t=0:1/fs:(length(CH2)-1)/fs;
% figure
% plot(t,vif)
↵
%%
↵
% Apply window to signal
↵
L=length(vif);
% vif=vif.*transpose(blackman(L));
↵
% Zero-pad and shift centre of deramped signal to t=0
padfactor=2;
vifpad=zeros(1,padfactor*L);
vifpad(1:0.5*L)=vif(0.5*L+1:L);
vifpad(padfactor*L-0.5*L+1:padfactor*L)=vif(1:0.5*L);
vif=vifpad;
↵
T=T*padfactor;
↵
%%
% Enter peak search parameters
expected=135; % Expected position of peak (m)
% expected=3; % Expected position of peak (m)
% tolerance=8; % Tolerance (m)
tolerance=0.5; % Tolerance (m)
binmin=round((expected-tolerance)/(c/2/B/padfactor/sqrt(er)));
binmax=round((expected+tolerance)/(c/2/B/padfactor/sqrt(er)));
%%
↵

```

```

% Take FFT and scale - first sideband
fftvif=(sqrt(2*padfactor)/length(vif))*fft(vif);
spec=fftvif(1:round(length(vif)/2-0.5));
magspec=abs(spec);
% magspec(1:500*padfactor)=0; % Remove large signals near DC
magspec=magspec/sqrt(mean(blackman(L).*blackman(L))); % Compensate for
window
freq=0:1/T:fs/2-1/T;
rangemetres = freq*c/2/B/sqrt(er);
figure
plot((freq/10^3),10*log(magspec), 'linewidth',1)
title ('Frequency Spectrum')
set(gca, 'fontsize',10)
set(gca, 'linewidth',1)

xlabel('Frequency (kHz)')
ylabel('Power (dB)')

% ylim([-100 0])
% ylim([-95 -20])

% axis([0 fs/2 -50+max(20*log10(10e9*magspec))
3+max(20*log10(10e9*magspec))])

xlim([0.1 0.3]) % Limit range to that of interest for long cable only
% xlim([7.95 8.05]) % Limit range to that of interest for 8khz
% xlim([0 10]) % Limit range to that of interest for 8khz

% xlim([1.61e4 1.63e4]) % Limit range to that of interest for 16khz
% xlim([3.1e4 3.35e4]) % Limit range to that of interest for 32khz
% xlim([6.3e4 6.5e4]) % Limit range to that of interest for 64khz

figure
plot(rangemetres,10*log(magspec), 'linewidth',2)

set(gca, 'fontsize',10)
set(gca, 'linewidth',1)
title ('Range Profile')
xlabel('Range (m)')

```

```

ylabel('Power (dB)')
% xlim([5 300]) % Limit range to that of interest
xlim([1 20]) % Limit range to that of interest
[a,b]=max(magspec(binmin:binmax));
b=b+binmin-1;
% [a,b]=max(magspec(foff*T:2*foff*T)); % Restrict search to known range of
signal
% b=b+foff*T-1;
rangebinmetres=(b-1)*c/2/abs(B)/padfactor/sqrt(er)
cable_length = rangebinmetres*2
%%
% Generate reference phase - i.e. expected phase of signal at each range
bin
m=0:length(spec)-1;
m=m/padfactor;
phiref=2*pi*fc.*m/B-k*m.*m/2/B/B+phi0;
deltaphi=2*pi*deltaT*fs*m/length(spec); % Compensate phase for ADC delay of
deltaT
phiref=phiref-deltaphi;
comp=exp(-j*phiref);
spec=spec.*comp; % Compensate measured signal so that phase = 0 in each
range bin for target centred in range bin
% Use measured phase for fine-precision range measurement
phasepeakdegs=(180/pi)*angle(spec(b))
% Routine that MAY detect and correct phase wrap errors
if magspec(b+1)>magspec(b-1)
    if phasepeakdegs<-150
        phasepeakdegs=phasepeakdegs+360
    end
end
if magspec(b-1)>magspec(b+1)
    if phasepeakdegs>150

```

```
    phasepeakdegs=phasepeakdegs-360;
end
end
%
deltarangemetres=phasepeakdegs*c/360/2/fc/sqrt(er);
estimatedrangemetres=rangebinmetres+deltarangemetres;
Vrms=sqrt(sum(magspec.*magspec)) % Total signal+noise rms voltage;
```

References

- [1] Corr, Hugh FJ, et al. "Precise measurement of changes in ice-shelf thickness by phase-sensitive radar to determine basal melt rates." *Geophysical Research Letters* 29.8 (2002).
- [2] Jenkins, Adrian, et al. "Interactions between ice and ocean observed with phase-sensitive radar near an Antarctic ice-shelf grounding line." *Journal of Glaciology* 52.178 (2006): 325-346.
- [3] N. Vriend, J. McElwaine, C. Keylock, P. Brennan, "High Resolution Radar Measurements of Snow Avalanches", *Geophysical Research Letters*, Vol. 40, 727-31, (2013).
- [4] Brennan, Paul V., et al. "Phase-sensitive FMCW radar system for high-precision Antarctic ice shelf profile monitoring." *IET Radar, Sonar & Navigation* 8.7 (2014): 776-786.
- [5] Ash, M., P. V. Brennan, N. M. Vriend, J. N. McElwaine, and C. J. Keylock. "FMCW phased array radar for automatically triggered measurements of snow avalanches." In *Radar Conference (EuRAD), 2011 European*, pp. 166-169. IEEE, (2011).
- [6] Eckerstorfer, Markus, et al. "Remote sensing of snow avalanches: Recent advances, potential, and limitations." *Cold Regions Science and Technology* 121 (2016): 126-140.
- [7] Tudose, Mihai, et al. "On the beat signal synchronisation of interferometric FMCW radars." *IET Radar, Sonar & Navigation* (2017).
- [8] Anghel, Andrei, et al. "Short-range wideband FMCW radar for millimetric displacement measurements." *IEEE Transactions on Geoscience and Remote Sensing* 52.9 (2014): 5633-5642.
- [9] Zhang, Rui, et al. "Scene Dynamics Estimation for Parameter Adjustment of Gaussian Mixture Models." *IEEE Signal Processing Letters* 21.9 (2014): 1130-1134.
- [10] Zhao, Yichao, and Yi Su. "Vehicles Detection in Complex Urban Scenes Using Gaussian Mixture Model with FMCW Radar." *IEEE Sensors Journal* (2017).
- [11] Mateo, Ana Baselga, and Zeb W. Barber. "Multi-dimensional, non-contact metrology using trilateration and high resolution FMCW radar." *Applied Optics* 54.19 (2015): 5911-5916.
- [12] Kaveh, Sajjad, and Yaser Norouzi. "Non-uniform sampling and super-resolution method to increase the accuracy of tank gauging radar." *IET Radar, Sonar & Navigation* 11.5 (2016): 788-796.
- [13] Wang, Guochao, et al. "A hybrid FMCW-interferometry radar for indoor precise positioning and versatile life activity monitoring." *IEEE Transactions on Microwave Theory and Techniques* 62.11 (2014): 2812-2822.

- [14] Candan, Cagatay. "A Method For Fine Resolution Frequency Estimation From Three DFT Samples." *IEEE Signal Process. Lett.* 18.6 (2011): 351-354.
- [15] Richards, Mark A. *Fundamentals of radar signal processing*. Tata McGraw-Hill Education, (2005).
- [16] Rabiner, L., R. W. Schafer, and C. Rader. "The chirp z-transform algorithm." *IEEE transactions on audio and electroacoustics* 17.2 (1969): 86-92.
- [17] Wang, Tien T. "The segmented chirp z-transform and its application in spectrum analysis." *IEEE Transactions on instrumentation and measurement* 39.2 (1990): 318-323.
- [18] Lanari, Riccardo. "A new method for the compensation of the SAR range cell migration based on the chirp z-transform." *IEEE Transactions on Geoscience and Remote Sensing* 33.5 (1995): 1296-1299.
- [19] Peleg, Shimon, and Boaz Porat. "The Cramer-Rao lower bound for signals with constant amplitude and polynomial phase." *IEEE Transactions on Signal Processing* 39.3 (1991): 749-752.
- [20] Yazdanfar, Siavash, et al. "Frequency estimation precision in Doppler optical coherence tomography using the Cramer-Rao lower bound." *Optics express* 13.2 (2005): 410-416.
- [21] Gappmair, Wilfried. "Cramer-Rao lower bound for non-data-aided SNR estimation of linear modulation schemes." *IEEE transactions on communications* 56.5 (2008): 689-693.
- [22] Patole, Sujeet Milind, et al. "Automotive radars: A review of signal processing techniques." *IEEE Signal Processing Magazine* 34.2 (2017): 22-35.
- [23] Rohling, Hermann, and M-M. Meinecke. "Waveform design principles for automotive radar systems." *2001 CIE International Conference on Radar Proceedings (Cat No. 01TH8559)*. IEEE, 2001.
- [24] Lin, Jau-Jr, et al. "Design of an FMCW radar baseband signal processing system for automotive application." *Springer Plus* 5.1 (2016): 42.
- [25] Hakobyan, Gor, and Bin Yang. "High-performance automotive radar: A review of signal processing algorithms and modulation schemes." *IEEE Signal Processing Magazine* 36.5 (2019): 32-44.
- [26] Bilik, Igal, et al. "The Rise of Radar for Autonomous Vehicles: Signal processing solutions and future research directions." *IEEE Signal Processing Magazine* 36.5 (2019): 20-31.
- [27] Kliazovich, Dzmitry, et al. "CA-DAG: Modelling communication-aware applications for scheduling in cloud computing." *Journal of Grid Computing* 14.1 (2016): 23-39.

- [28] Dizdarević, Jasenka, et al. "A survey of communication protocols for internet of things and related challenges of fog and cloud computing integration." *ACM Computing Surveys (CSUR)* 51.6 (2019): 1-29.
- [29] Mukherjee, Sudarshan, and Jemin Lee. "Edge computing-enabled cell-free massive MIMO systems." *IEEE Transactions on Wireless Communications* 19.4 (2020): 2884-2899.
- [30] Busari, Sherif Adeshina, et al. "Millimetre-wave massive MIMO for cellular vehicle-to-infrastructure communication." *IET Intelligent Transport Systems* 13.6 (2019): 983-990.
- [31] Petersson, Markus. "Performance assessment of massive MIMO systems for positioning and tracking of vehicles in open highways." (2017).
- [32] Li, Yahong, et al. "Continuously prepared highly conductive and stretchable SWNT/MWNT synergistically composited electrospun thermoplastic polyurethane yarns for wearable sensing." *Journal of Materials Chemistry C* 6.9 (2018): 2258-2269.
- [33] Lee, Youngsik, et al. "Wearable sensing systems with mechanically soft assemblies of nanoscale materials." *Advanced Materials Technologies* 2.9 (2017): 1700053.
- [34] Giaccardi, Elisa, et al. "Thing ethnography: doing design research with non-humans." *Proceedings of the 2016 ACM Conference on Designing Interactive Systems*. 2016.
- [35] Kees, Alexandra, et al. "Understanding the Internet of Things: A Conceptualisation of Business-to-Thing (B2T) Interactions." *ECIS*. 2015.
- [36] Wang, Wen-Qin. "Cognitive frequency diverse array radar with situational awareness." *IET Radar, Sonar & Navigation* 10.2 (2016): 359-369.
- [37] Scanlon, Michael V., and William D. Ludwig. "Sensor and information fusion for improved hostile fire situational awareness." *Unattended Ground, Sea, and Air Sensor Technologies and Applications XII*. Vol. 7693. International Society for Optics and Photonics, 2010.
- [38] Zhang, Yu, et al. "A modified waveform design for radar-communication integration based on LFM-CPM." *2017 IEEE 85th Vehicular Technology Conference (VTC Spring)*. IEEE, 2017.
- [39] Liu, Yongjun, et al. "Design of integrated radar and communication system based on MIMO-OFDM waveform." *Journal of Systems Engineering and Electronics* 28.4 (2017): 669-680.
- [40] Tian, Xuanxuan, and Zhaohui Song. "On radar and communication integrated system using OFDM signal." *2017 IEEE Radar Conference (RadarConf)*. IEEE, 2017.
- [41] Skolnik, Merrill I. *Introduction to radar. Radar Handbook 2*, (1962).
- [42] Blake, Lamont V. *Radar range-performance analysis*. Norwood, MA, Artech House, Inc., (1986).
- [43] Morris, Guy V. *Airborne pulsed Doppler radar*. Artech House Publishers, (1988).

- [44] Jankiraman, Mohinder. *Design of multi-frequency CW radars*. Vol. 2. SciTech Publishing, (2007).
- [45] Scheer, Jim, and James L. Kurtz. *Coherent radar performance estimation*. Boston: Artech House, (2012).
- [46] Ghiglia, Dennis C., and Mark D. Pritt. *Two-dimensional phase unwrapping: theory, algorithms, and software*. Vol. 4. New York: Wiley, (1998).
- [47] Kay, Steven M. *Fundamentals of statistical signal processing*. Prentice Hall PTR, 1993.
- [48] Doviak, Richard J. *Doppler radar and weather observations*. Courier Corporation, 2006.
- [49] Setlur, Pawan, Moeness Amin, and Fauzia Ahmad. "Dual-frequency doppler radars for indoor range estimation: Cramér–rao bound analysis." *IET Signal Processing* 4.3 (2010): 256-271.
- [50] Bar-Shalom, Yaakov. "Negative correlation and optimal tracking with Doppler measurements." *IEEE Transactions on Aerospace and Electronic Systems* 37.3 (2001): 1117-1120.
- [51] Trunk, G., and S. Brockett. "Range and velocity ambiguity resolution." *The Record of the 1993 IEEE National Radar Conference*. IEEE, 1993.
- [52] Kolawole, Michael. *Radar systems, peak detection and tracking*. Elsevier, 2003.
- [53] Li, Yang, et al. "Range migration compensation and Doppler ambiguity resolution by Keystone transform." *2006 CIE International Conference on Radar*. IEEE, 2006.
- [54] Hennington, Larry. "Reducing the effects of Doppler radar ambiguities." *Journal of Applied Meteorology* 20.12 (1981): 1543-1546.
- [55] Marshall, Hans-Peter, and Gary Koh. "FMCW radars for snow research." *Cold Regions Science and Technology* 52.2 (2008): 118-131.
- [56] Li, J., et al. "Airborne Snow Measurements Over Alaska Mountains and Glaciers With A Compact FMCW Radar." *IGARSS 2019-2019 IEEE International Geoscience and Remote Sensing Symposium*. IEEE, 2019.
- [57] Ayhan, Serdal, et al. "Frequency estimation algorithm for an extended FMCW radar system with additional phase evaluation." *Microwave Conference (GeMIC), 2011 German*. IEEE, (2011).
- [58] Guoqing, Qi. "Digital signal processing in FMCW radar marine tank gauging system." *Signal Processing, 3rd International Conference on*. Vol. 1. IEEE, (1996).
- [59] Anghel, Andrei, et al. "Short-range wideband FMCW radar for millimetric displacement measurements." *IEEE Transactions on Geoscience and Remote Sensing* 52.9 (2014): 5633-5642.

- [60] Wojtkiewicz, Andrzej, et al. "Two-dimensional signal processing in FMCW radars." *Proc. XX KKTOiUE* (1997): 475-480.
- [61] Pauli, Mario, et al. "Range detection with micrometer precision using a high accuracy FMCW radar system." *Systems, Signals and Devices (SSD), 2012 9th International Multi-Conference on*. IEEE, (2012).
- [62] Ayhan, Serdal, et al. "System simulation for FMCW radar in industrial applications." *2016 IEEE Topical Conference on Wireless Sensors and Sensor Networks (WiSNet)*. IEEE, 2016.
- [63] Scherr, Steffen, et al. "An efficient frequency and phase estimation algorithm with CRB performance for FMCW radar applications." *IEEE Transactions on Instrumentation and Measurement* 64.7 (2015): 1868-1875.
- [64] Stove, Andrew G. "Linear FMCW radar techniques." *IEE Proceedings F (Radar and Signal Processing)*. Vol. 139. No. 5. IET Digital Library, (1992).
- [65] Scheer, Jim, and William A. Holm. *Principles of modern radar*. Eds. Mark A. Richards, and William L. Melvin. SciTech Pub., (2010).
- [66] Wehner, Donald R. *High resolution radar*. Norwood, MA, Artech House, Inc., (1987).
- [67] Ash, M., Chetty, K., Brennan, P., McElwaine, J., & Keylock, C. (2010, May). FMCW radar imaging of avalanche-like snow movements. In *Radar Conference, 2010 IEEE* (pp. 102-107).
- [68] Niu, Ruixin, et al. "Target localization and tracking in noncoherent multiple-input multiple-output radar systems." *IEEE Transactions on Aerospace and Electronic Systems* 48.2 (2012): 1466-1489.
- [69] Willett, Peter, William Dale Blair, and Xin Zhang. "The multitarget monopulse CRLB for matched filter samples." *IEEE Transactions on Signal Processing* 55.8 (2007): 4183-4197.
- [70] Varshney, Lav R., and Daniel Thomas. "Sidelobe reduction for matched filter range processing." *Proceedings of the 2003 IEEE Radar Conference (Cat. No. 03CH37474)*. IEEE, 2003.
- [71] Wang, Jun, Duoduo Cai, and Yaya Wen. "Comparison of matched filter and dechirp processing used in linear frequency modulation." *2011 IEEE 2nd International Conference on Computing, Control and Industrial Engineering*. Vol. 2. IEEE, 2011.
- [72] Anttila, Lauri, Mikko Valkama, and Markku Renfors. "Circularity-based I/Q imbalance compensation in wideband direct-conversion receivers." *IEEE Transactions on Vehicular Technology* 57.4 (2008): 2099-2113.
- [73] Lees, M. L. "Digital beamforming calibration for FMCW radar." *IEEE transactions on aerospace and electronic systems* 25.2 (1989): 281-284.

- [74] Jahn, Martin, et al. "A four-channel 94-GHz SiGe-based digital beamforming FMCW radar." *IEEE transactions on microwave theory and techniques* 60.3 (2012): 861-869.
- [75] Farnett, Edward C., George H. Stevens, and Merrill Skolnik. "Pulse compression radar." *Radar handbook 2* (1990): 10-1.
- [76] Cook, Charles E. "Pulse compression-key to more efficient radar transmission." *Proceedings of the IRE* 48.3 (1960): 310-316.
- [77] Fuhrmann, Daniel R., Edward J. Kelly, and Ramon Nitzberg. "A CFAR adaptive matched filter detector." *IEEE Trans. Aerosp. Electron. Syst* 28.1 (1992): 208-216.
- [78] Perry, R. P., R. C. Dipietro, and R. L. Fante. "SAR imaging of moving targets." *IEEE Transactions on Aerospace and Electronic Systems* 35.1 (1999): 188-200.
- [79] DeGraaf, Stuart R. "SAR imaging via modern 2-D spectral estimation methods." *IEEE Transactions on Image Processing* 7.5 (1998): 729-761.
- [80] Li, Jian, and Petre Stoica. "An adaptive filtering approach to spectral estimation and SAR imaging." *IEEE Transactions on Signal Processing* 44.6 (1996): 1469-1484.
- [81] Page, Douglas, Steven Scarborough, and S. Crooks. "Improving knowledge-aided STAP performance using past CPI data [radar signal processing]." *Proceedings of the 2004 IEEE Radar Conference (IEEE Cat. No. 04CH37509)*. IEEE, 2004.
- [82] Lee, Jong-Sen, et al. "Intensity and phase statistics of multilook polarimetric and interferometric SAR imagery." *IEEE Transactions on Geoscience and Remote Sensing* 32.5 (1994): 1017-1028.
- [83] Frühwirth, Rudolf. "Application of Kalman filtering to track and vertex fitting." *Nuclear Instruments and Methods in Physics Research Section A: Accelerators, Spectrometers, Detectors and Associated Equipment* 262.2-3 (1987): 444-450.
- [84] Mighell, Kenneth J. "Stellar photometry and astrometry with discrete point spread functions." *Monthly Notices of the Royal Astronomical Society* 361.3 (2005): 861-878.
- [85] Peleg, Shimon, and Boaz Porat. "The Cramer-Rao lower bound for signals with constant amplitude and polynomial phase." *IEEE Transactions on Signal Processing* 39.3 (1991): 749-752.
- [86] Toker, Onur, and Marius Brinkmann. "A Novel Nonlinearity Correction Algorithm for FMCW Radar Systems for Optimal Range Accuracy and Improved Multitarget Detection Capability." *Electronics* 8.11 (2019): 1290.
- [87] Quinn, Barry G. "Estimating frequency by interpolation using Fourier coefficients." *IEEE transactions on Signal Processing* 42.5 (1994): 1264-1268.

- [88] Jacobsen, Eric. "On local interpolation of DFT outputs." Available online: <http://www.ericjacobsen.org/FTinterp.pdf>. [Accessed January 2013] (1994).
- [89] Belega, Daniel, Dominique Dallet, and Dario Petri. "Accuracy of sine wave frequency estimation by multipoint interpolated DFT approach." *IEEE Transactions on Instrumentation and Measurement* 59.11 (2010): 2808-2815.
- [90] Wen, He, Chengcheng Li, and Lu Tang. "Novel three-point interpolation DFT method for frequency measurement of sine-wave." *IEEE Transactions on Industrial Informatics* 13.5 (2017): 2333-2338.
- [91] Belega, Daniel, Dario Petri, and Dominique Dallet. "Accuracy analysis of complex sinusoid amplitude and phase estimation by means of the interpolated discrete-time Fourier transform algorithm." *Digital Signal Processing* 59 (2016): 9-18.
- [92] Agrez, Dusan. "Weighted multipoint interpolated DFT to improve amplitude estimation of multifrequency signal." *IEEE Transactions on Instrumentation and Measurement* 51.2 (2002): 287-292.
- [93] Grandke, Thomas. "Interpolation algorithms for discrete Fourier transforms of weighted signals." *IEEE transactions on instrumentation and measurement* 32.2 (1983): 350-355.
- [94] Luo, Jiufei, Zhijiang Xie, and Ming Xie. "Interpolated DFT algorithms with zero padding for classic windows." *Mechanical Systems and Signal Processing* 70 (2016): 1011-1025.
- [95] Guoqing, Qi. "High accuracy range estimation of FMCW level radar based on the phase of the zero-padded FFT." *Proceedings 7th International Conference on Signal Processing, 2004. Proceedings. ICSP'04. 2004.*. Vol. 3. IEEE, 2004.
- [96] Bhutani, Akanksha, et al. "The Role of Millimeter-Waves in the Distance Measurement Accuracy of an FMCW Radar Sensor." *Sensors* 19.18 (2019): 3938.
- [97] Babaeian, Kayvan, et al. "A CZT-Based Algorithm for Improving Multi-Target Ranging in FMCW Radar." *2019 27th Iranian Conference on Electrical Engineering (ICEE)*. IEEE, 2019.
- [98] Pauli, Mario, et al. "Range detection with micrometer precision using a high accuracy FMCW radar system." *International Multi-Conference on Systems, Signals & Devices*. IEEE, 2012.
- [99] Orth, Alexander, et al. "High precision real-time FMCW-radar signal processing performed on a levitating sphere control loop system." *2018 11th German Microwave Conference (GeMiC)*. IEEE, 2018.
- [100] Ayhan, Serdal, et al. "FMCW radar system with additional phase evaluation for high accuracy range detection." *2011 8th European Radar Conference*. IEEE, 2011.
- [101] Ikram, Muhammad Z., Adeel Ahmad, and Dan Wang. "High-accuracy distance measurement using millimeter-wave radar." *2018 IEEE Radar Conference (RadarConf18)*. IEEE, 2018.

- [102] Xiong, Yuyong, et al. "High-precision frequency estimation for FMCW radar applications based on parameterized de-alternating and modified ICCD." *Measurement Science and Technology* 29.7 (2018): 075010.
- [103] Stoica, Petre, and Torsten Soderstrom. "Statistical analysis of MUSIC and subspace rotation estimates of sinusoidal frequencies." *IEEE Transactions on Signal Processing* 39.8 (1991): 1836-1847.
- [104] Kumaresan, Ramdas, and Donald W. Tufts. "Estimating the angles of arrival of multiple plane waves." *IEEE Transactions on Aerospace and Electronic Systems* 1 (1983): 134-139.
- [105] Roy, Richard, and Thomas Kailath. "ESPRIT-estimation of signal parameters via rotational invariance techniques." *IEEE Transactions on acoustics, speech, and signal processing* 37.7 (1989): 984-995.
- [106] Kim, Sangdong, Daegun Oh, and Jonghun Lee. "Joint DFT-ESPRIT estimation for TOA and DOA in vehicle FMCW radars." *IEEE Antennas and Wireless Propagation Letters* 14 (2015): 1710-1713.
- [107] Larsson, Erik G., Jian Li, and Petre Stoica. "High-resolution nonparametric spectral analysis: Theory and applications." *High-resolution and robust signal processing*. Vol. 4. Marcel Dekker, 2003. 153-253.
- [108] Lacoss, Richard T. "Data adaptive spectral analysis methods." *Geophysics* 36.4 (1971): 661-675.
- [109] Stoica, Petre, Hongbin Li, and Jian Li. "A new derivation of the APES filter." *IEEE Signal Processing Letters* 6.8 (1999): 205-206.
- [110] Slepian, David. "Estimation of signal parameters in the presence of noise." *Transactions of the IRE Professional Group on Information Theory* 3.3 (1954): 68-89.
- [111] Shi, Chenguang, et al. "Cramer-Rao lower bound evaluation for linear frequency modulation based active radar networks operating in a Rice fading environment." *Sensors* 16.12 (2016): 2072.
- [112] FAN, Z., et al. "Cramer-Rao Lower Bounds of Parameter Estimation for Frequency-Modulated Continuous Wave (CW) Lidar." (2018).
- [113] Ding, Shuai, et al. "Exact and Closed-Form CRLBS for High-Order Kinematic Parameters Estimation Using LFM Coherent Pulse Train." *IEEE Access* 6 (2018): 57447-57459.
- [114] Rahman, S., P. V. Brennan, and L. Lok. "Millimeter-precision range profiling and cross-sectional imaging of ice shelves in Polar regions using phase-sensitive FMCW radar." In *Radar Conference (RADAR), 2013 IEEE*, pp. 1-5. IEEE, (2013).

- [115] Mahafza, Bassem R. *Introduction to radar analysis*. Chapman and Hall/CRC, (2017).
- [116] Rosenberg, Luke, and Stephen Bocquet. "Non-coherent Radar Detection Performance in Medium Grazing Angle X-Band Sea Clutter." *IEEE Transactions on Aerospace and Electronic Systems* 53.2 (2017): 669-682.
- [117] Petrov, Fedor. "Polynomial approach to explicit formulae for generalized binomial coefficients." *European Journal of Mathematics* 2.2 (2016): 444-458.
- [118] Lambert, AJD Fred, and Surendra M. Gupta. *Disassembly modeling for assembly, maintenance, reuse and recycling*. CRC press, (2016).
- [119] Stoica P, Moses RL. *Spectral analysis of signals*, (2005)
- [120] Mason, Eric, Bariscan Yonel, and Birsen Yazici. "Deep learning for radar." *2017 IEEE Radar Conference (RadarConf)*. IEEE, 2017.
- [121] Gong, Maoguo, et al. "Change detection in synthetic aperture radar images based on deep neural networks." *IEEE transactions on neural networks and learning systems* 27.1 (2015): 125-138.
- [122] Sebt, M. A., A. Sheikhi, and M. M. Nayebi. "Orthogonal frequency-division multiplexing radar signal design with optimised ambiguity function and low peak-to-average power ratio." *IET radar, sonar & navigation* 3.2 (2009): 122-132.
- [123] Wen, Miaowen, et al. "Multiple-mode orthogonal frequency division multiplexing with index modulation." *IEEE Transactions on Communications* 65.9 (2017): 3892-3906.
- [124] Bourdoux, A., K. Parashar, and M. Bauduin. "Phenomenology of mutual interference of FMCW and PMCW automotive radars." *2017 IEEE Radar Conference (RadarConf)*. IEEE, 2017.
- [125] Li, Guangzuo, et al. "Linear frequency-modulated continuous-wave ladar system for synthetic aperture imaging." *Applied optics* 56.12 (2017): 3257-3262.
- [126] Zhu, Dekang, et al. "A novel high-precision phase-derived-range method for direct sampling LFM radar." *IEEE Transactions on Geoscience and Remote Sensing* 54.2 (2015): 1131-1141.
- [127] Pauli, Mario, et al. "Miniaturized millimeter-wave radar sensor for high-accuracy applications." *IEEE Transactions on Microwave Theory and Techniques* 65.5 (2017): 1707-1715.
- [128] DiFranco, J. V., and W. L. Rubin. *Radar Detection* / J.V. DiFranco and W.L. Rubin. Raleigh, NC: SciTech Pub., 2004. SciTech Radar and Defense Ser.
- [129] Shnidman, D.A. "Expanded Swerling Target Models." *IEEE Transactions on Aerospace and Electronic Systems* 39.3 (2003): 1059-069.

- [130] Aittomaki, T, and Koivunen, V. "Performance of MIMO Radar With Angular Diversity Under Swerling Scattering Models." *IEEE Journal of Selected Topics in Signal Processing* 4.1 (2010): 101-14.
- [131] Bosse, Jonathan, Krasnov, Oleg, and Yarovoy, Alexander. "Direct Target Localization with an Active Radar Network." *Signal Processing* 125 (2016): 21-35.